A MicroMegas neutron beam imaging detector at the n_TOF facility at CERN

F. Belloni[1],
[1]*CEA-Saclay, Irfu, F-91191 Gif-sur-Yvette France*

March 12, 2014

Abstract

The determination of neutron induced cross sections demands a precise knowledge of the neutron beam profile. Different experiments have adopted different detectors.

At the n_TOF facility [1] the neutron beam profile is determined with a MicroMegas detector equipped with a neutron to charged particles converter, allowing to exploit ionization for detection purposes.

This report summarizes the results obtained in 4 years of operation of the "XY-micromegas" detector, as well as in the test of the "PXMG-micromegas" detector at the n_TOF facility at CERN.

A brief introduction about micromegas detectors and the differences between bulk and microbulk technology is first reported, followed by simulations allowing to draw considerations to establish the best image reconstruction method. The description of the two detectors and the data analysis succeed in chronological order.

Contents

1 Introduction

The rate of reactions induced by a beam of particles in a target is proportional to the current of the incident particles. Neutron induced cross section measurements therefore require the precise knowledge of the incident neutron beam, both in terms of flux and of spatial dimensions. The combination of these two quantities for a precise energy of the incident particles gives the beam profile, defined as the spatial intensity of the beam at a particular plane transverse to the beam propagation path, determined at the chosen energy of the incident particles.

The study of the neutron beam profile requires the use of a neutron detector position sensitive. Since neutrons are uncharged, they do not feel to the Coulomb force and can travel through many centimeters of material without experiencing any type of interaction, resulting invisible to common size detectors. When neutrons undergo an interaction, it is with a nucleus of the absorbing material. In such interaction, either the neutron disappears giving life to heavy charged particles, or it changes its direction and ionizes the nucleus it collides with. Most neutron detectors are equipped with a neutron to charged particles (n/cp) converter, allowing to kill the neutrons and directly detect the charged particles.

Different experiments have chosen different methods to measure the neutron beam profile. For instance at the Van de Graaff facility in IRMM [2] (monochromatic neutron beams) activation of aluminum foil is exploited [3], while at The Svedberg Laboratory (TSL) neutron beam facility in Uppsala, protons emitted from a CH_2 target as a consequence of the elastic scattering of high energy monochromatic neutrons are detected with a setup called SCAttering Nucleon Detection AssembLy (SCANDAL) and consisting in a couple of drift chambers for trajectory determination and a CsI scintillator for measuring the proton energy at the chosen angle (the incident neutron energy is consecutively derived) [4].

At the n_ELBE time of flight facility the neutron beam profile is scanned by detecting fast neutron (200 keV $\leq$ E_n $\leq$ 7 MeV) with movable plastic scintillators [3].

2 Micromegas detectors

Micromegas (MICRO-MEsh-GAseous Structure) [5] detectors are gas detectors combining the principles of ionization and proportional chambers. This coupling is made possible by the presence of a micromesh separating the active volume in two regions, where two different electric fields establish respectively a charge drift and a charge multiplication regime. These detectors can be schematically represented as in Fig. 1.

In the first micromegas detectors the mesh was a real metallic grid and the 3 main components (anode, mesh and drift) were all stand alone pieces, assembled together by using screws. One of the advantages of this building procedure relied on the fact that the separation of the 3 parts and their subsequent remounting was possible. On the other hand, this mechanical configuration was not exempt from small shifts of the mesh with respect to the anode. For this reason a new building procedure, aiming at reducing the number of stand alone components in micromegas detectors, was developed, resulting in

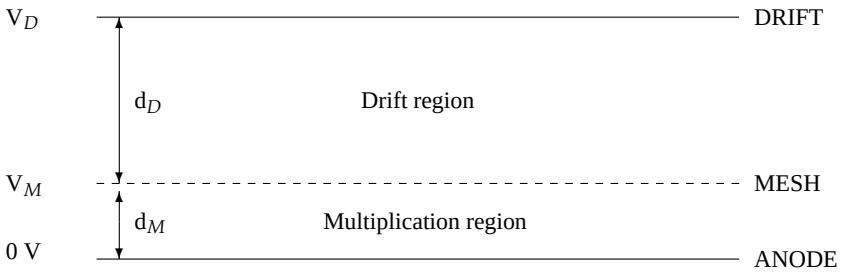

Figure 1. Schematic representation of a micromegas detector. V_M and V_D are the mesh and drift voltages.

the bulk and microbulk technology.

A bulk [6] is anode and the mesh in a unique piece. Their separation results in the irremediable destruction of the detector. In bulks, the mesh is a metallic grid, but not in a single foil: it is composed by intersecting “owened” wires of a usual diameter ⌀ = 18 μm, therefore it is 36 μm “thick" (see Fig. 2).

The typical manufacturing process of a bulk is schematically drawn in Fig. 3. A metal (Cu) slab is used as a support and two layers of Vacrel (a photosensitive material), each 64 μm thick, are superimposed and laminated in order to achieve a thickness of 128 μm for what will become the multiplication region. At this point the mesh is stretched at the top of the second Vacrel layer, and a third Vacrel layer is added above the mesh (upper panel of Fig. 3). Everything is laminated together, to get one single object which, after interposition of a mask presenting circular holes, is irradiated by UV light. The Vacrel touched by the light passing through the holes becomes resistive to chemical attack, while the Vacrel shadowed by the mask remains unchanged and is subsequently removed by an etching procedure. The final result, the bulk, is therefore a metallic slab, housing Vacrel pillars 128 μm high which support the mesh (lower panel of Fig. 3) and a further layer of pillars.

In order to obtain a solid structure with a thinner mesh and with lower quantity of material (which is translated in absence of perturbation of the incident beam), the microbulk technology [7] was developed. The typical manufacturing process is illustrated in Fig. 4. A layer of a polyamide, for example kapton, 50 μm thick is sandwiched between two copper slabs, each 5 μm thick. No lamination is performed. The sandwich is obtained by vacuum evaporation of Cu on kapton. A mask of a photosensitive material is then deposited on the top of the upper copper layer, and everything is irradiated with UV (left panel of Fig. 4). After removing the mask, different etchings are applied. The first one gets rid of that portion of the copper layer which was not shielded by the mask, while the second one penetrates deep inside the kapton and chemically attacks that. The result is a copper slab supporting a kapton-“gruyère" (right panel of Fig. 4).

A microbulk is therefore anode and mesh in one single object, but its conception is completely different from the bulk one. In microbulks the multiplication region is thinner

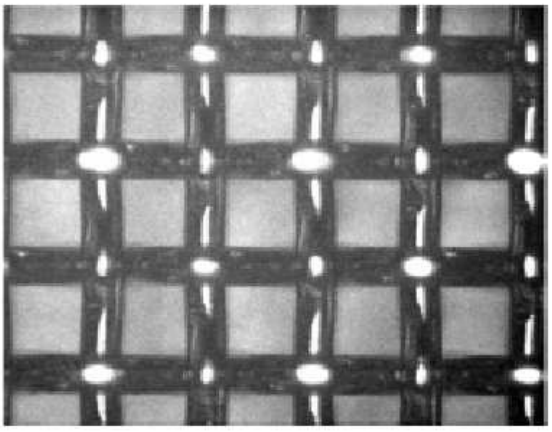

Figure 2. Wire mesh of a bulk. The diameter of the wires is $\oslash$ = 18 μm.

than in bulks, no lamination is performed and the mesh is not a metallic grid existing “a priori", i.e. before the microbulk, but it is created with the microbulk itself. Moreover, as for now[1], the microbulk structure is somehow the complement of the bulk ones, meaning that while the former is empty everywhere except where are pillars, the latter is well represented by the cartoon image of cheese with holes.

One of the manifold applications of micromegas is beam imaging, meaning the study of the beam profile and particle flux. Born as an answer to more powerful accelerators, requiring resistance to really high event rates and extremely precise position and time resolution, these detectors are now used in several experiments [8]. n_TOF and CAST are just two out of numerous examples.

3 MicroMegas detectors at n_TOF

Two micromegas detectors for beam profile characterization have been employed in the years between 2009 and 2013 for beam profile characterization. The differences between the two detectors rely in a dissimilar anodic structure (strips in one case, pixels in the other) and fabrication procedure.

4 First beam profiler: XY-MicroMegas at n_TOF

4.1 Detector description

A micromegas detector with a segmented anode in 2 orthogonal directions, equipped with a neutron/charged particle converter, was developed in the frame of a joint effort of CEA and CERN for the CAST experiment and subsequently modified for the n_TOF Collaboration. This “XY-micromegas" [9] is a circular bulk, with an anode to mesh distance equal to 128 μm. Each side of the squared readout sumperimposed to the detector, 6 cm

[1] studies are being performed in order to reduce the amount of the remaining kapton in microbulks

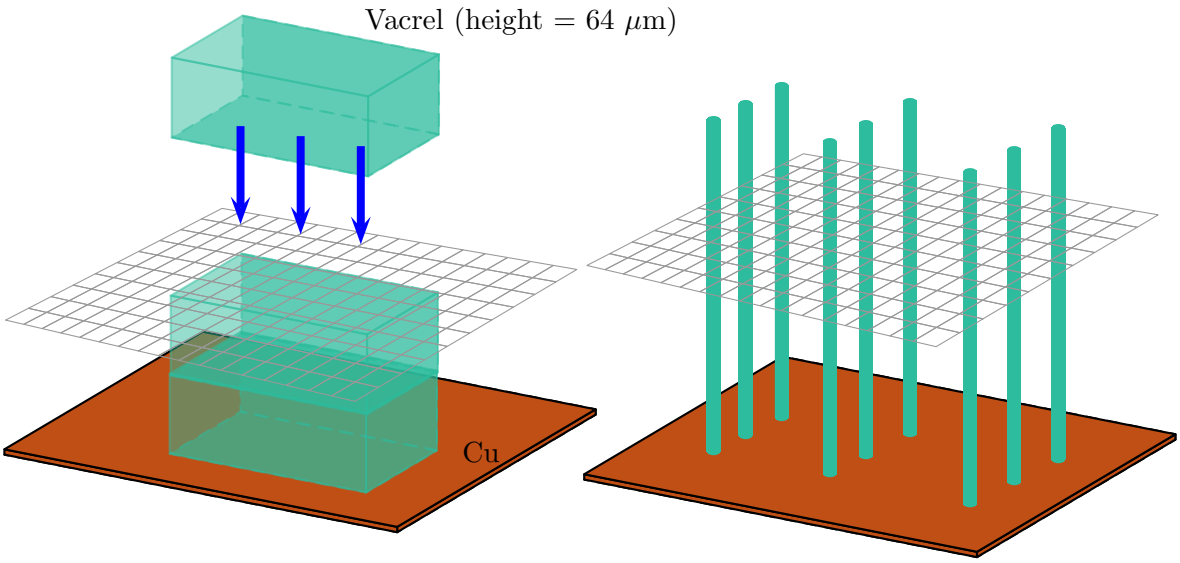

Figure 3. Bulk manufacturing process. The upper left panel shows the superimposition of everything which will be laminated together, while in the right panel is the bulk after the etching technique has been applied.

Figure 4. Microbulk manufacturing process. The left panel shows the result of the first etching, while in the right panel is the microbulk after the last etching has been applied.

long, is divided in 106 strips, allowing a resolution of 0.5 mm as a function of the neutron energy determined by the time of flight. Fig. 5 shows the layout of pads and strips, as well as the interstrip distance.

The side of each pad is rotated by 45° with respect to the side of the detector. For simplicity 7 strips along X and 7 along Y are drawn, but in the reality 106 strips are needed to cover each side of the bulk.

The bulk lays on a PC board and is encapsulated in a cylindrical chamber filled with gas (88% Ar and 10% CF_4 and 2% isobutane) at atmospheric pressure (see Fig. 6). A kapton (12.5 μm) foil stretched and glued on a plastic ring plays the role of the window. A layer of copper (1 μm), facing the gas, is deposited on the kapton foil and connected to high voltage. $^{10}B_4C$ is deposited on this drift and acts as a neutron/charged particle

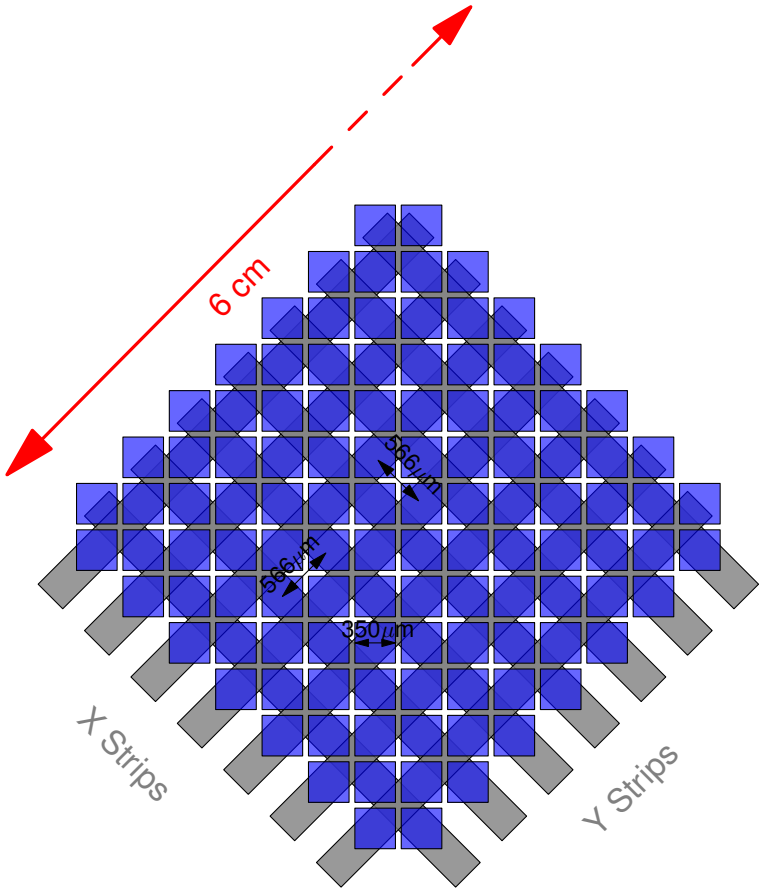

Figure 5. Part of the “XY-micromegas" detector scheme. Pads are 350 μm width, and they are separated by 50 μm gaps, which results in an interpad distance of 400 μm. X strips and Y strips are about 150 μm width. X strips are situated at a different deep inside the kapton layer with respect to Y strips, therefore they do not touch each other.

converter. Given the employment of ^{7}Li and α, created in the reaction ^{10}B(n,α)^{7}Li, as ionizing particles, the drift was positioned at a distance of 4 mm from the mesh.

For reasons linked to the positioning of the electronic connections of the detector on the PC board, only 96 strips for each side, out of the available 106, are employed, resulting in a displacement of the center of the active area of the bulk with respect to its geometrical center (Fig. 7). This shift has to be taken into account when reconstructing the beam image.

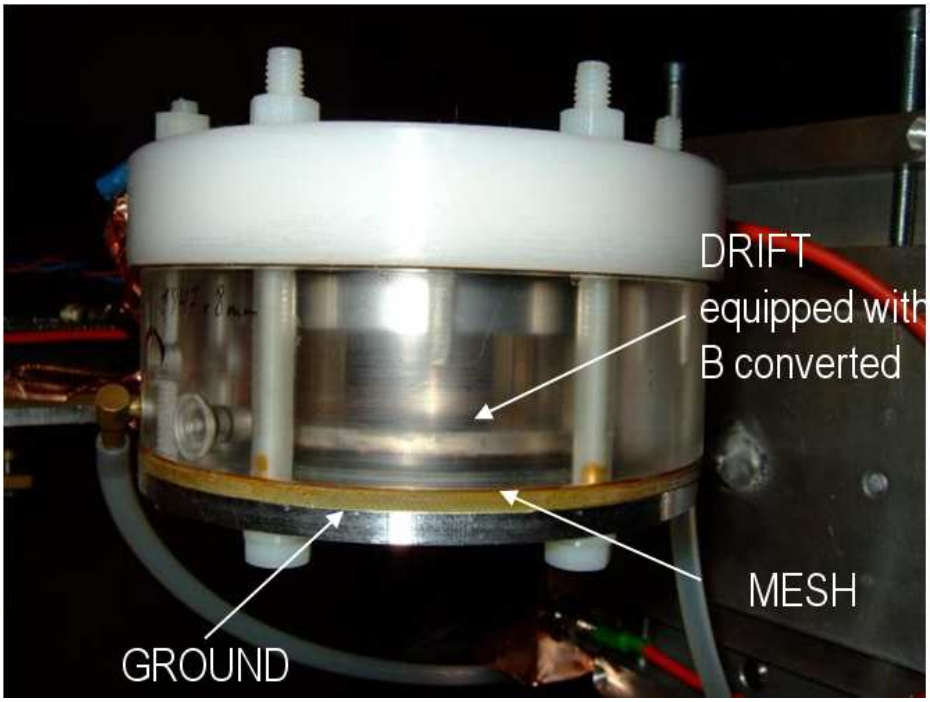

Figure 6. Detector chamber.

4.2 Electronics

Theoretically, given 106 x 2 = 212 strips, 213 channels should be employed to read all signals, i.e. the mesh and each one of the X and Y strips. Given the fact that, as just seen, only 96 strips for each side are used, the number of necessary channels reduces to 193, still a huge number for a time of flight DAQ system. In order to economize the number of employed channels, a different solution was envisaged: each of the 96 strips covering one side of the detector is read in the same moment, and the sampled signals are increasingly delayed and sent to the dedicated electronics via one cable only. In order to translate this concept into a matter of fact, 6 gassiplex cards [10] are used. The 96 tracks from strips for each side of the detector finish in 96 pins visible in Fig. 7. A PC board is plugged into these pins and holds the gassiplex cards, as well as the electronic circuit. Each gassiplex card is a chip powered by a 6 V power supply and reading 16 strips. Each strip is sampled at the same moment, for a certain amount of time and at the same frequency and signals are stored inside the gassiplex chips. A clock is used to deliver to the electronics the stored signals in a certain order (usually corresponding to the strip number). Fig. 8 is a schematic view of a portion of Fig. 9. Black lines represent the input of gassiplex cards, while red lines their output.

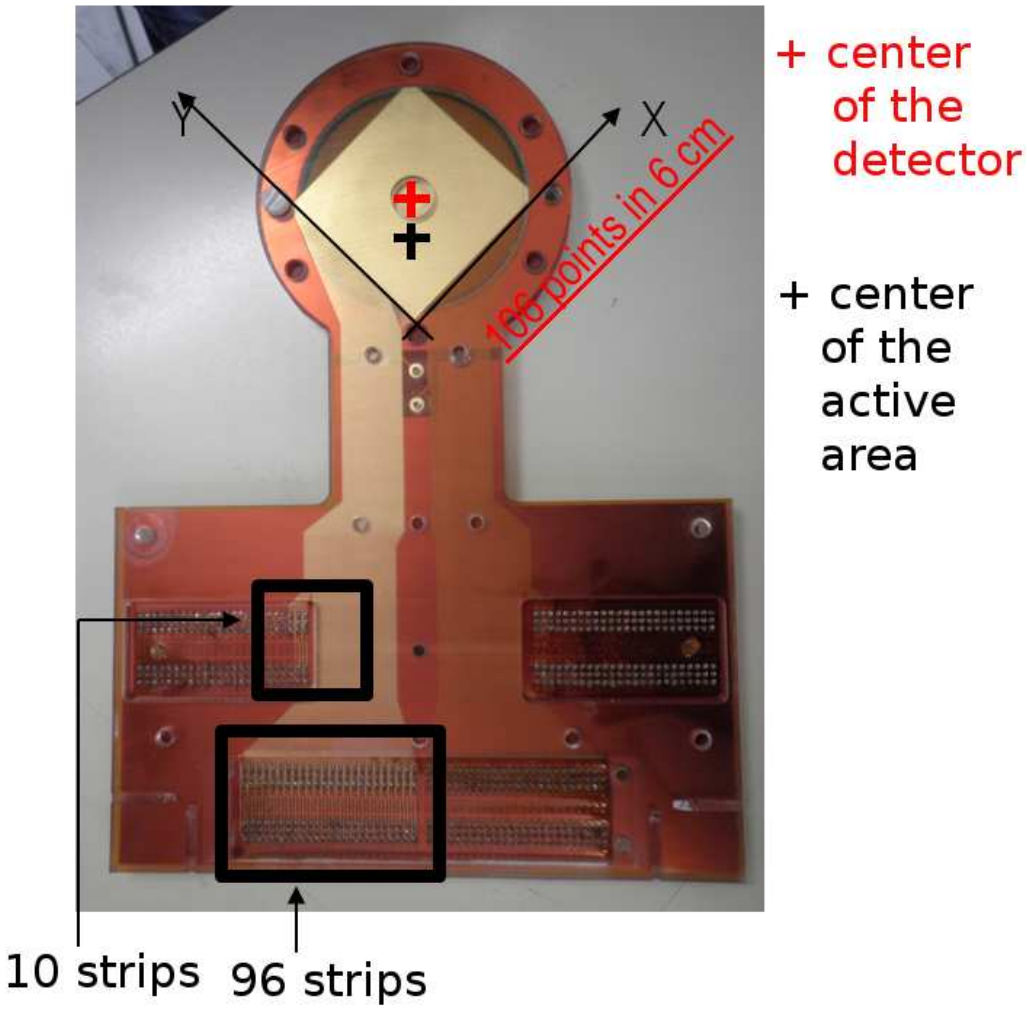

Figure 7. The XYMG bulk and its electronic connection.

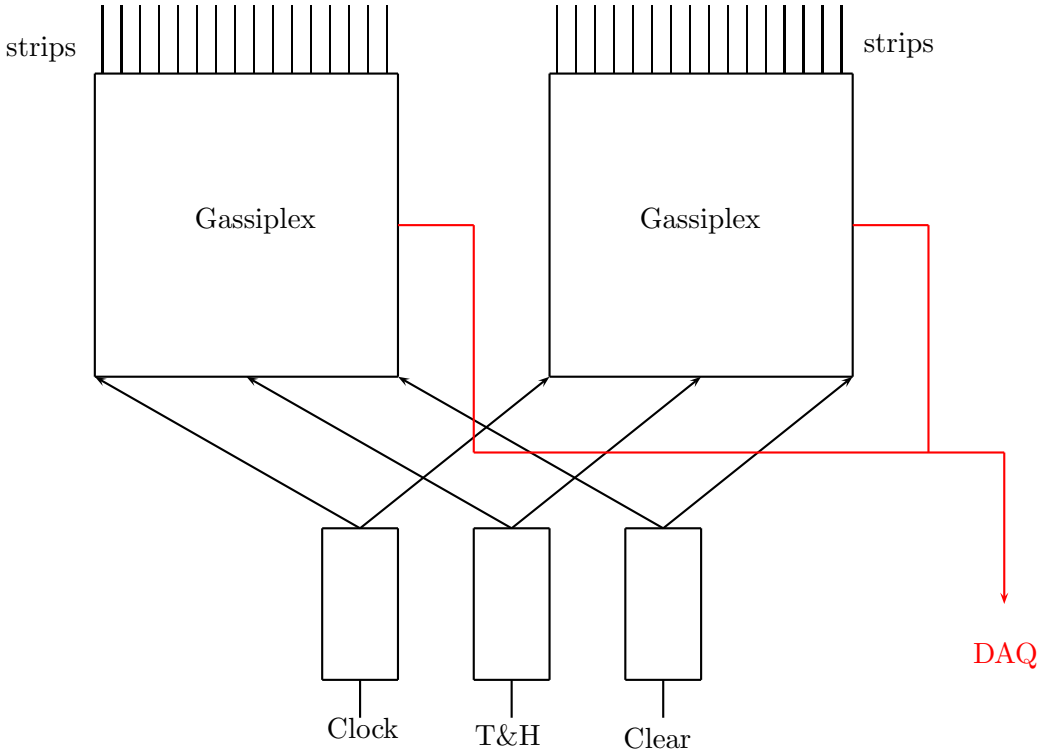

Figure 8. Working scheme of the gassiplex cards.

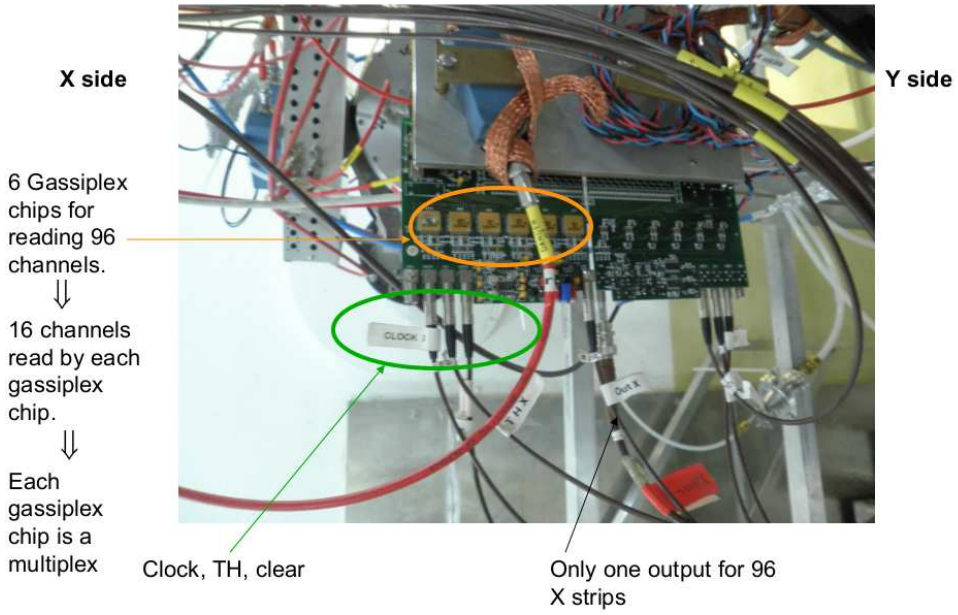

Figure 9. View of the PC board and related electronics.

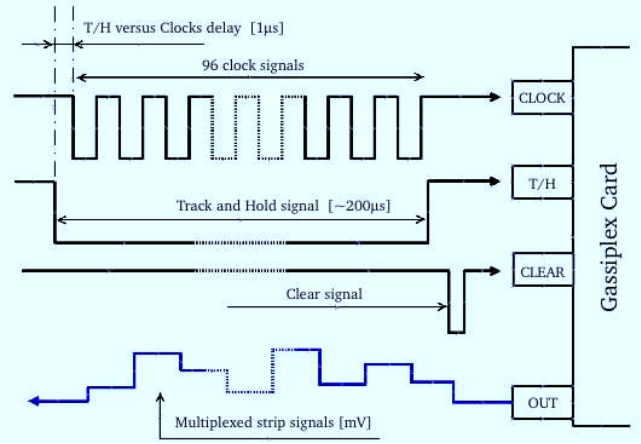

Figure 10. A schematic view of the input and output signals of a Gassiplex card. Figure from ref. [11].

As previously said, each chip reads 16 strips. An externally set time window of a certain temporal length (called Track & Hold, or briefly T&H) is opened whenever a pretrigger signal is given by the proton accelerator (see Analysis routines. Gassiplex cards must therefore receive this information, as well as another parameter (the Clock) saying when delivering the acquired signals from each strip to the DAQ (Data AcQuisition). When the process ends, the memory of the chips has to be reset (Clear). Therefore, each gassiplex card receives as an input both the signals of 16 strips and 3 "working parameters", i.e. T&H, Clock and Clear. The X and Y "circuits" are separate, meaning that 6 gassiplex cards are used for the X strips, and 6 for the Y strips. Moreover 1 T&H, 1 Clock and 1 Clear signals are needed for the X circuit and another T&H, Clock and Clear for the Y. In the end, 1 single output channel is used for the X strips, and another for the Y strips.

At n_TOF, after some tests, it was decided to set a Clock of 2 μs, resulting in a T&H equal to 2 μs x 96 strips = 192 μs. This holds for both circuits (X and Y). Let's consider only the X circuit. The given parameters assure that, after each $^{10}B(n,\alpha)^{7}Li$ interaction, signals are contemporary acquired in the 96 strips for 2 μs. The allocated "time memory" is therefore 192 μs, which coincidences with the dead time and, one after the other, the stored signals are sent to the DAQ.

Fig. 10 shows the input and output signals of a Gassiplex card, and Fig. 11 illustrates in detail how the T&H and clock are generated (in "normal", i.e. not calibration, mode).

Several NIM modules are employed. First the mesh signal is sent to the input of an ORTEC Model 474 Timing Filter Amplifier (TFA), where shaping takes place. The TFA output goes to a Lecroy Model 428F Linear Fan-In/Fan-Out, which duplicates the signal. One output is sent to the DAQ, for recording the mesh signal, while the other one is sent to a LeCroy 621AL Quad Discriminator input to be translated in a logic output. Such binary signal is then transferred to a LeCroy Model 622C Quad coincidence. This

module is in reality a 4 in 1 modules or, more simply said, can be looked at as divided into 4 independent submodules. The first (upper one) receives both the already mentioned binary signal and the T&H status information from the $\overline{out}$ of a second (lower) submodule of a 2 in 1 SEN Dual Timer TU277.

The $\overline{out}$ of the mentioned dual timer is nothing else than the reversed T&H gate, i.e. the pink line of Fig. 10. Therefore the first submo-dule of the Quad Coincidence, in machine language, performs an "&" operation on the 2 received signals and emits a consequent logic output or, in human readable language, checks if when the mesh signal arrives a T&H is already opened or not. In the former case the output will deliver the information "T&H already opened, therefore ignore the mesh signal", while in the latter situation the outcome will pass the message "open a new T&H". Whatever it is, the result of the check is sent to the second submodule of the Quad Coincidence, which receives as a further input a cable coming from a LeCroy Model 222 Dual Gate and Delay Generator delivering the γ-flash time information. An "&" operation is therefore performed by the second Quad Coincidence submodule, to avoid starting a T&H in case the mesh signal was generated by neutrons of energies higher than 1 MeV (corresponding to a tof of about 42740 ns). In the following step, the logic output generated by the second submodule of the Quad Coincidence is sent to the first (upper) submodule of the already mentioned Dual Timer and, from here, to 2 other submodules for triggering or inhibiting at the same time the start of the clock and the opening of a new T&H. As for the clock, a reset signal from the first submodule of the upper Dual Timer is sent to the upper submodule of a 4 in 1 LeCroy Model 429 Logic Fan-In/Fan-Out. Such signal delivers the information "start the clock" or "take no action". The same logic signal delivered to the Logic Fan-In/Fan-Out, passes from the first submodule of the Dual Timer (end marker exit) to the second one "accumulating" a delay of about 800 ns and is then sent to the fourth (lower) submodule of a the Logic Fan-In/Fan-Out. The 2 outputs of such submodule are connected to the X and Y gassiplex cards, for transferring them the final decision about opening or not a new T&H.

A second out from the lower Dual Timer submodule goes meanwhile to one input of the third Quad Coincidence submodule, used for inhibiting the clock once the T&H is closed. The concept is always the same: a logic "&" operation is performed on 2 incoming signals, the former of which mentioned here above, and the latter coming from the $\overline{out}$ of the lower submodule of a second Dual Timer. Therefore the third submodule of the Quad Coincidence checks if the clock occurs during the T&H. If so, the clock is accepted, otherwise it is refused. The logic output obtained as a result is sent to the first submodule of the Logic Fan-In/Fan-Out. This electronic component works in OR mode and sends an OK signal to the first submodule of a second Dual Timer each time it receives a signal either from the reset of the first Dual Timer or from the out of the Quad coincidence. The second Dual Timer regulates the clock repetition and this information is sent to the second submodule of the Logic Fan-In/Fan-Out, which delivers that to the X and Y gassiplex cards.

The signals exiting from the gassiplex cards and, as just seen, the one from the mesh go to the DAQ, consisting of flash ADCs working at a sampling rate of 100 MHz. The

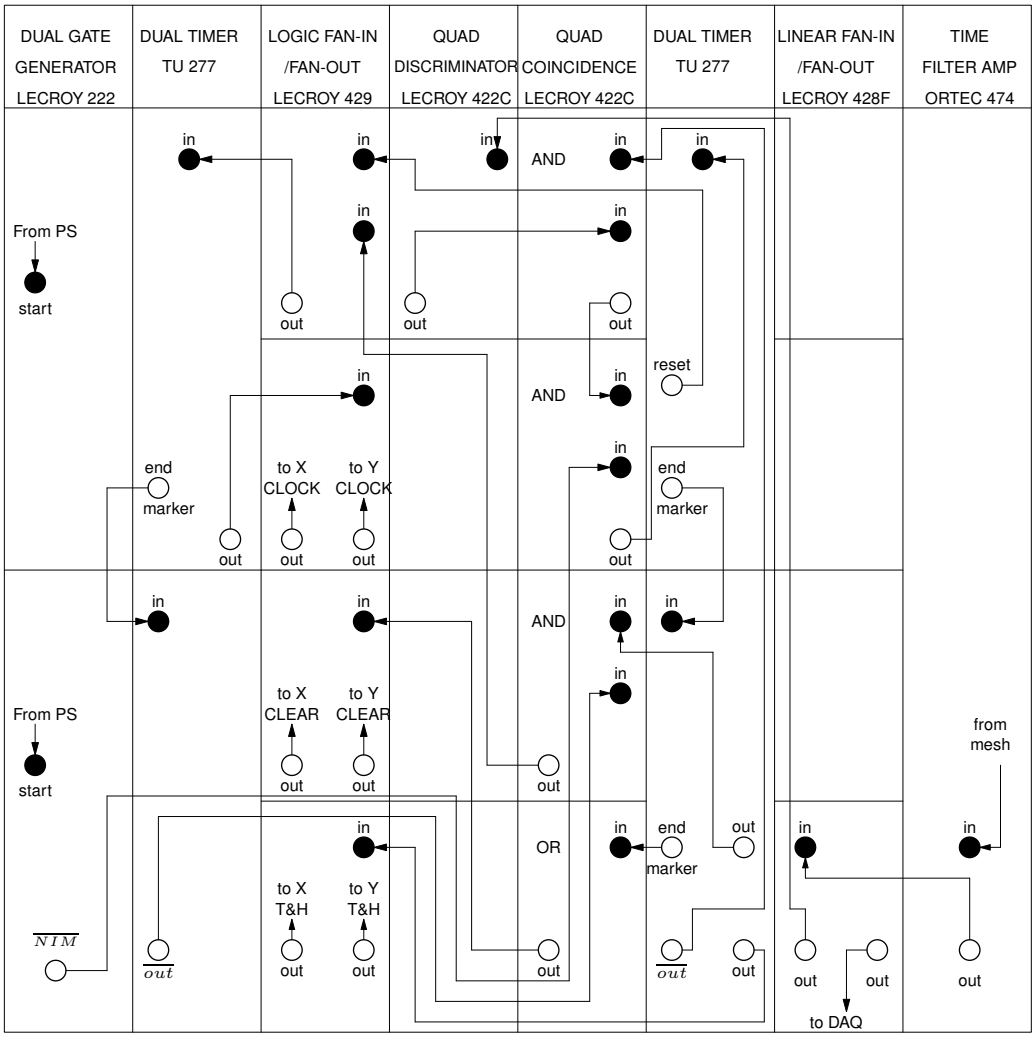

Figure 11. NIM modules employed for creating the T&H, clock and clear signals necessary to operate the gassiplex cards.

obtained digital data are subsequently sent to CASTOR (Cern Advanced STORage manager [12]), where they remain available for off-line analysis.

4.3 Analysis routines

This section reports on the main steps performed by the analysis routines. For the code and a more detailed documentation, see [1]

4.3.1 Preliminary

At the n_TOF facility neutrons are created by spallation reactions induced by a 20 GeV pulsed proton beam impinging on a lead target. Each time a proton bunch is delivered, a pretrigger alerts the DAQ and an acquisition window capable of reading 8 MSamples of data is opened for each channel. Given a sampling rate of 100 MHz used for the XYMG detector, each of its three signals (one mesh electrode, and two GASSIPLEX signals with the X and Y strips amplitude information), is sampled every 10 ns, resulting in a time window of 2^{24} ns or approximately 83 ms for each bunch. From the acquired 2^{23} datapoints by the flash-ADCs, only the waveforms of the signals exceeding a preset threshold due to an event in the detector are stored for further processing. This is called zero suppression. In following a recorded signal is called “signal” or “movie”, in the case of GASSIPLEX signals are also called “track&hold” or “T&H”. In figure 12 this is schematically shown for one single movie, corresponding to a ^{10}B(n,α)^{7}Li reaction caused by one neutron of a certain energy inside the converter.

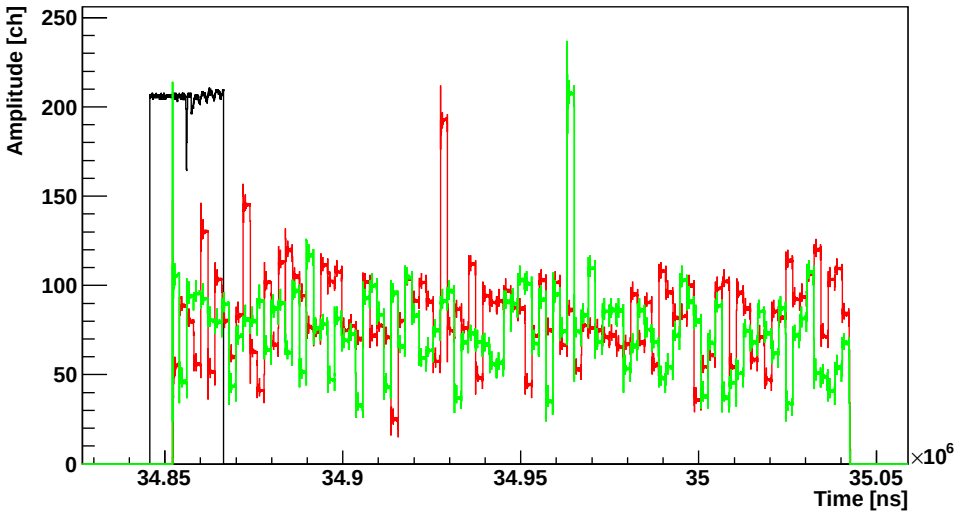

Figure 12. Movie of a normal run put in histogram. Signals in the mesh are in black, those in the X strips are drawn in red and the green line is used for signals in the Y strips.

The “raw data”, which are the zero-suppressed signals sampled by the flash-ADCs, stored on CERN’s storage manager CASTOR together with the voltage, timing and other information, are the basis for further analysis which is done in two separate steps:

1. Raw data processing: extraction of the event information like time, amplitudes, γ-flash, from the raw data including coincidence information. The event information is also called DST (data summary tape) data.

2. Reconstruction of the beam image from the event information (event processing).

Both steps are described hereafter.

4.3.2 Raw data processing

The analysis routines for the XYMG detector start from the raw data. A main routine reads raw data from the three electrodes, i.e. from the mesh (if present), the X strip anode and the Y strip anode. For each selected run, the raw data stored on CASTOR is retrieved, and processed for each selected channel, bunch by bunch, movie by movie. We have used a simplified version of the raw data reading routines. [13].

The sensible pieces of information recovered are the time, the amplitude of the signal in correspondence of this time and the "source" of the signal, i.e. mesh, X or Y strips. The first two quantities are put in a histogram. The histogram is filled for the first movie of the first electrode, passed to a subroutine analyzing that, and then deleted to be recreated and filled again with the information coming from the successive movie of the same electrode and event. Once the first event of the first electrode has been totally retrieved, the following electrode(s) are treated. After all movies of the first event have been processed, the results of the analysis performed by the subroutine, stored as C++ structures, are passed to a different subroutine to be further treated and stored in a TTree keeping memory of the event number for future use. At this point the command is passed back to the main analysis routine. The first movie of the second event is read, put in histogram and processed and everything is repeated. The process finishes when no more data are available and the result of the analysis of a run is a root file containing a TTree.

4.3.3 Raw data processing: Mesh signals

In normal runs, each time a neutron interacts with the ^{10}B converter, a charged particle is emitted and ionizes the gas. Therefore the potential difference between the mesh and the ground varies and a signal in the mesh appears.

In order to determine its amplitude, time, width and area, the baseline is calculated using an implementation of Algorithm D for decreasing clipping window of ref. [14], and then subtracted. A C++ structure is therefore filled with such quantities. A particular role is covered by the first mesh signal of each event of a normal run: soon after a PS pulse starts, protons induce spallation reactions (see more about the n_TOF facility [1]). Though a sweeping magnet and several shieldings are positioned along the neutron beam line, and though the neutron beam line intercepts an angle of 10° with the proton beam line, a strong signal is detected in the mesh. Such signal is produced by electromagnetic radiation and relativistic particles generated in the spallation reaction and is known as γ-flash . The γ-flash serves as a time-reference for the neutron energy calibration.

An example of a typical mesh signal is shown in figure 13 together with the extracted time and amplitude information.

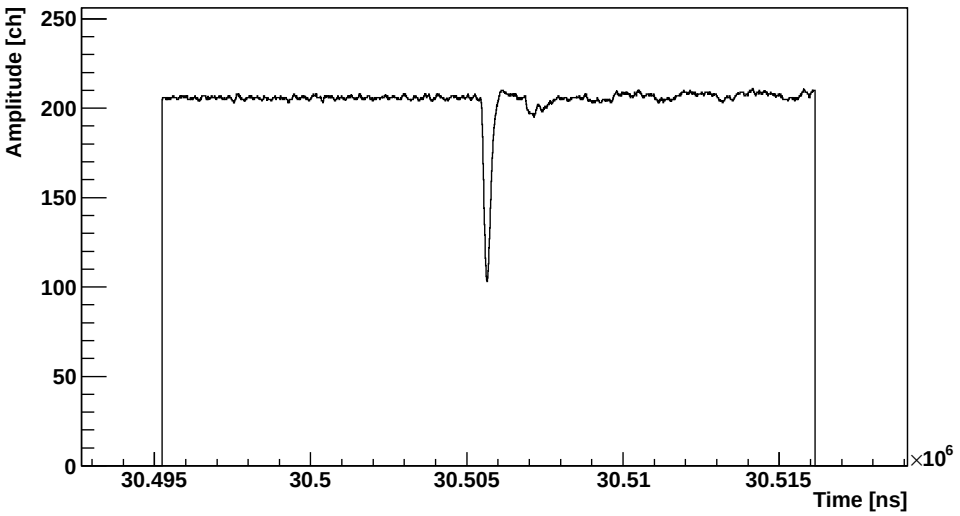

Figure 13. An example of a typical mesh signal.

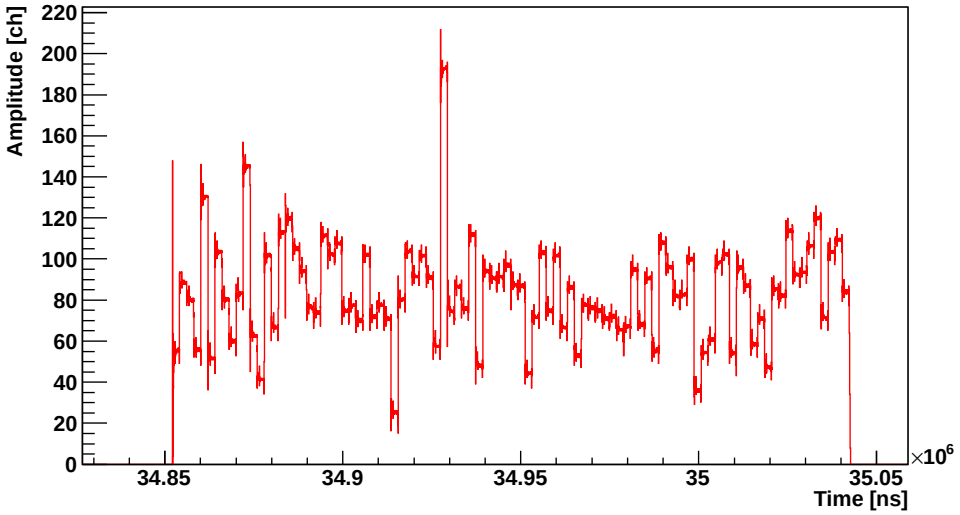

Figure 14. Original signal in 96 X strips.

4.3.4 Raw data processing: GASSIPLEX signals

The X and Y strips raw data are not usual detector signals but GASSIPLEX output signals. Each of the signal amplitudes of the 96 strips are electronically stretched to about 2 μs and with an increasing time delay of also approximately 2 μs. This results in an analog signal (T&H) of roughly $96 \times 2 = 192$ μs, representing the strip amplitudes one after the other as shown in figure 14. This time corresponds also to the deadtime of the GASSIPLEX.

The GASSIPLEX T&H is usually triggered by a mesh signal as in the electronic setup shown in figure 11.This is the case during normal runs with the neutron beam or with a radioactive source. In order to determine the baseline of the detector in each strip (noise level), “pedestal” runs are taken in absence of a source and beam. In this configuration, no mesh signals are produced and the GASSIPLEX is triggered electronically with a fixed frequency of usually 5 kHz.

Fig. 15 shows two movies for a normal run. The picture illustrates also the dead time for the GASSIPLEX signals. If a mesh signal occurs during a T&H, it does not trigger a new T&H.

When processing GASSIPLEX movies, the time window Δt of the signal is determined. Usually the T&H signal is 192 μs long. These signals were still corresponding to 96 strips. In the analysis we accepted signals with $176 < \Delta t < 200$ μs. Then the signal is rebinned in 96 intervals and the amplitude of each of the 96 strips is determined. This is necessary because signals were sampled at a frequency of 100 MHz. This means that for each strip around 200 ((192 μs/96 $\times$100 MHz) amplitude values are stored. The resolution of Fig. 15 is not good enough to allow to distinguish different sampled amplitude values inside the same strip, but by zooming on it, Fig. 16 is obtained, which helps visualizing the concept. Each “step” is a strip, but these steps are not really flat. Signals oscillate around a mean value. In order to obtain an univoque correspondence between a strip and its “average” amplitude value, a rebinning was performed.

Fig. 17 shows the result of the performed rebinning. A structure for X strips is therefore filled with the time start and time end of all X signals as well as with 96 strip amplitudes for each X signal. Y strip movies are processed in the same way, but a decoding has to be applied. This is necessary because of an inversion in the strip numbering due to the employed electronic connections. In the end a C++ structure for Y strips is filled.

When all signals of all electrodes have been analyzed for the same event number, the structures containing the events are processed.

4.3.5 Coincidence determination

For normal runs the coincidence between the mesh and both strip time signals have to be determined The coincidence condition employed was chosen on the basis of the different delays set in the 2009, 2010, 2011 and 2012 runs and states that the mesh signal can start up to 1500 ns before the mesh strip signals or up to 5000 ns after that. Data found in coincidence are saved as branches of a TTree with a same entry number.

For pedestal runs only the coincidence between time signals of the X and Y strips is determined. Again, the coincidence condition employed was chosen on the basis of the different delays set in the 2009, 2010, 2011 and 2012 runs and states that the absolute difference in time between the start of a signal in the X strips and in the Y strips has to be smaller than 1000 ns. As before, data found in coincidence are saved as branches of a TTree under the same entry number.

The final event data are stored in a separate file for each run for further processing.

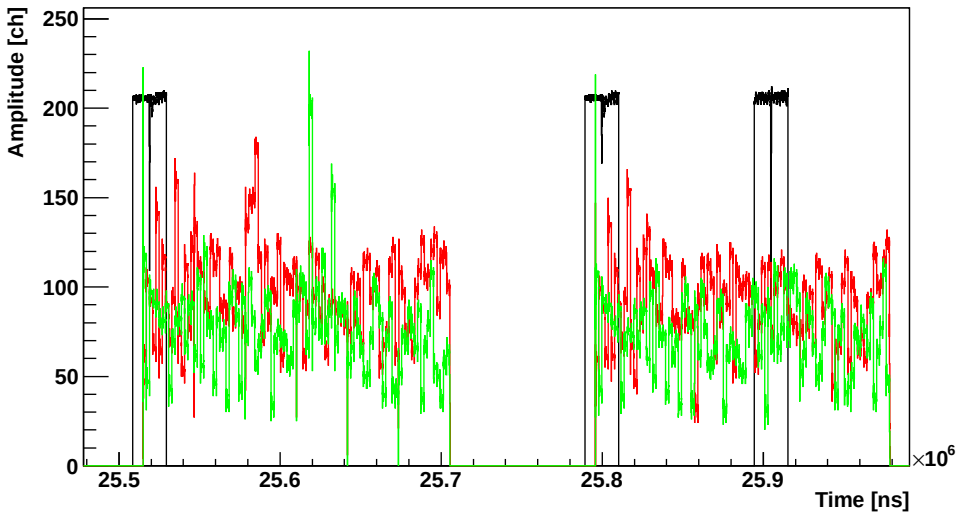

Figure 15. Part of raw data for a normal run put in histogram. Signals in the mesh are in black, those in the X strips are drawn in red and the green line is used for signals in the Y strips.

4.3.6 Event processing

In a second step a different code processes the previously stored event files in order to obtain the beam image. It reads the TTree created in beam presence, plots the durations of signals for X and Y strips and separately fits them with 2 Gaussians. Out of all stored signals, only those whose length is within the average length of X and Y strip signals $\pm$ such length divided by 192 will be considered. This allows to get rid of too short and too long signals, to avoid a mismatch between strip numbers. As a matter of fact, if a signal is much longer than another, what is strip n in one signal, results to be strip $n+1$ in another one and a strip mixing is risked during the final analysis.

At this point, the TTree generated in the previous analysis in beam absence is read and an average amplitude value corresponding to the baseline is determined for each strip. This task is performed by filling, for each strip, a histogram of the amplitude values registered and by extracting the channel number corresponding to the peak position.

Now, for each T&H of the normal run, the real amplitude of each strip is calculated by subtracting to the stored value both its pedestal amplitude and the average amplitude of the pedestal for the 96 strips of that particular T&H. This last component accounts for possible level shifts due to variations of the gains with time. A new Ttree for normal runs, containing the same information as before, but with net amplitude values (i.e. values cleaned from pedestal and offset) for each strip is created.

As a further step, a cluster analysis is performed on each entry for X strips and for Y strips. This consists in determining, for each T&H, the number of strips next to each

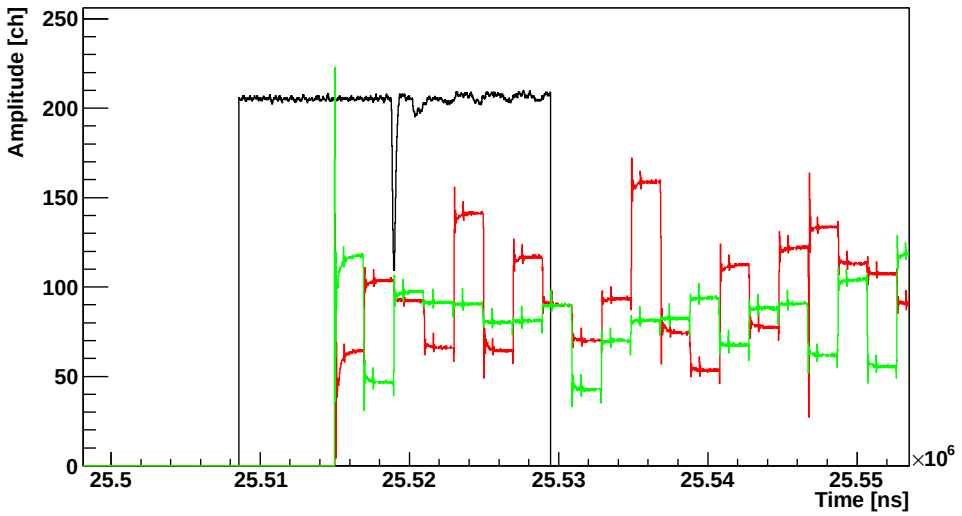

Figure 16. Part of raw data for a normal run put in histogram. Few strips are considered and a sampling rate higher than the strip number is vi-sible.

other presenting a value above a certain threshold and the sum of the amplitudes above such threshold (this sum is proportional to the energy deposited in the cluster). If the former number, known as multiplicity, is not strangely high, and the latter is not too low, the "fired" strip is determined thanks to a center of charge analysis. If more than one acceptable (in terms of multiplicity and energy deposited) cluster is found in the same T&H, the T&H is rejected. A position in space is associated to each fired strip by considering the active length of one side of the XYMG detector (i.e. 96 x 566 μm = 5.434 cm) and by calculating for a precise j: (-5.434/2 + j*strip_length/2) cm, with j = strip number -1. This means that, in a first moment, the mismatch between the active and the geometrical area is not corrected for. A new TTree keeping memory of the run number, event number, T&H number, trigger time,...is created and updated with the cluster information.

For a same run, event, T&H and time, the couple of X and Y fired strips has to be determined and their previously calculated position inside the detector has to be turned into spatial coordinates relative to the active area and orientation of the bulk in the experimental area (EAR). The strips intercept in fact an angle θ = -225° with the horizontal and vertical directions of the EAR (see Fig. 18), therefore the relation between the old and new (prime) coordinates is:

$$\begin{bmatrix} X' \\ Y' \end{bmatrix} = \begin{bmatrix} \cos\theta & -\sin\theta \\ \sin\theta & \cos\theta \end{bmatrix} \cdot \begin{bmatrix} X \\ Y \end{bmatrix} + \begin{bmatrix} H_{shift} & 0 \end{bmatrix} \cdot \begin{bmatrix} 1 \\ 0 \end{bmatrix} \quad (1)$$

where the mismatch between the active and geometrical area of the detector has been corrected for by introducing an horizontal shift (H_{shift} term).

The γ-flash is used as reference to find the energy of the neutron inducing a signal in

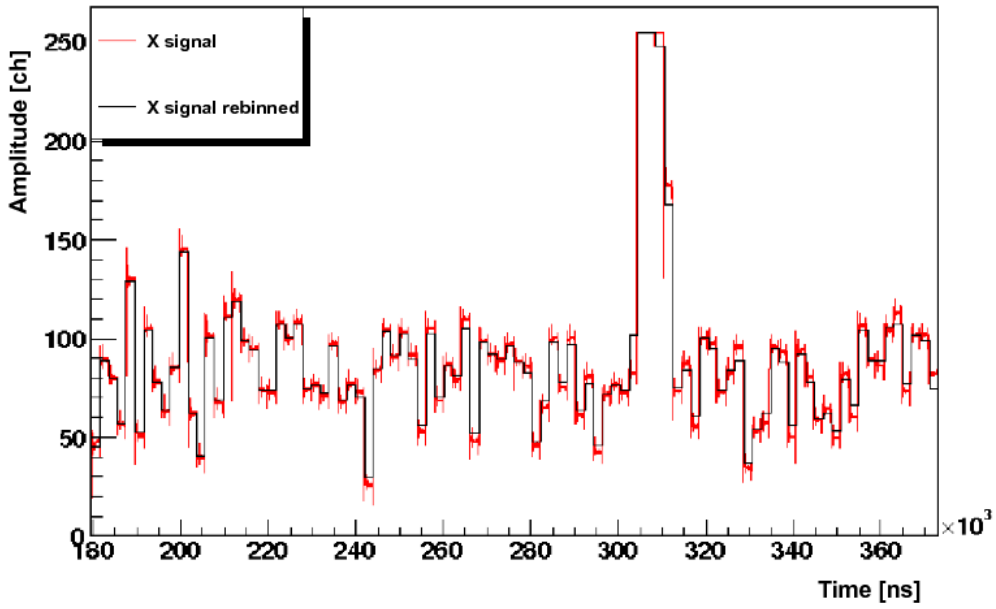

Figure 17. Rebinned and original signal in 96 X strips.

the mesh so that the beam image can be reconstructed for all or for some selected neutron energies. By projecting the beam images along the Cartesian reference axis (X' and Y'), a study of the beam profile as a function of the incident neutron energy can be performed.

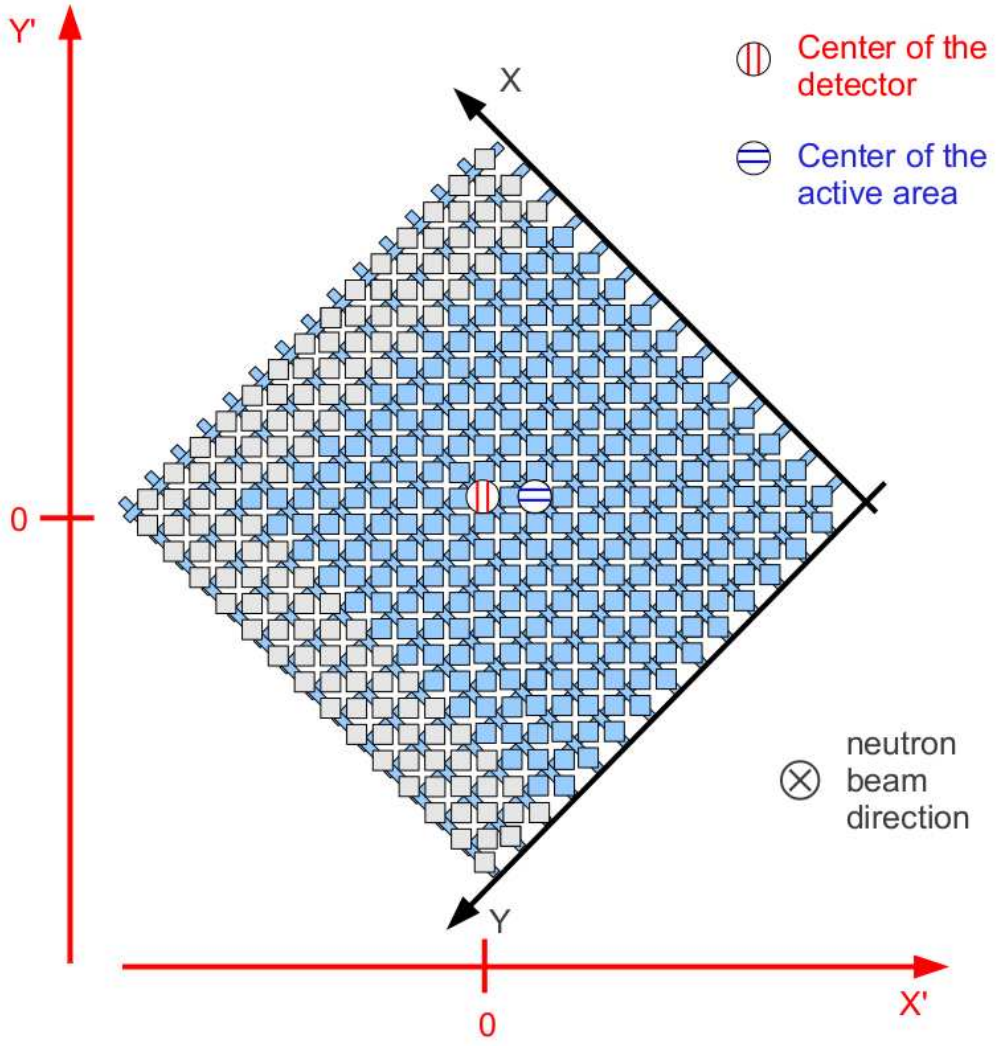

Figure 18. Schematic layout of the orientation of the detector with respect to the experimental area (EAR). For simplicity only few strips, and not 106 along each side, are drawn. Light blue pads represent the active area, while grey pads lay in the unused region of the detector.

4.4 Simulations

An extensive study of the characteristics of the n_TOF neutron flux generated by spallation reactions of proton pulses on the lead target has been performed at CERN by means of coupled FLUKA and MCNP Monte Carlo simulations [15]. The implemented geometry is extremely detailed and accounts for all the components of the facility, including walls, and flooring and different shieldings, from the spallation target up to the moderator system. The results of such simulations at the entrance of the vacuum tube are used as the input information of a neutron transport routine performing the neutron propagation through the beam line up to a plane situated 183.15 m downstream with respect to the spallation target. By collecting the hitting point of the neutrons on the plane, the beam image, profile and interception factor are extracted.

Few additional Monte Carlo simulations have been performed in CEA to account for the presence of the beam profiler in the neutron beam in particular experimental layouts. In some cases the results of the simulations performed in CERN in terms of the neutron beam profile at 183.15 m downstream with respect to the spallation target and in terms of the neutron flux before the aluminum window closing the neutron tube have been used as the new input primary source. More details follow in this report.

4.4.1 Validating the center of charge method: stopping power

A minimal geometry, consisting in a cylinder of 5 cm radius and 4 mm thickness filled with Ar (88%), CF_4 (10%) and C_4H_{10} (2%) was implemented.

The Q value of the n + ^{10}B $\rightarrow$ ^{4}He + ^{7}Li reaction is 2.31 MeV if ^{7}Li is left is in its ground state. When thermal neutrons interact with the converter, the two charged products are emitted in opposite directions, with kinetic energies Tα = 1.47 MeV and $T_{^7Li}$ = 0.84 MeV. Their range in the gas was calculated with SRIM and compared with the results from the simulations.

Fig. 19 shows the energy deposited by 1.47 MeV alpha particles according to SRIM, FLUKA, MCNPX and GEANT4. The difference in the ranges depends on the use of different algorithms, but also on the setting concerning the energy threshold below which alpha particle transport is not performed anymore. In FLUKA such threshold was set to the thermal point, in MCNPX to 1 keV and in GEANT4 the default settings of the Livermore model were used. By varying the value of this threshold, the range of the ^{4}He nuclei in the gas can be slightly tuned. The differences in the amount of energy deposited per unit length in the low energy loss region instead depends only on the algorithms implemented in the Monte Carlo codes and can not be modified. Since SRIM results are based on a huge amount of experimental data, the output given by this computer program is considered as a reference.

Fig. 20 shows the energy deposited by 0.84 MeV ^{7}Li nuclei according to SRIM, FLUKA, MCNPX and GEANT4. The same considerations as before apply.

The results of the Monte Carlo Simulations highlight the trend of the energy deposited by αs when progressing in the gas mixture employed in the experiment. As expected, for

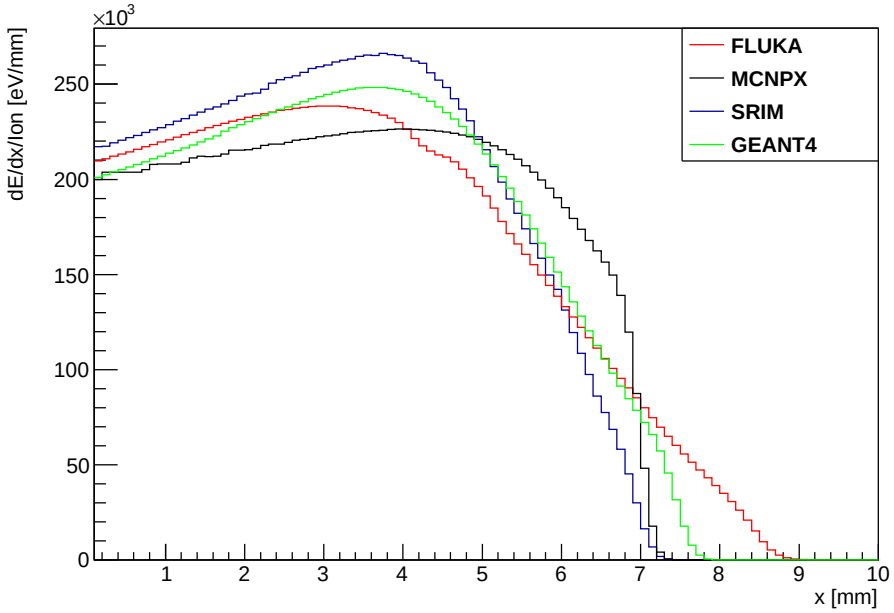

Figure 19. Energy deposition of 1.47 MeV alpha particles in Ar (88%), C_4H_{10} (2%), CF_4 (10%).

higher incident kinetic energies the maximum of the stopping power is reached after the particle travelled some distance in the gas, while for lower incident kinetic energies the stopping power is already at its maximum at the beginning of the track. We recall that the anode of the micromegas detector used for the beam profile characterization is segmented in X and Y, therefore in normal conditions the signal in each strip is proportional to the corresponding -dE/dx at the strip position. We moreover remind that our goal is the beam profile characterization, meaning in practice that for each incident neutron undergoing a n + ^{10}B $\rightarrow$ ^{4}He + ^{7}Li reaction, we are interested in the determination of the interaction point. In the light of the above considerations, Fig. 19-20 suggest that it is not possible concluding that the coordinate of the strip showing the highest signal amplitude is the position where the neutron stroke the converter, because this is true only sometimes. It is instead more correct to perform the center of charge analysis. Such procedure, as a matter of fact, always results in a mistake in the determination of the interaction point. Thanks to the fact that statistically half of the times the value of the interception point calculated this way is underestimated and half of the times overestimated, the differences between the correct and determined coordinates cancel out and complexively, for a significative amount of neutron, the reconstructed beam profile coincides with the real one.

4.4.2 Energy deposition

As will be shown in §5, during the years 2009 - 2012 the XY - beam profiler has been operated in different conditions: the voltages applied to the electrodes were not always

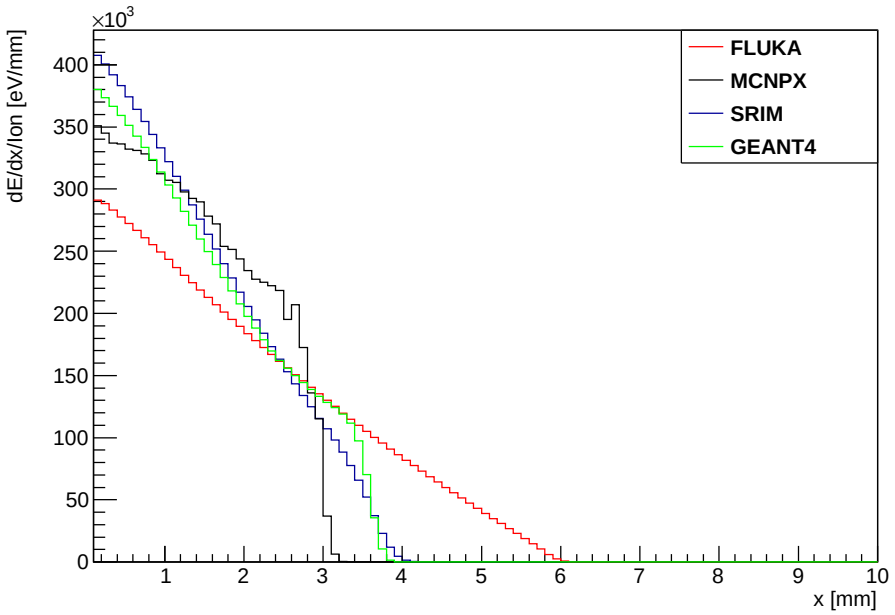

Figure 20. Energy deposition of 0.84 MeV ^{7}Li particles in Ar (88%), C_4H_{10} (2%), CF_4 (10%) according to different MonteCarlo codes.

the same, and two neutrons to charged particle converters have been employed. Out of all the layouts, only few have been selected for a comparison between experimental data and Monte Carlo results. Each time details are given.

A simulation to check the amount of energy deposited by ^{4}He nuclei and ^{7}Li particles in the gas have been implemented with GEANT4. The choice of this code was performed on the basis of the results obtained in the previous paragraph. The primary particles are neutrons, with energy sampled from the 2009 n_TOF neutron flux. The neutrons are shot straight against the converter (details below), therefore no beam divergence is considered. Anyhow the starting position of each neutron in the plane orthogonal to their directions is sampled, as a function of its energy, from the neutron beam profile obtained by the simulations performed in CERN.

A cylinder of 3 cm radius and 2 μm thickness composed by B_4C (enriched 100% in ^{10}B) is inserted in a cylinder of 5 cm radius and 4 mm thickness filled with Ar (88%), CF_4 (10%) and C_4H_{10} (2%). The internal and external cylinders have one overlapping base, as shown in Fig. 21.

The results of the simulations are reported in Fig. 22, where the different contributions to the total energy deposition are highlighted.

In optimal conditions, a proportionality between the energy lost by a particle passing through the gas and the sum of the amplitudes of the signals in all the anodic strips following the passage of such particle is expected. Therefore we give a look to the experimental

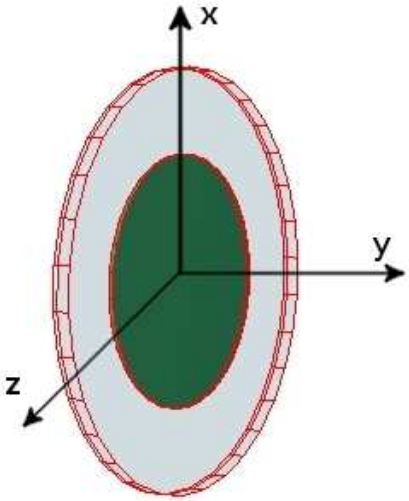

Figure 21. SimpleGeo view of the simplified geometry implemented for the simulations: the ^{10}B converter and the 4 mm (drift to mesh gap) thick ionization chamber. The picture is not in scale.

data.

Some strips in the Y direction are not properly working. Moreover, the gain in the X strips is different from the gain in the Y strips. Because of these two reasons, when we plot the sum of the amplitudes of signals generated in the X and Y strips separately for several events, the 2 curves have the same shape but do not superimpose (see the red and green curves in Fig. 23). We still remind that the final goal is the determination of the point where the incident neutron stroke the converter. Since a point on a plane is defined by two coordinates, we need that for every single event at least one strip in each one of the two orthogonal directions of the detector shows a signal above noise level. If contrary case, the signal is discarded. The baseline determination was carried out in beam absence (pedestal runs) by fitting the average signal amplitude in every strip of the detector with a Gaussian. This gave a mean value of the baseline level and its fluctuation (σ), different for every strip. A signal was considered to be real when its amplitude was at least 5 σ above the baseline. Fig. 23 shows the sum of the amplitudes of the real signals in the X strips (red), in the Y strips (green), in the Y strips after correction for the different gain and missing strips (light blue) and in all the anodic strips (X+Y) before (dark blue) and after (pink) correction for the different gain and missing strips.

In order to compare the total energy deposited in the gas according to the performed simulations and in the reality, it is necessary to add to the GEANT4 results the resolution of the detector. A resolution of 9%, based on average values in literature, was considered. Fig. 24 shows the good agreement between GEANT4 simulations and experimental data, after calibration of the latter on the former. Since in the simulations all the strips are considered to have the same gain and performance, for the experimental data the sum of

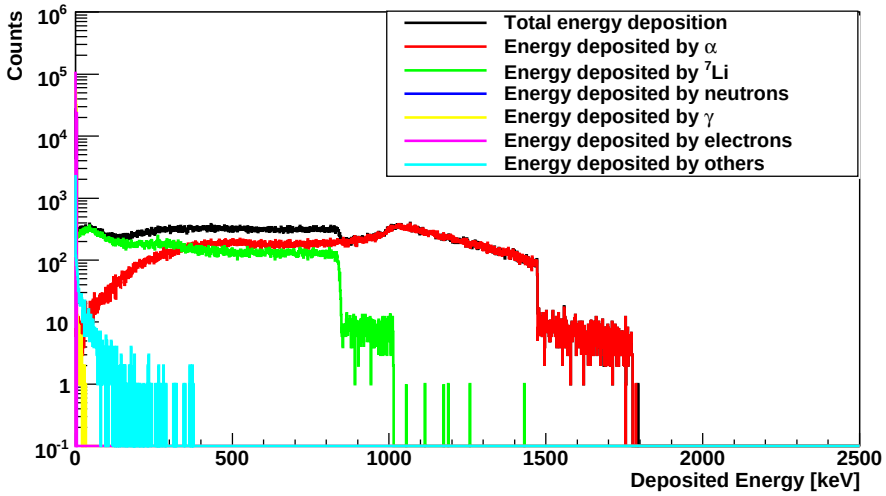

Figure 22. Energy deposited by different particles in C_4H_{10} (2%), CF_4 (10%) according to the performed simulations.

the signals detected in the anodic strips (X+Y) after correction have been used.

The amplitude of a signal in the mesh of a micromegas detector is proportional to the energy lost by a particle passing through the gas and therefore, the distribution of the mesh amplitudes should reflect the distribution of Fig. 22. Fig. 25 reports the amplitude of the signals recorded by the mesh for a specific run (run 9167) after optimization of the applied voltages had been achieved. The smaller mesh amplitudes were discarded because of a threshold imposed to distinguish real events from noise. This picture resembles the light blue curve of Fig. 24, thought the ^{7}Li peak has smaller width because a threshold was applied to the experimental data.

During the measurement campaigns covering the years from 2009 to 2012, a flux monitor [16] was sometimes interposed in the neutron beam before this could intercept the profiler. The flux monitor consists of 2 migromegas detectors of microbulk type, enclosed in a gas chamber and equipped each one with a neutron to charged particle converter (^{235}U and ^{10}B respectively, in order to cover different energies of the neutron spectrum) . In addition, a subtle ^{6}Li foil sandwiched between two carbon layers is always in the beam [17], being the converter of a fixed flux silicon monitor positioned just before the neutron beam exits the beam line. These detectors were chosen at n_TOF because of their negligible impact on the neutron beam. In order to estimate the level of neglibility of their presence, an additional GEANT4 simulation was performed. Every material intercepting the beam was implemented in the geometry. On the other side, the walls, floor and ceiling of the experimental area are absent. Fig. 26 shows a comparison between the energy deposited in the beam profiler by neutrons travelling only through the detector itself and the energy deposited in the beam profiler by neutrons travelling through the flux monitors, their windows, and the beam profiler itself. The two curves are normalized for

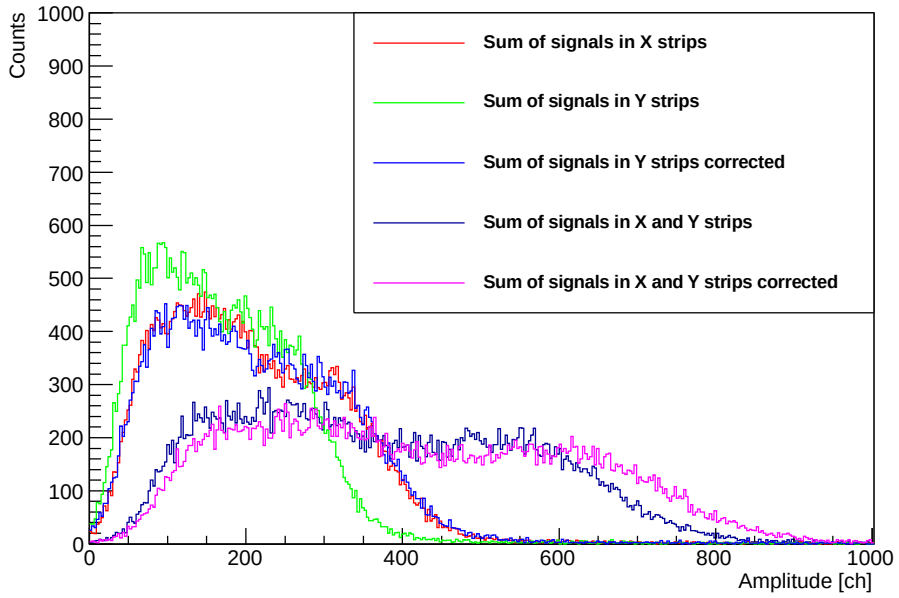

Figure 23. Sum of the amplitudes in the anodic strips along the X direction (red), along the Y direction (green), along the Y direction after applying a correction for different gains and and missing strips (light blue), in all the anodic strips (dark blue) and in all the anodic strips after applying a correction for different gains and and missing strips (pink) for run 9167, after the pedestal and offset subtraction have been performed

the same number of neutrons. As expected the presence of the flux monitors almost does not affect the neutron beam, accounting only for a reduction of 7.6% of the neutron flux.

Up to here the printed board circuit (PCB) housing the detector and its aluminum support were discarded. An additional GEANT4 simulation was implemented to test the role of these elements. The incident neutrons, sampled as usual from the 2009 n_TOF flux and profile, were shot through the flux monitors, windows, ... and beam profiler up to a 2.3 mm glass epoxy PCB (3% Cu + 3% kapton to account for the readout. Out of the remaining 94% glass epoxy, 47.2% was SiO_2 and 52.8% H_2C_2. All percentages are meant in mass fraction) and a 2.5 mm aluminum support. The total energy deposited in the gas increased by 16% with respect to what previously observed for the same number of primary neutrons. The shape of the spectrum of the energy deposited in the gas did not change and looked exactly like Fig. 26, but rescaled in the ordinate values. By scoring the energy deposited by different particles it was remarked that the increase in the deposited energy was almost totally due to an increase of the α particles and ^{7}Li nuclei in the gas. This was easily explained by the presence of hydrogen in the PCB. When a primary neutron is shot, it can interact with the ^{10}B and create charged particles. If this does not happen, the neutron crosses the gas, where it can undergo a nuclear recoil or proceed up to the printed circuit board to be backward scattered by the hydrogen (and less likely by the other elements composing the PCB). In such case, the neutron is less energetic after

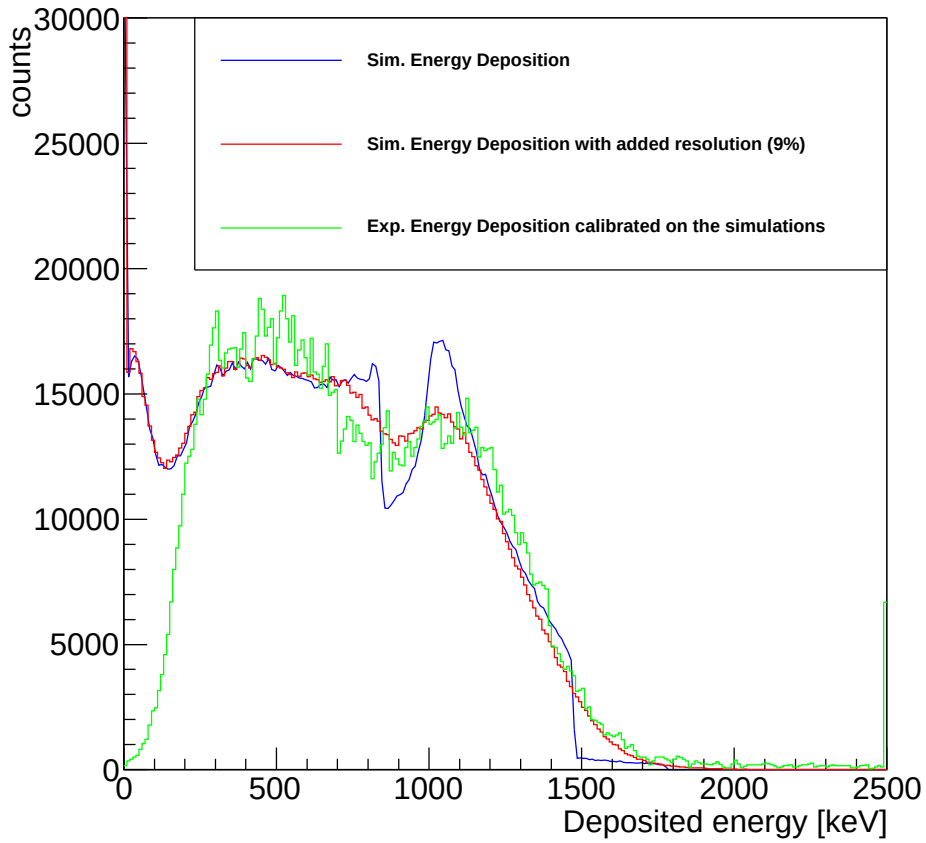

Figure 24. Proportionality between the energy lost by a particle passing through the gas and the sum of the amplitudes of the signals in all the anodic strips following the passage of such particle.

the scattering reaction than before that. The backscattered neutron has now and additional opportunity to strike the converter (being neutral in charge, it can move against the electric field direction) and, given its lower energy, a higher possibility to undergo a n + ^{10}B $\rightarrow$ ^{4}He + ^{7}Li reaction. roughly speaking, in half of the cases following such reaction, the α particle will enter the gas while the ^{7}Li will be stopped in the converter or by its backing, and in half of the cases the opposite situation occur. Of course, the backscattered neutron can instead undergo a nuclear recoil, but the cross section for such reaction is lower than the one for the n + ^{10}B $\rightarrow$ ^{4}He + ^{7}Li reaction. Moreover the mean free path in the gas is longer than in the converter. Therefore after the scattering on the PCB, it is the neutron interaction with the converter that dominates the energy deposition, just like before the scattering, as visible in Fig. 22. This explains why the shape of the curve of the energy deposited in the gas is not affected by the presence or absence of the PCB.

On the contrary, the PCB plays a key role on the beam image, as will be explained

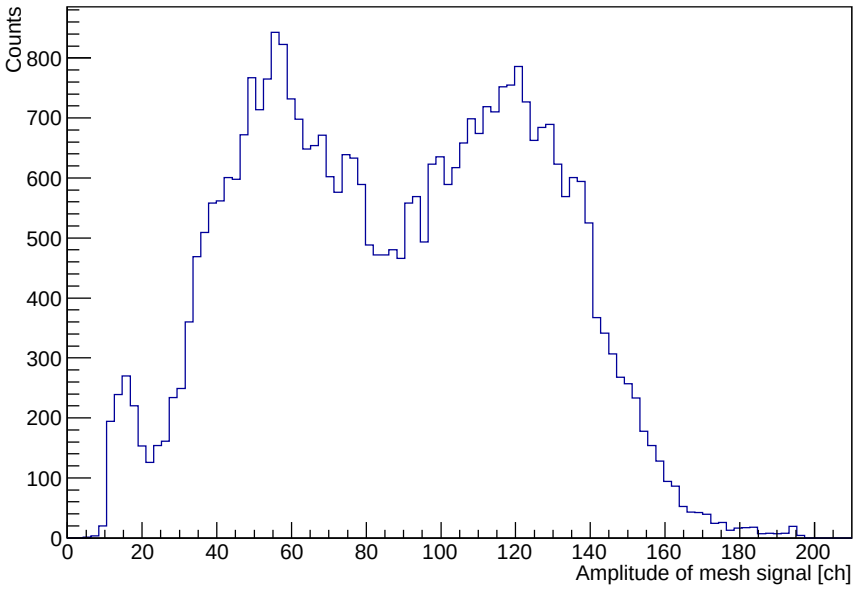

Figure 25. Mesh amplitude distribution for run 9167.

later.

4.4.3 Multiplicity

When a particle ionizes the gas in the micromegas detector, electron-ion pairs are created and drift in opposite direction under the influence of an applied electric field. In principle each drifting charge contributes to the signal created in the mesh. In reality, dealing with time of flight measurements and therefore with the necessity of high time resolutions, only fast signals are accepted (low shaping time) and electrons thus play a dominant role. Electrons are created all along the track of the ionizing particle. The electrons generated in the gas between the drift and the mesh, drift parallely to the electric field towards the mesh because the voltage set in the drift is more negative that the one set in the mesh. In this region, the electric field is strong enough to suppress recombination and allow all generated electrons to reach the mesh, but too weak to permit charge multiplication. The relative weakness of the electric field allows the collisions between electrons and gas molecules to influence the motion of the electrons while drifting towards the mesh along the field lines. A velocity component transversal to the electric field therefore displaces electrons in a direction parallel to the mesh plane (transversal diffusion).

After reaching the mesh, if voltages are properly set, the electrons pass through the holes, drifting towards the anode. In this region the electric field is so strong that the transversal diffusion plays no role at all. The electrons induce a signal in the strip towards which they are moving. It thus follows that the number of strips presenting a signal above electronic noise, called ‘multiplicity’, is a function of the direction and range of

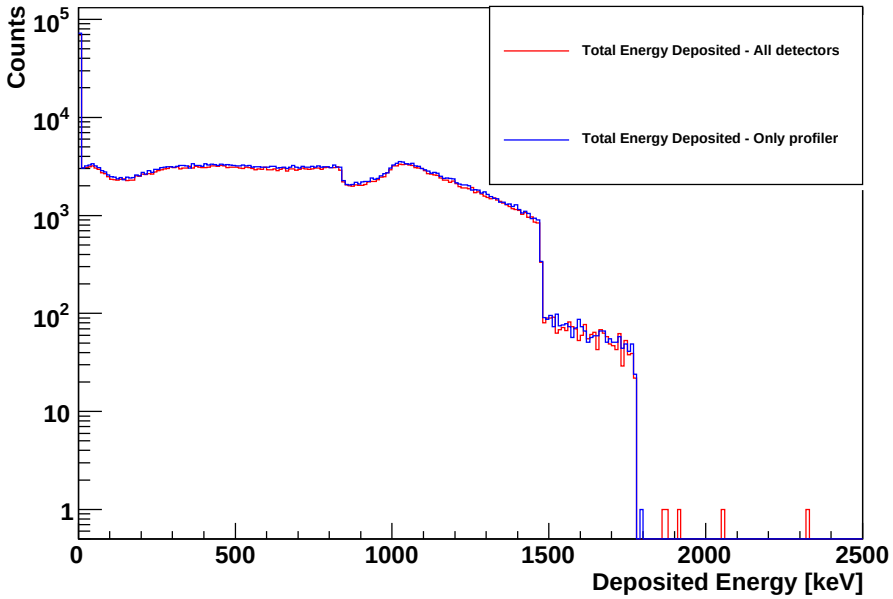

Figure 26. Comparison between the energy deposited in the gas of the beam profiler when the neutron beam passes only through it and the energy deposited in the gas of the beam profiler when the material in the beam between the beam profiler is considered (GEANT4 simulations).

the ionizing particle, of the gas composition, pressure and temperature and of the electric field.

A GEANT4 simulation to determine the distribution of the number of strips presenting a signal due to gas ionization in the micromegas detector has been performed. The aluminum window of the beam line and the flux monitor in front of the beam profile have been considered, as well as the PCB. Moreover the implementation of the two micromegas detectors in the second geometry (flux monitor and beam profiler) is detailed, accounting for whatever layer of material (kapton, ^{235}U, ...) in the beam. The source particles are the neutrons. Their energy is sampled from the neutron flux evaluated before the aluminum window closing the beam line and their starting position on a plane parallel to the walls of the experimental area is modelled according to the beam image as a function of the incident neutron energy obtained by the simulations performed in CERN.

In order to compare the results of the simulation with the experimental ones, it was necessary to keep in mind how the former and the latters had been obtained. As for the experimental results, for each neutron beam the signals in the strips were cleaned from the electronic noise and from possible offsets. Theoretically this operation should end with all the strips, but the ones in proximity of the interaction point of a neutron with the ^{10}B converter, showing a signal of 0 amplitude. In reality, since the background level that is subtracted is a fix value (different from strip to strip), while the background

level itself oscillates, this procedure ends with all the strips, but the ones in proximity of the interaction point of a neutron with the ^{10}B converter, showing a signal close to 0 amplitude. This “close to zero” can be quantified with the uncertainty with which the pedestal is known. This is why a threshold has to be imposed in order to discriminate this residual signal from real signals. The sum of the number of strips showing a signal whose amplitude is larger than 5 times the uncertainty with which the pedestal level is known (σ) gives the multiplicity of a cluster for each event.

Dealing with simulation results, the background noise is absent. In addition GEANT4 does not account for electron diffusion, which had to be considered in a second step, processing the results of the simulation with a routine. The energy deposited by charged particles created after the neutrons strike the converter, as well as the one due to the nuclear recoil caused by high energetic neutrons colliding against the gas molecules, was sampled in different points along the particle tracks. For each point, the deposited energy was converted in number of electrons, that underwent diffusion. For a gas mixture of Ar (88%), CF_4 (10%) and C_4H_{10} (2%) at atmospheric pressure and room temperature, the transversal diffusion of electrons moving in an electric field of 375 V/cm was calculated with Magboltz [18] v.10.0.1 and resulted $193.272 \pm 9.837 \mu\text{m}/\sqrt{cm}$. The number of electrons crossing the mesh in correspondence of a certain strip had to be multiplied for a constant factor taking into account the avalanche created by each electron in the region between the mesh and the anode. The calibration performed in the previous paragraph allowed to convert the energy collected by each strip (equal to the number of electrons times the ionization energy of the gas) into channel format. A residual background of 0 amplitude and uncertainty equal to the experimental σ (channel format) with which the pedestal is known, had to be added in each strip in order to make experimental data comparable with simulations. In the end, a threshold equal to 5 experimental σ (channel format) was applied, and the strips presenting an amplitude larger than the threshold were grouped in clusters.

The distribution of the multiplicities obtained with a threshold of 5 σ in the X strips is peaked at a value equal to 3 both in experimental and simulation results, as shown in Fig.. 27. For the experimental results, a run with the center of the beam image in a position not different from what shown in Fig. 35 and Fig. 36 was considered. Because of a not reading strip along the Y direction of the detector (see Fig. 36), the experimental distribution of the multiplicities obtained with a threshold of 5 σ in the Y strips peaks instead at a lower value (value equal to 2).

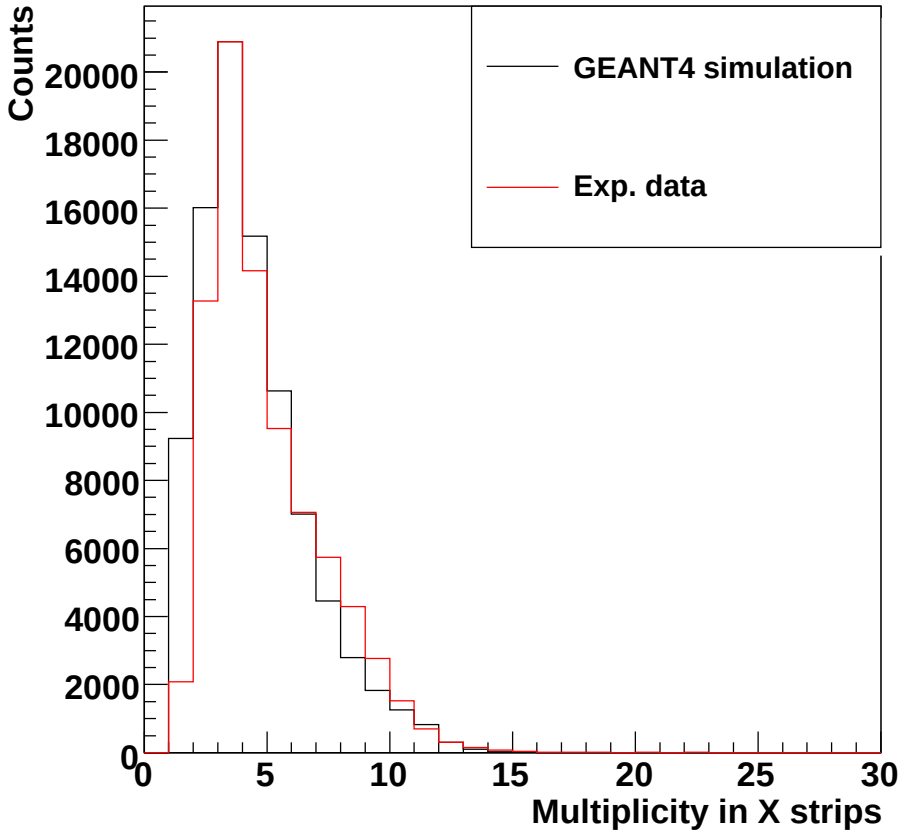

Figure 27. Comparison between the experimental distribution of the signal multiplicity in the X strips and the same quantity obtained by a complete (PCB included) GEANT4 simulation.

5 Measurements: XY-MicroMegas

In this report, and mainly in this section, the word “beam profile” often occurs and is used with a meaning slightly different from the original one. Normally the beam profile is defined as the spatial intensity profile of a beam at a particular plane transverse to the beam propagation path and can be visualized both through a bidimensional “countour line like” plot or a bidimensional plot seen in three dimension, with the third dimension being the neutron density. The former of the above mentioned representations is here referred exclusively as “beam image”, while with “beam profile” we designate not only the latter, but also its projection along one direction in the space.

The XYMG detector has been used in order to study the profile of the neutron beam at the n_TOF facility. Results from 4 measurement campaigns (2009, 2010, 2011 and 2012) are summarized in this report. For 2009 data the attention is focused on the influence of the second collimator on the beam profile and not on the beam profile itself.

Some general considerations and few details about the performance of the employed detector are intermixed with this main speech, to help a better comprehension of the experimental results. The beam profile is instead carefully studied for the 2010, 2011 and 2012 measurement campaigns, in order to extract the beam interception factor at the detector position (not at the sample position) relative to two targets of different diameters. The beam interception factor is vital for normalization purposes and is defined as the number of neutrons in the sample area, i.e. number of neutrons hitting the area covered by the sample, divided by the number of neutrons in the full area, i.e. by the number of neutrons in the whole beam. Table 1 summarizes the studies put in evidence in this report.

Table 1. Summary of the information contained in the report for 4 measurement campaigns.

Year	**Beam Time [protons]**	**Deposit thickness**	**Flight path [m]**	**Study**
2009	44.81184e+16	24 nm and 2μm	183.75	Influence of the 2^{nd} collimator on the beam profile tested
2010	93.973285e+16	2μm	183.75	Study of the beam image & profile + Determination of the beam interception factor
2011	N.D.	2μm	183.75	Study of the beam image & profile + Determination of the beam interception factor
2012	26.0463e+16	2μm	183.75	Study of the beam image & profile + Determination of the beam interception factor

All the beam images present in the report are oriented as Fig. 18. The“horizontal” and “vertical” EAR positions respectively coincides with X’ and Y’ or, in other words, with the floor and one lateral wall of the experimental area (EAR). The (X’,Y’) = (0,0) couple of coordinates mark the geometrical center of the detector.

The same conventions are used for all pictures showing the beam profile.

The lowest neutron energy delivered by the n_TOF beam is above the thermic point, therefore wherever a lower value is used, 0.03 eV should be read at its place. The habit of defining a neutron energy bin between 0.01 eV and 0.1 eV in fact only corresponds to the necessity of making to understand that analysis was performed by grouping data in 1 bin per decade.

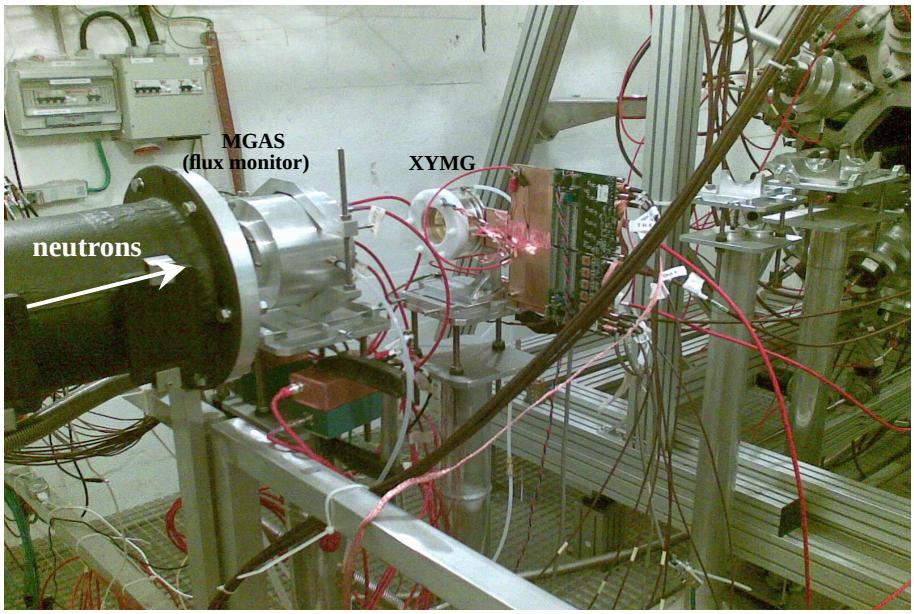

Figure 28. View of the EAR-1. The configuration shown is "XYMG close to silicon monitors".

5.1 2009

The "XY-micromegas" detector had already been used in the past at the n_TOF facility. Nonetheless in 2009 two neutron/charged particle converter thicknesses were tested (24 nm and 2 μm) as well as two positions (close to the silicon monitors and close to the sample exchanger). Here we report only measurements with the 24 nm thick ^{10}B deposit, to show the reason why in the following years the 2 μm thick one was preferred.

Fig. 28 is a photography of the experimental area. Neutrons come from the left and meet first a flux monitor. Being microbulk-type, this detector does not perturbate the incident neutron flux (see §4.4.2), and the XYMG can be positioned behind it without problems. The last detector encountered by the neutrons in the photography is the total absorber calorimeter. When the XYMG is in the beam, whatever detector positioned behind it is not used, since bulks strongly perturbate the incident neutron flux. The configuration shown is Fig. 28, characterized by a flight path (distance between the spallation target and the detector) L = 18374.0 cm, is known as "XYMG close to silicon monitors".

In order to be able to make some guess about the radial size of the neutron beam at the detector position, it is necessary to know a couple of details concerning the beam optics. The neutron pipe is divided in different sectors of decreasing diameters and is equipped with two collimators. The first, in iron and concrete, is 2 m long and simply reduces the beam radial size, while the second one, 2.5 m long, even shapes the neutron spectrum, thanks to the polyethylene hydrogen and ^{10}B content. Two versions of this collimator, differing in their radii, exist and are used one for fission and the other for capture measurements. For more details see [1]. Fig. 29 is a schematic view of the collimation system, considered as perfect (no misalignments), in capture configuration. For a flight path L = 18374.0 cm, which is translated into a distance between the end of the second collimator and the detector position equal to 5.89 m, considerations purely

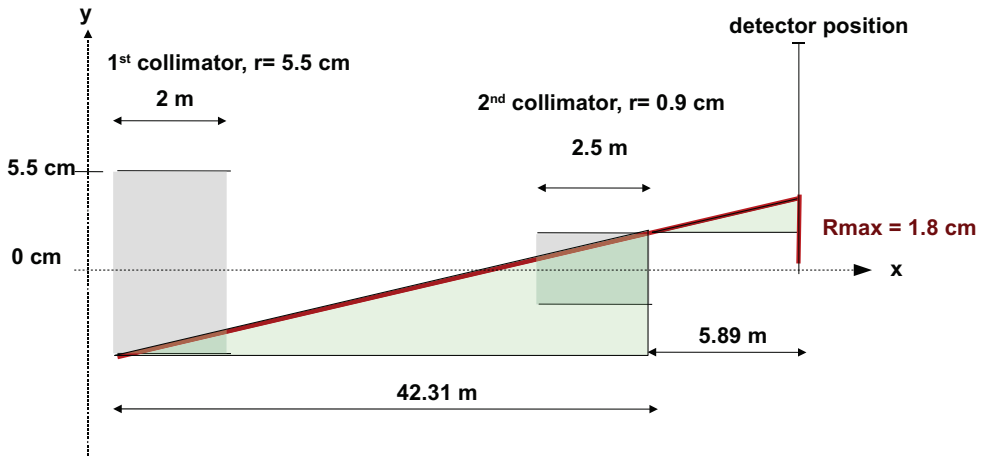

Figure 29. Schematic view of the collimation system (not in scale).

geometrical suggest that most neutrons hit the detector at y = 0, while no neutron should be seen outside a radius r = 1.8 cm from the center of the beam line at the detector position.

FLUKA simulations of the n_TOF spallation reaction have been performed in CERN. The generated neutrons have been transported along a flight path of L = 183.75 m by combining the FLUKA code (for neutron energies higher than 20 MeV) and the MCNPX code (for neutron energies lower than 20 MeV) and the beam image, has been obtained as a function of the incident neutron energy. The result, plotted in Fig. 30, shows that no neutron is found at a radial distance bigger than 1.8 cm from the center of the image, as expected.

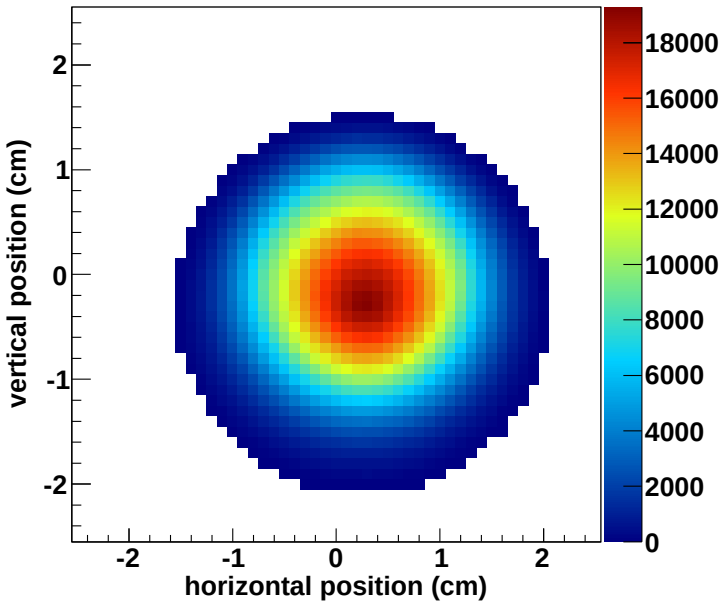

Figure 30. Beam image for a flight path L = 183.75 m. All neutron energies are considered.

5.1.1 1^{st} - 4^{th} July 2009

The first beam image obtained in 2009 is plotted in Fig. 31. The details of the measurement are reported in Tab 2. A multiplicity smaller than 8 was required for the calculation of the center of charge. The conditions imposed on the experimental data to extract the beam image change from time to time, since during the years the applied voltages were changed.

Table 2. Details of the measurement performed in the period 1^{st} - 4^{th} July 2009.

Configuration	XYMG close to SILI (assumed 183.75 m)
Runs	9072, 9074, 9075, 9076, 9077, 9078
Protons	1.722e+17
Converter thickness	24 nm
Mesh Voltage	330 V
Drift Voltage	480 V

The first characteristic of the beam image plotted in Fig. 31 catching our attention is its extension. The whole detector image is visible, at the extent that it is even possible to identify the missing angle (right side) outside the bulk ring. The other 3 angles are instead

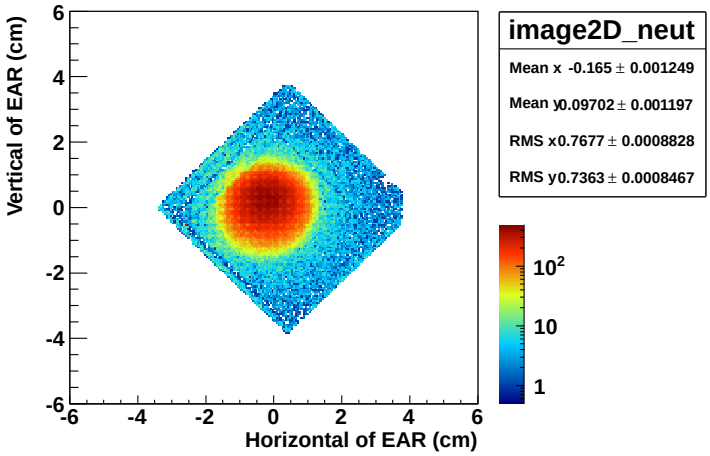

Figure 31. Beam image (μMegas detector seen in the reference system of the EAR.).

visible because 10 X and 10 Y strips are not employed. Compare Fig. 31 with Fig. 32 and Fig. 7 for a visual explanation. The experimentally obtained beam image put therefore in evidence that the whole bulk, and not only a spot of radius 1.8 cm, is detecting charged particles, thought of course only the portion of the bulk covered by the readout can be read and translated into an image.

On the other hand, since the neutron beam diameter at the detector position inferred from previous calculations measures only 3.6 cm, we were not expecting to see the whole part of the detector covered by the readout. Such discrepancy in the simulated and experimental beam image is due to two factors. The first consists in the fact that the procedure to infer the radial extension of the space covered by the neutrons at the detector position according to geometrical considerations, as well as the one to extract that according to the simulations performed in CERN by means of the FLUKA and MCNPX codes, are different from the data treatment experimentally performed. When a neutron strikes the ^{10}B converter, α particles and ^{7}Li are emitted. The emission angle depends on the kinematics of the reaction. Once the charged particle has been emitted, it is subjected to the electric field and the gravitational field. The latter, on such a small flight path as the drift to anode distance, and on such heavy nucleus is completely negligible with respect to the former, given a usual difference of potential between the drift electrode and the mesh of the order of 150 V. The kinetic energy acquired inside the electric field (around 70 eV for ^{4}He nuclei and 1.5 times such value for ^{7}Li) is in its turn negligible with respect to the kinetic energy with whom particles are emitted from the converter. Therefore also the trajectory of αs and ^{7}Li nuclei inside the detector is determined by the n(^{10}B,α)^{7}Li reaction. The larger the emission angle, the higher is the number of strips showing a signal due to the passage of the charged particle(s) and the less precise is the determination of the emission point based on the center of charge analysis. Thought, as explained in §4.4.1, this

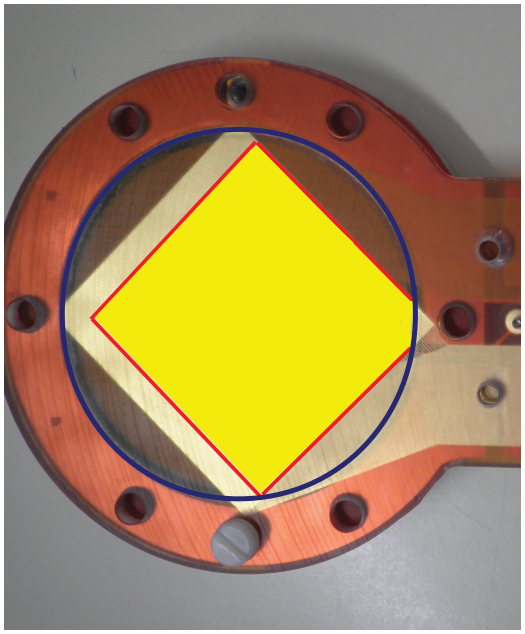

Figure 32. XYMG detector detail: the blue line signs the border of the circular bulk, while the red ones limit the area covered by the strips connected to the electronic chain acquiring and treating data. The yellow area resulting from the intersection of the bulk with the active part of the readout is the working section of the detector.

method is the best available, it introduces a halo on the border of the beam image as big as the multiplicity allowed in the analysis. For example, if the expected beam diameter is 1.8 cm, by allowing a multiplicity of 10 strips in the data analysis, a beam image with a radius of 10 strips *6 cm/(106 strips) = 0.56 cm larger than the expected one is obtained.

The second and dominant factor explaining the discrepancy in the dimension of the halo of Fig. 31 on one side and Fig. 30 and Fig. 29 on the other side, is the presence of the PCB in the experimental layout and its absence in the simulated and predicted ones. As explained in §4.4.2, the primary neutrons that do not interact neither with the boron converter nor with the gas molecules, can be backscattered by the PCB. The scattering angle depends on the kinematics of the reaction. The backscattered neutrons have therefore a certain probability to strike again the converter, and a non zero chance to do so in its peripheral region. The center of charge of a signal due to backscattered neutrons can therefore be localized in whatever part of the detector compatibly with the kinematics of the reaction.

Fig. 33 and Fig. 34 show the result of two GEANT4 simulations, where the incident primary particles are neutrons whose energy and position in space on a plane orthogonal to the beam direction are sampled respectively from the 2009 experimental n_TOF neutron flux and from the FLUKA simulations performed in CERN. The flux monitors, aluminum windows, ... are implemented in both geometries, with the difference that in one simulation also the PCB was considered, while in the other it was discarded. After

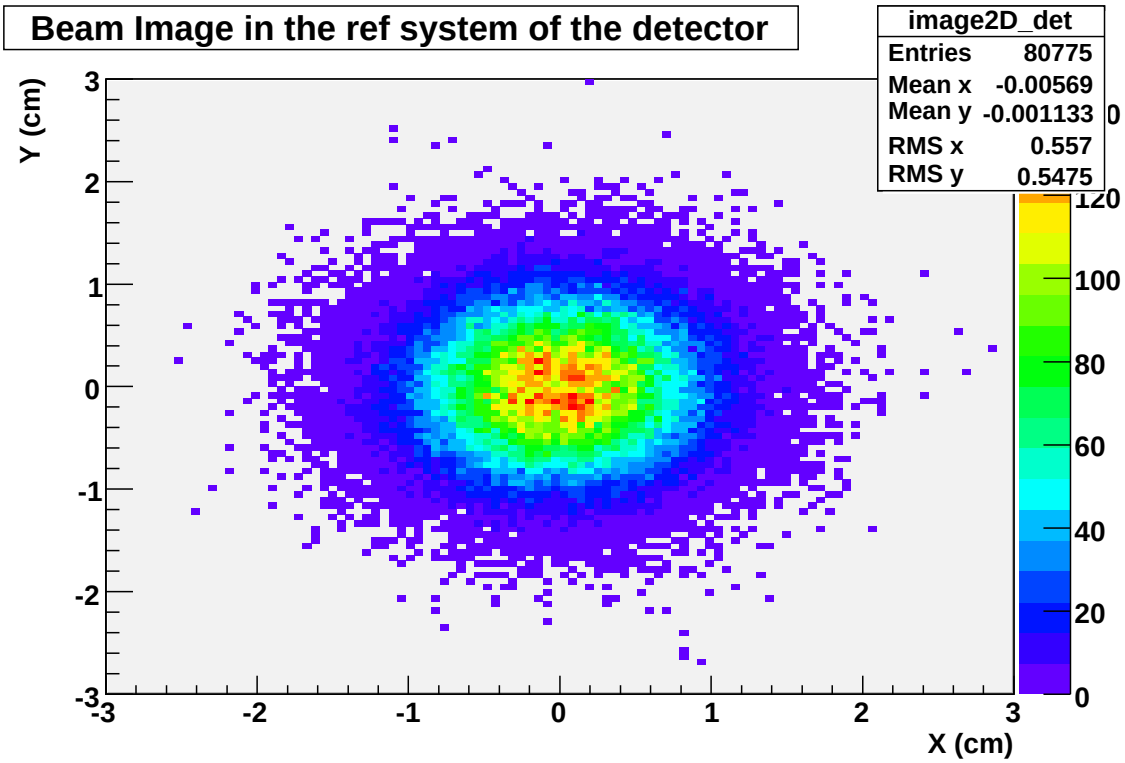

Figure 33. GEANT4 beam image when the PCB is not implemented in the geometry.

performing the analysis described in §4.4.3, the same data treatment as in the experimental case was carried on.

Another striking peculiarity of the beam image plotted in Fig. 31 is the presence of visible "lines". Going through the data analysis, if in the very first step we plot the amplitude of the signals picked up by each strip of one side of the detector for several events, the explanation to these lines is found. They correspond to strips providing always low amplitude signals. Fig. 35 and Fig. 36 well exemplifies the situation for a 2010 measurements (a 2010 measurement was preferred for the plot only because of higher statistics).Thought on one side the problematic strips affect the analysis of the beam interception factor, on the other one they result to be a fingerprint of our XYMG detector and can be used, year after year, to check the correctness of the reconstructed image.

For better visualizing the shape of the beam profile, a plot as in Fig. 37 is necessary. Its gaussian-like shape can be explained on the basis of the rules of the geometrical optics. Soon after the spallation target, the neutrons can be thought as a wavefront occupying the whole beam pipe diameter. Actually they occupy a small cylinder whose height is given by the difference in kinetic energy between the fastest and slowest neutrons. Therefore, up to the exit of the second collimator, we expect to see a beam profile shaped as a step function. When interacting with the edge of the second collimator, neutrons are either absorbed by ^{10}B or moderated by the hydrogen in the polyethylene, or by the carbon and

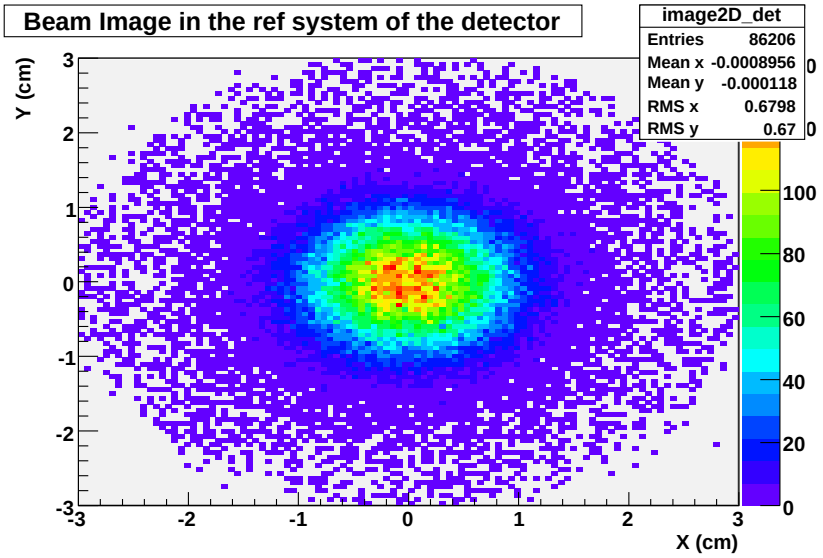

Figure 34. GEANT4 beam image when the PCB is implemented in the geometry.

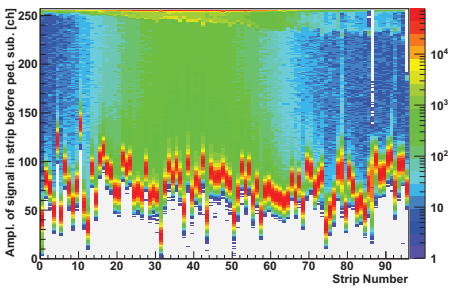

Figure 35. AMPLITUDE OF SIGNALS READ IN STRIPS CORRESPONDING TO THE X SIDE OF THE DETECTOR (SEE FIG. 18) BEFORE THE PEDESTAL SUBTRACTION.

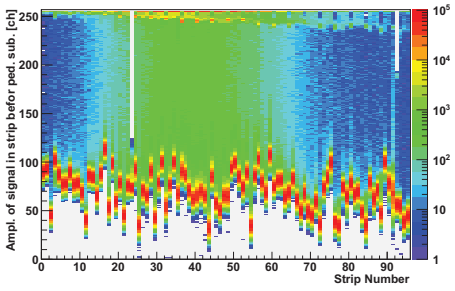

Figure 36. AMPLITUDE OF SIGNALS READ IN STRIPS CORRESPONDING TO THE Y SIDE OF THE DETECTOR (SEE FIG. 18) BEFORE THE PEDESTAL SUBTRACTION.

iron in the steel. The moderation process is a sequel of elastic scatterings, and we can think at this mechanism as neutrons striking the collimator and being reflected.

In reality the beam profile is not a Gaussian, and can not even be precisely described by a Gaussian distribution convoluted with a door function as instead expected. Several small factors affect the shape of the beam profile and hold it from resulting perfectly symmetric. An example of one of such factors, for low neutron energies, is represented by the gravitational effect, that influences the projection of the beam profile along the vertical direction parallel to the walls of the experimental area.

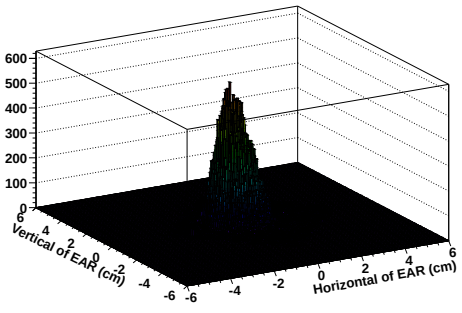

Figure 37. XYMG detector detail: the blue line signs the border of the circular bulk, while the red ones limit the area covered by the strips connected to the electronic chain acquiring and treating data. The yellow area resulting from the intersection of the bulk with the active part of the readout is the working section of the detector.

In any case, the bidimensional beam profile can be approximated and therefore fitted with the bivariate normal function given in 2

$$f(x,y) = \frac{A}{2\pi\sigma_x\sigma_y\sqrt{1-\rho^2}} \cdot e^{-}\left(\frac{\left(\frac{(x-x_0)^2}{\sigma_x^2}\right) + \left(\frac{(y-y_0)^2}{\sigma_y^2}\right) - 2\rho\frac{(x-x_0)\cdot(y-y_0)}{\sigma_x\sigma_y}}{2(1-\rho^2)}\right) \quad (2)$$

with ρ being the correlation between x and y. If the gaussian is simmetric, ρ = 0, and the 2 takes the form given in 3

$$f(x,y) = \frac{A}{2\pi\sigma_x\sigma_y} \cdot e^{-}\left(\frac{(x-x_0)^2}{2\sigma_x^2} + \frac{(y-y_0)}{2\sigma_y^2}\right) \quad (3)$$

If the ρ parameters is left free in the fit, and all neutron energies are considered, the result in table 3 is obtained for the measurement performed in the period 1^{st} - 4^{th} July 2009.

Table 3 shows that the ρ parameter is not compatible with zero, but by computing the covariance matrix associated to the fit parameters the correlation among such parameters can be calculated. Table 4 reports the correlation matrix for the performed fit and shows that there is anyhow only little correlation between x and y coordinates and no correlation (or, in another measurements, little correlation) between σ_x and σ_y.

Therefore it is possible fixing the ρ parameter to zero and fitting the beam profile with the simmetric bivariate normal distribution given in 3. Such function presents an interesting feature. If integrated along one dimension, it gives rise to a new gaussian characterized by the same mean and width of the original normal distribution. The operation of integrating the bivariate normal function along one direction is equivalent to perform its projection along the direction orthogonal to the previous one.

Table 3. Fit parameters extracted by fitting the beam profile with a bivariate normal distribution. The ρ parameter was left free.

Parameter Number	Parameter Name	Parameter Value	Parameter Uncertainty	% Uncertainty
0	Const	1.16655E+03	1.93889E+00	0.2
1	X_0	-2.00480E-01	1.13008E-03	0.6
2	σ_x	6.69874E-01	8.51754E-04	0.1
3	Y_0	1.06803E-01	1.08592E-03	1.0
4	σ_y	6.47007E-01	8.04229E-04	0.1
5	ρ	3.63890E-02	1.70190E-03	4.7

Table 4. Correlation matrix associated to the fit parameters of 3.

Parameter	Const	$\mathbf{X}_0$	σ_x	$\mathbf{Y}_0$	σ_y	ρ
Const	100	-0	2	0	2	0
$\mathbf{X}_0$	-0	100	-1	4	0	0
σ_x	2	-1	100	-0	0	3
$\mathbf{Y}_0$	0	4	-0	100	0	-0
σ_y	2	0	0	0	100	3
ρ	0	0	3	-0	3	100

Since unidimensional plots on a paper are easier to be read than bidimensional plots constrained on a page, the beam profile will be presented through its projections in the whole report. In the following pages the experimental beam profile obtained by selecting different neutron energy ranges is shown with its fit. The fit is performed by excluding the tails, since as previously seen, they are due to the presence of the PCB. The beam profile obtained by the simulations performed in CERN is also shown, as ideal situation (true beam profile) in absence of the PCB.

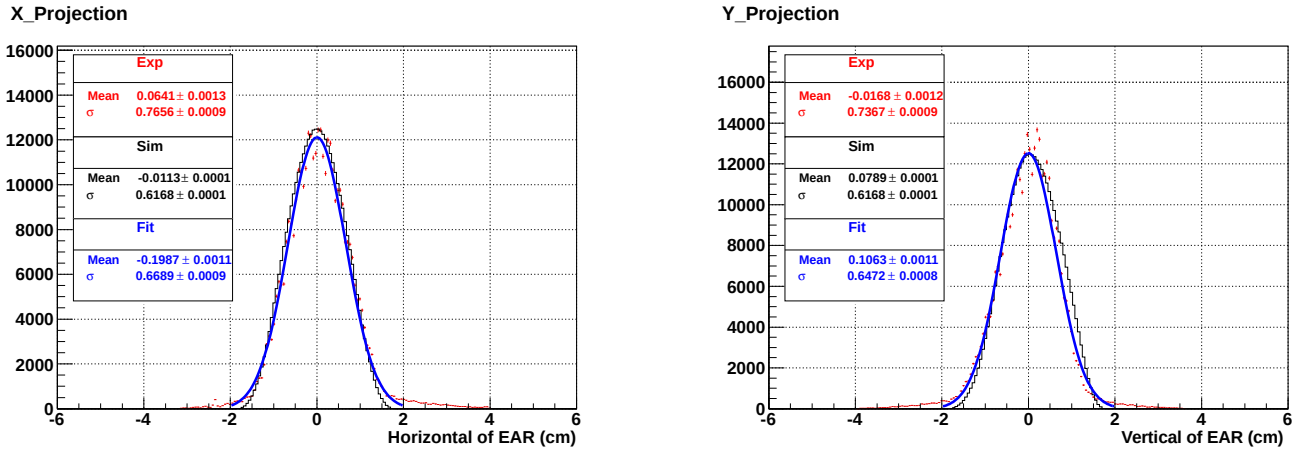

Figure 38. Beam profile obtained by considering all neutron energies.

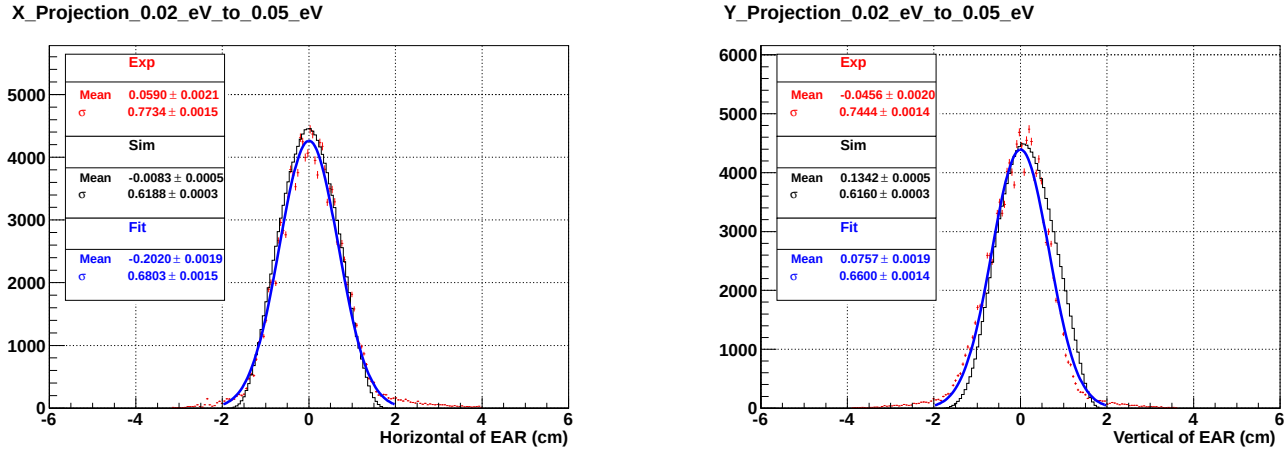

Figure 39. Beam profile in the energy range between 0.022 eV and 0.05 eV.

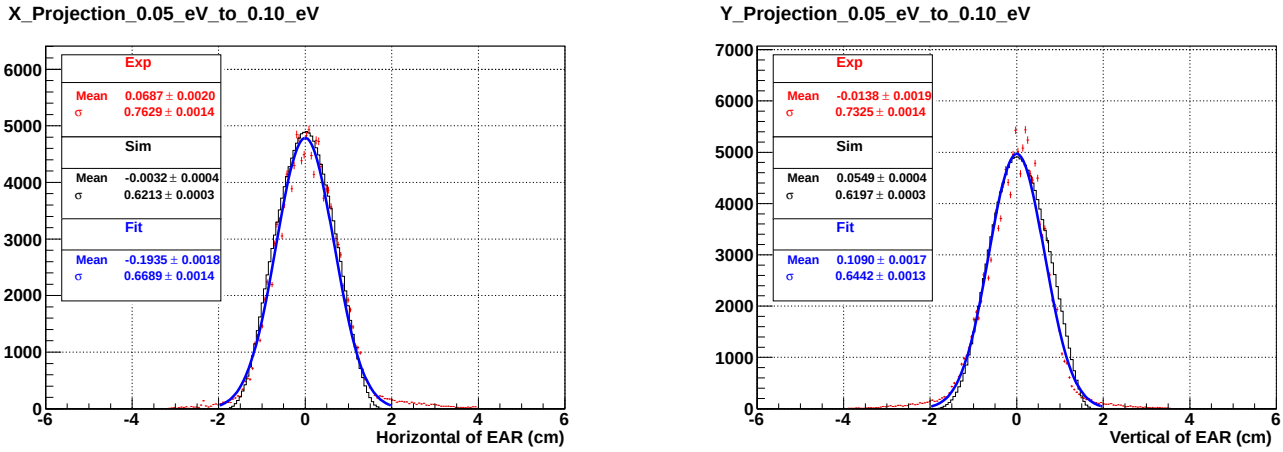

Figure 40. Beam profile in the energy range between 0.05 eV and 0.1 eV.

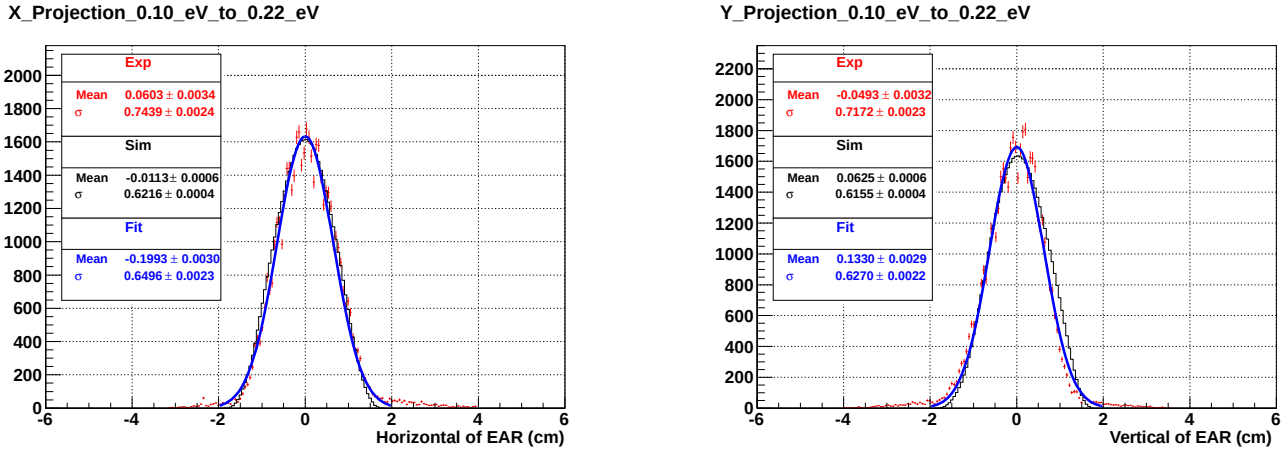

Figure 41. Beam profile in the energy range between 0.1 eV and 0.22 eV.

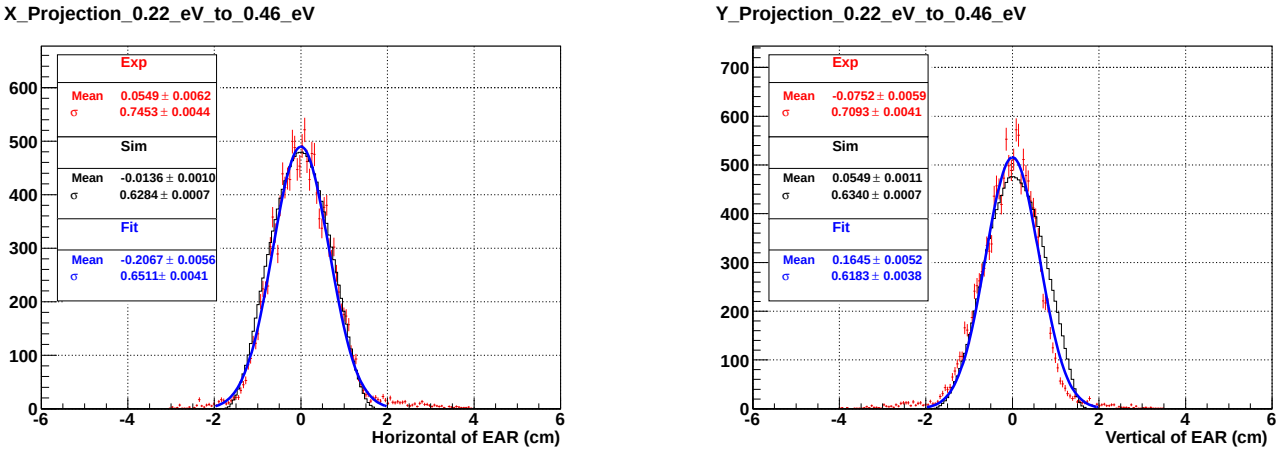

Figure 42. Beam profile in the energy range between 0.22 eV and 0.46 eV.

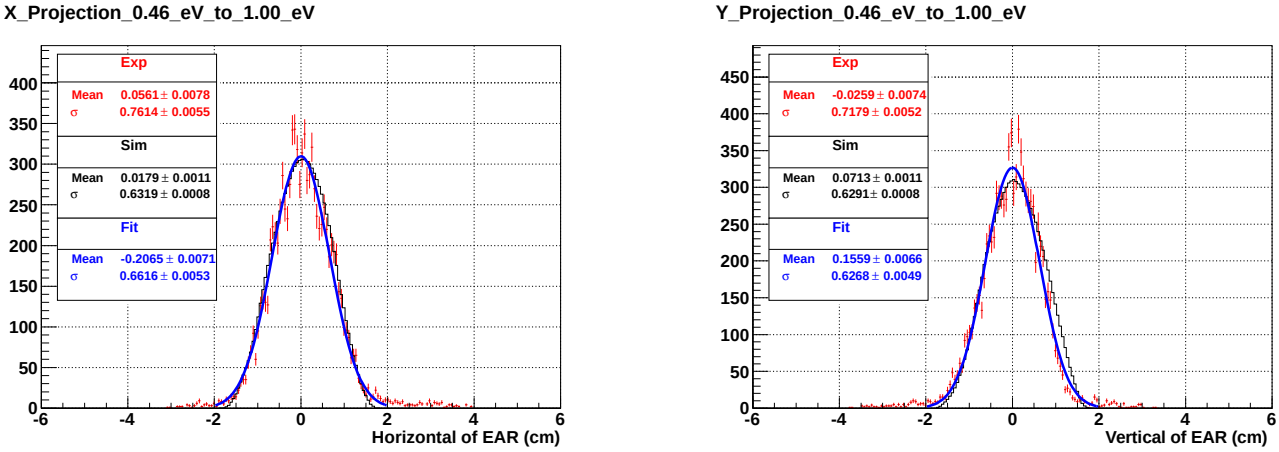

Figure 43. Beam profile in the energy range between 0.46 eV and 1 eV.

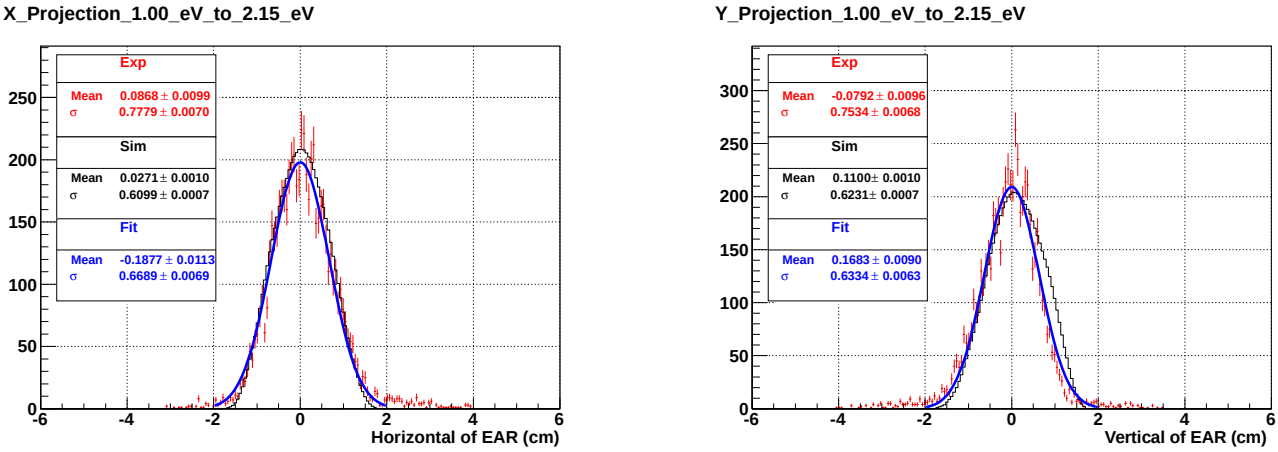

Figure 44. Beam profile in the energy range between 1 eV and 2.15 eV.

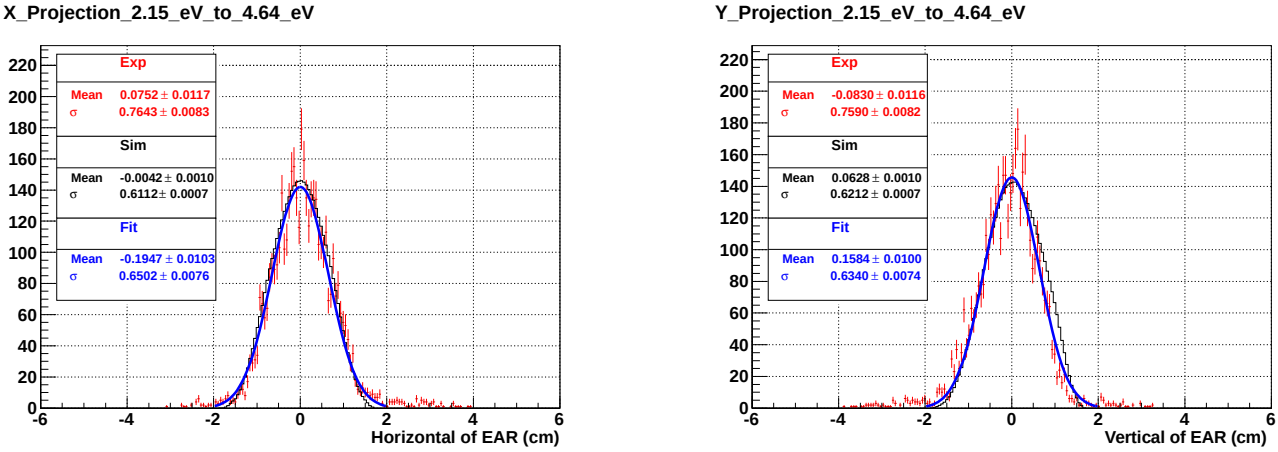

Figure 45. Beam profile in the energy range between 2.15 eV and 4.64 eV.

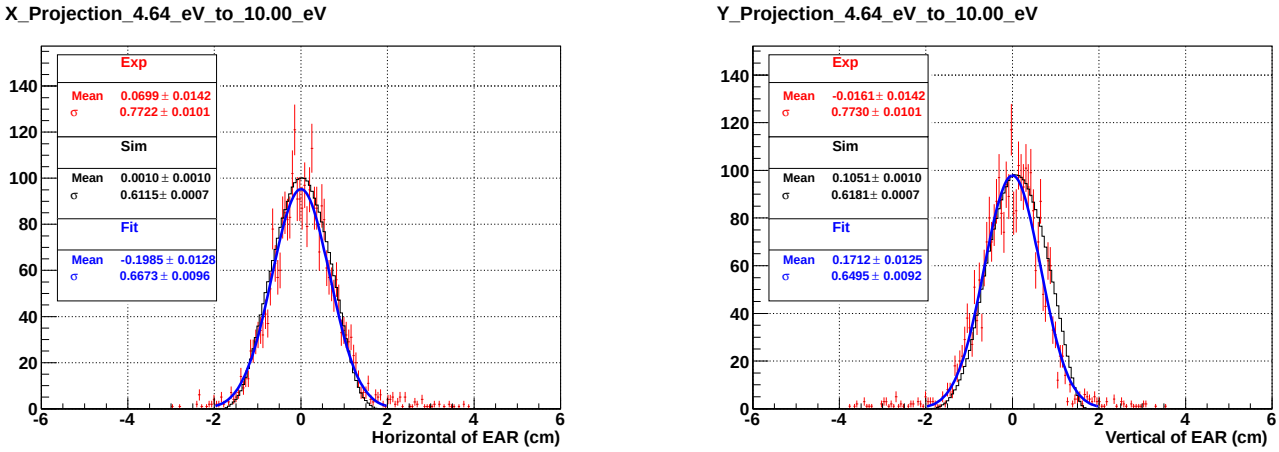

Figure 46. Beam profile in the energy range between 4.64 eV and 10 eV.

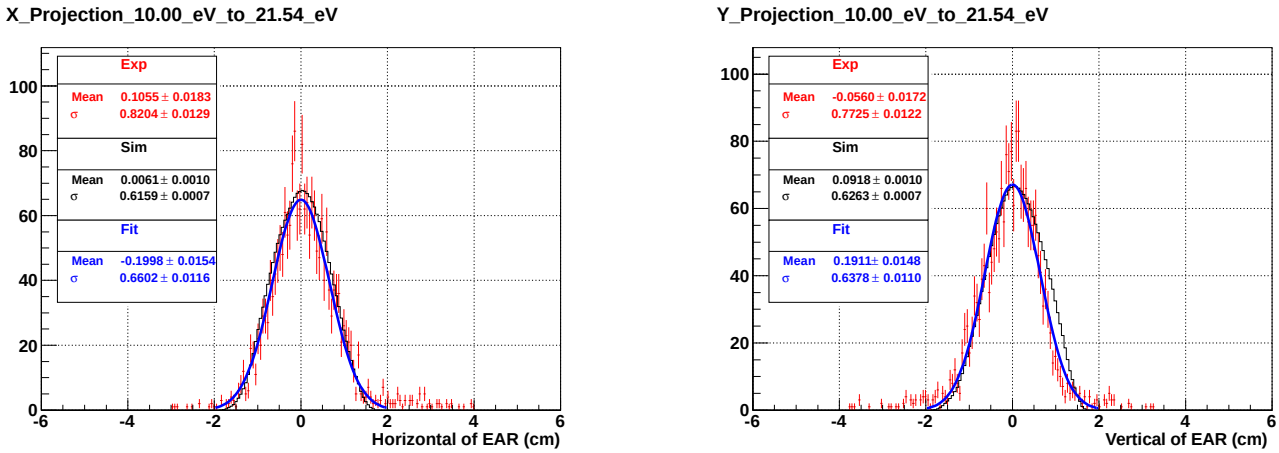

Figure 47. Beam profile in the energy range between 10 eV and 21.54 eV.

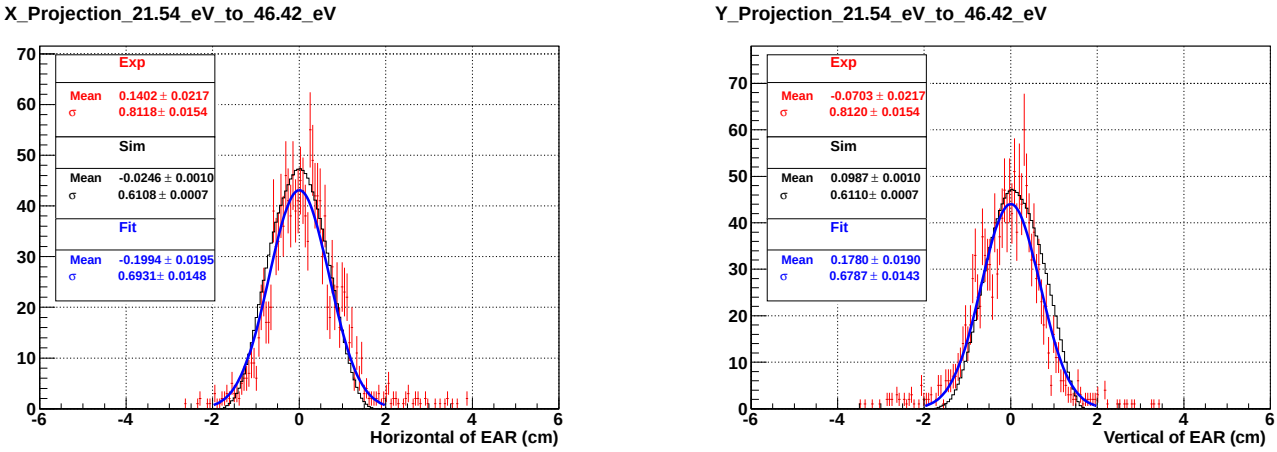

Figure 48. Beam profile in the energy range between 21.54 eV and 46.42 eV.

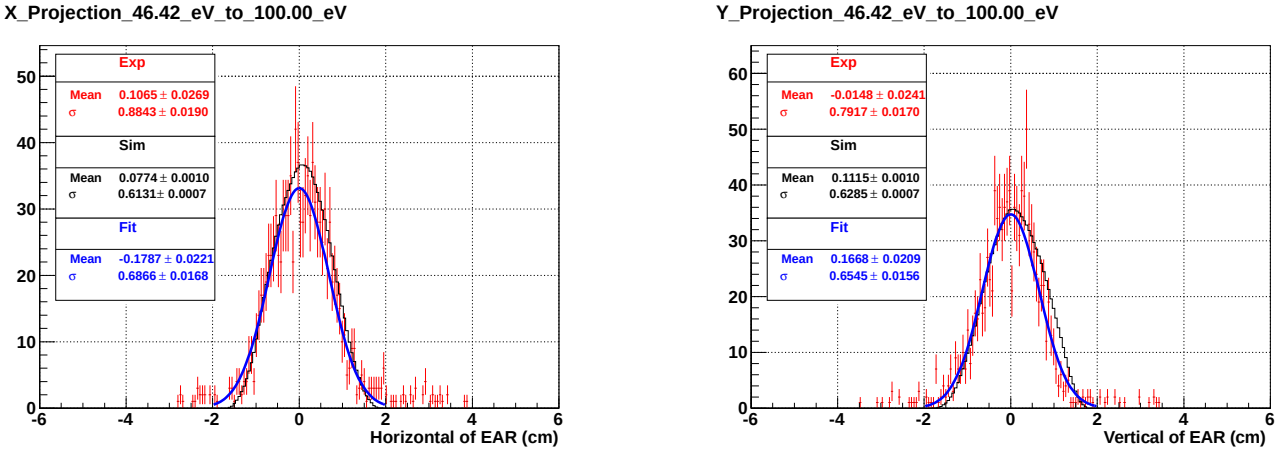

Figure 49. Beam profile in the energy range between 46.42 eV and 100 eV.

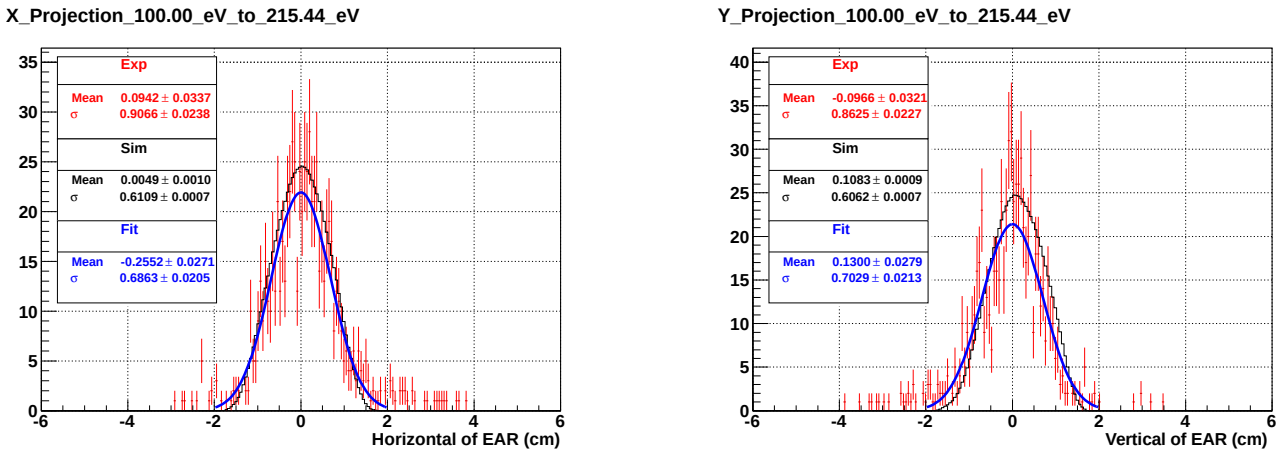

Figure 50. Beam profile in the energy range between 100 eV and 215.44 eV.

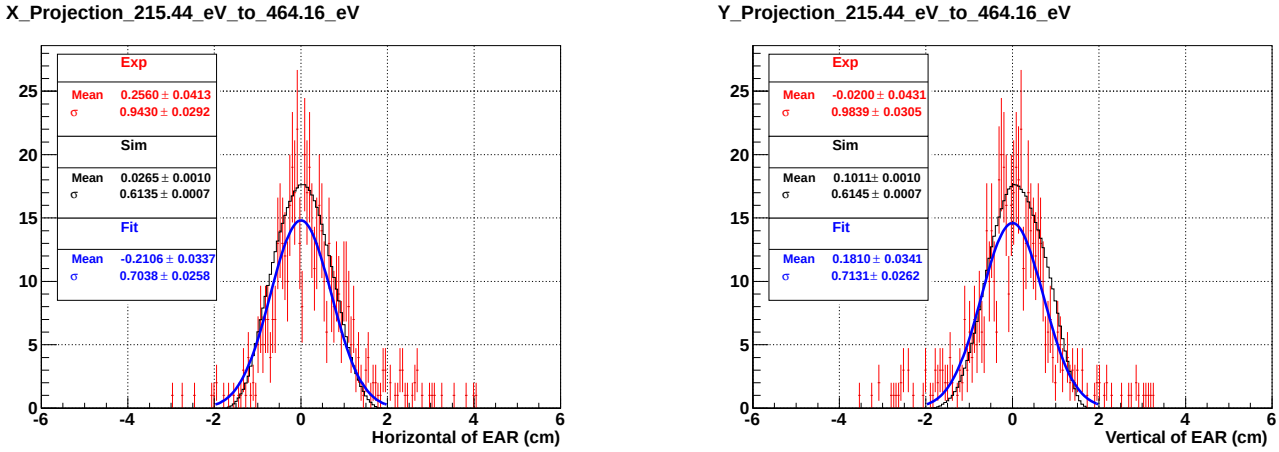

Figure 51. Beam profile in the energy range between 215.44 eV and 464.16 eV.

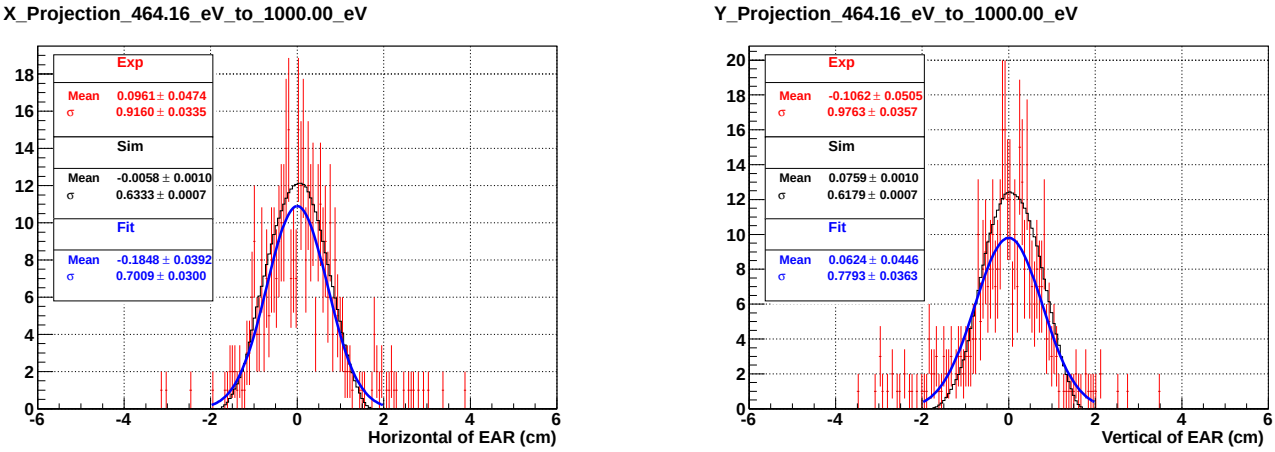

Figure 52. Beam profile in the energy range between 464.16 eV and 1 keV.

For neutron energies exceeding 1 keV no beam profile is reported because of too low statistics. Even increasing the time duration of the measurements, only little improvement would be obtained. This lack of statistics at high neutron energies is in fact due to the combination of two factors: a really thin neutron/charged particle converter thickness and the trend of $^{10}B(n,\alpha)^{7}Li$ cross section (decreasing for increasing neutron kinetic energy). Fig. 39 shows that the beam profile results “bent” and is characterized by a rugged top. This last feature is a consequence of the operation of integration.

5.1.2 11^{th} - 13^{th} July 2009

The detector was moved and a new image (see Fig. 53) was acquired.

Table 5. Details of the measurement performed in the period 11^{th} - 13^{th} July 2009.

Configuration	XYMG close to SILI
Runs	9119, 9120, 9121, 9122
Protons	8.8e+16
Converter thickness	24 nm
Mesh Voltage	330 V
Drift Voltage	480 V

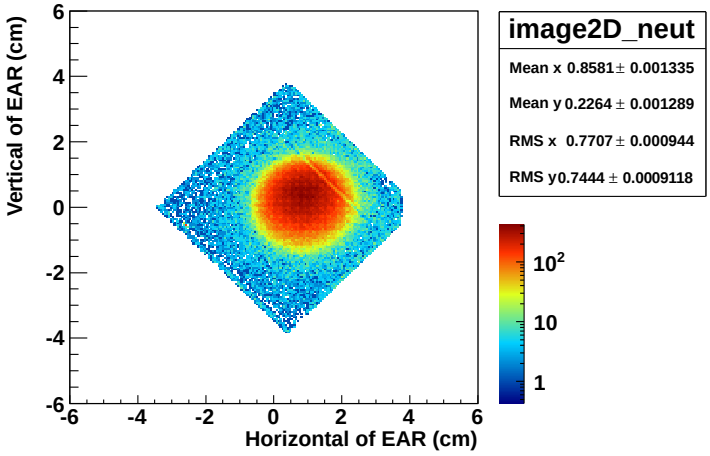

Figure 53. Beam image (μMegas detector seen in the reference system of the EAR.).

Apart from a different center of the image, nothing changed with respect to the previous measurement.

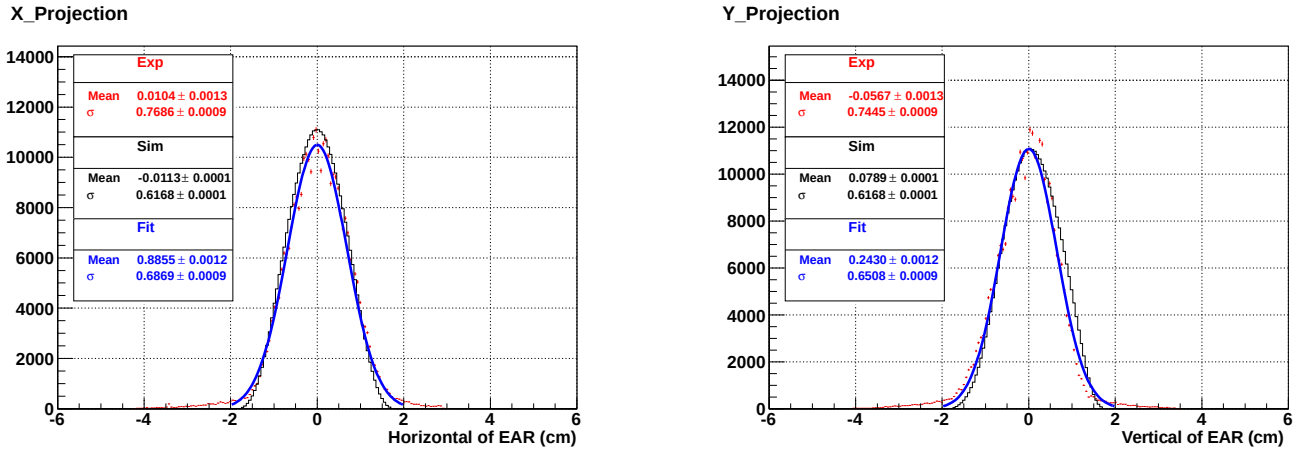

Figure 54. Beam profile obtained by considering all neutron energies.

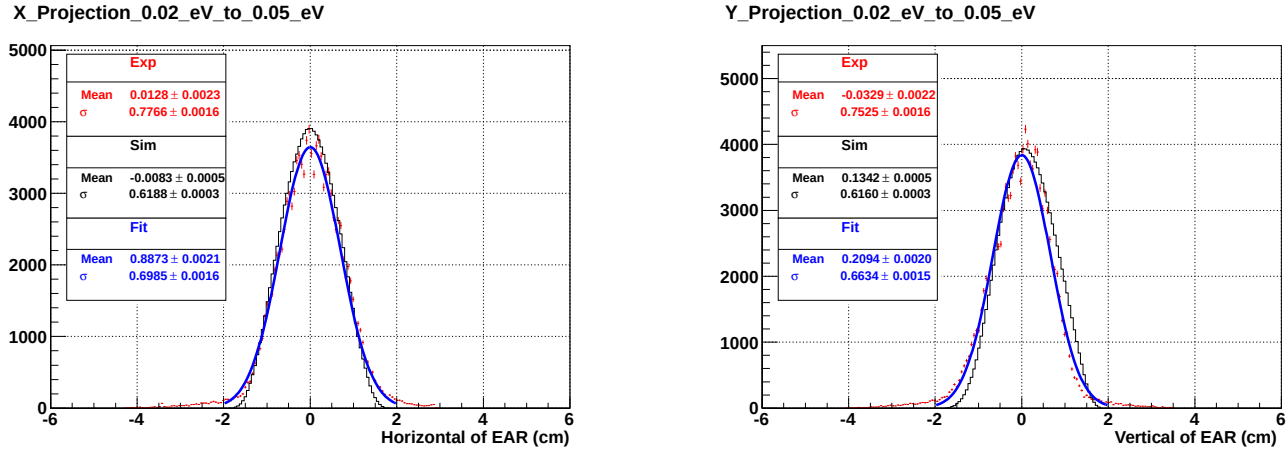

Figure 55. Beam profile in the energy range between 0.022 eV and 0.05 eV.

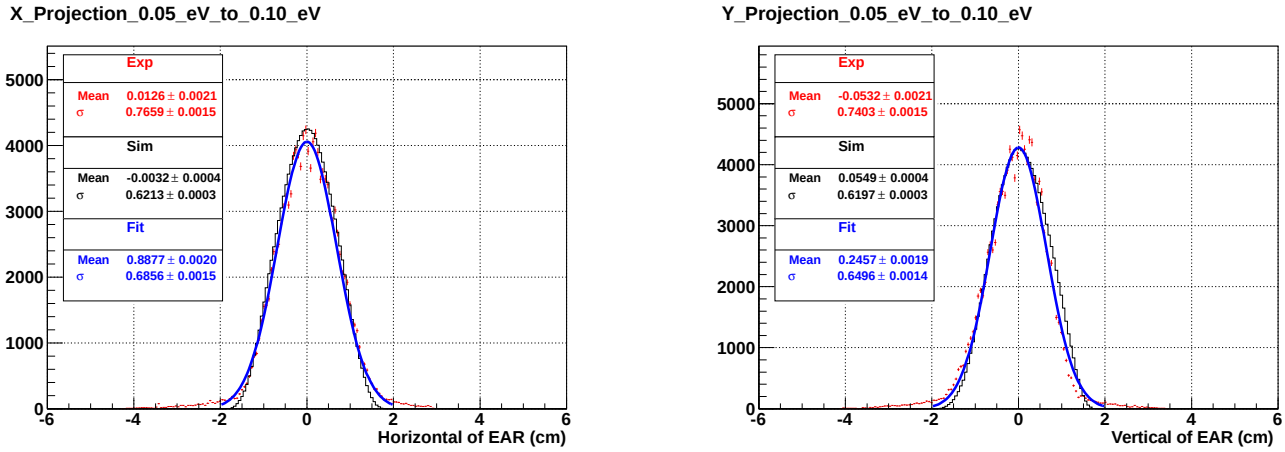

Figure 56. Beam profile in the energy range between 0.05 eV and 0.1 eV.

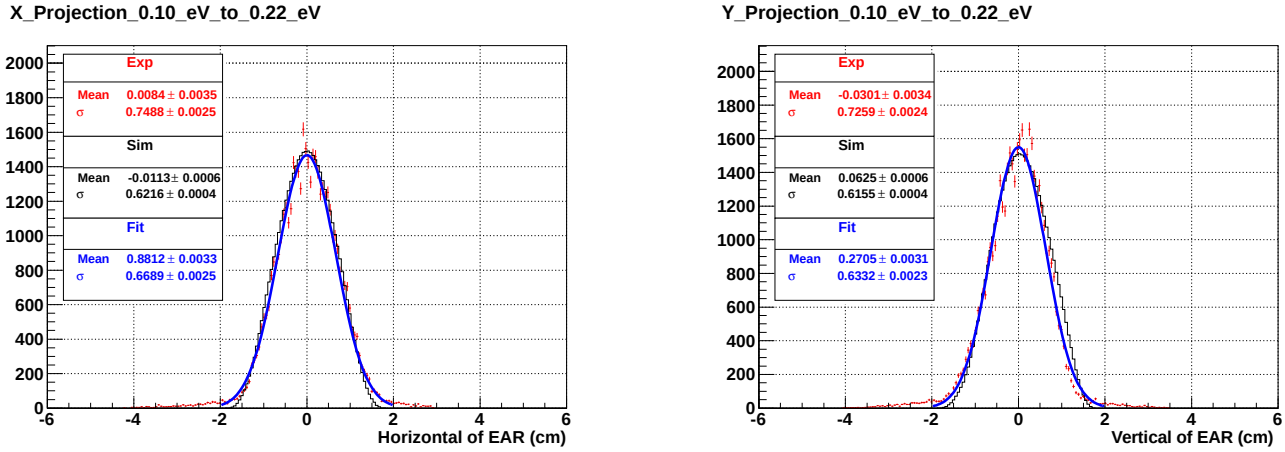

Figure 57. Beam profile in the energy range between 0.1 eV and 0.22 eV.

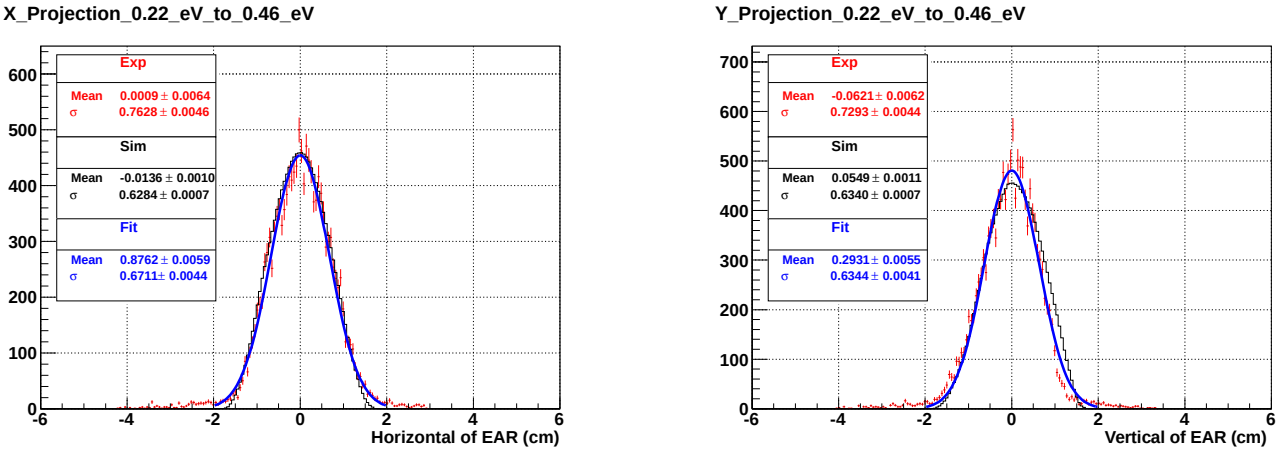

Figure 58. Beam profile in the energy range between 0.22 eV and 0.46 eV.

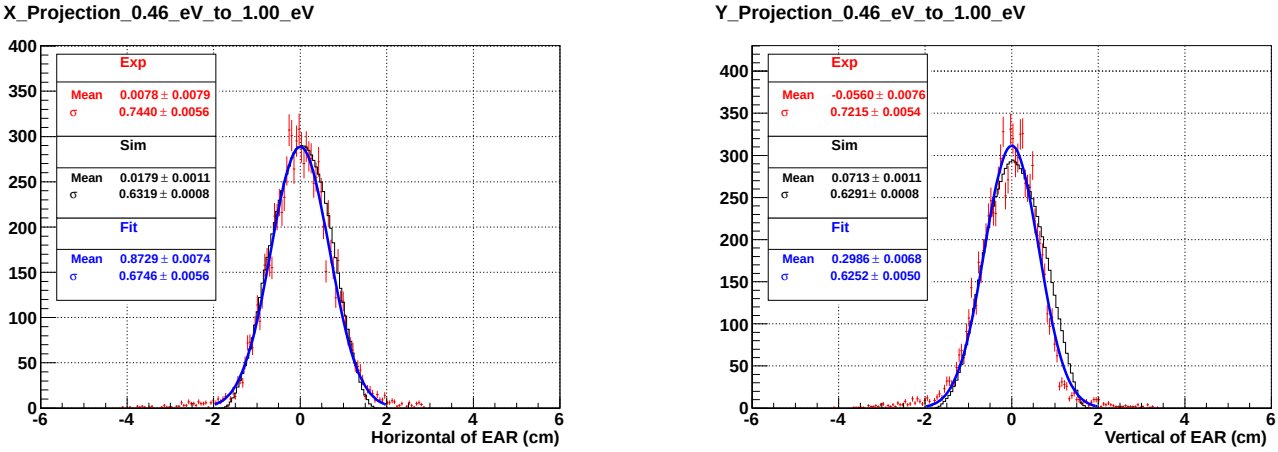

Figure 59. Beam profile in the energy range between 0.46 eV and 1 eV.

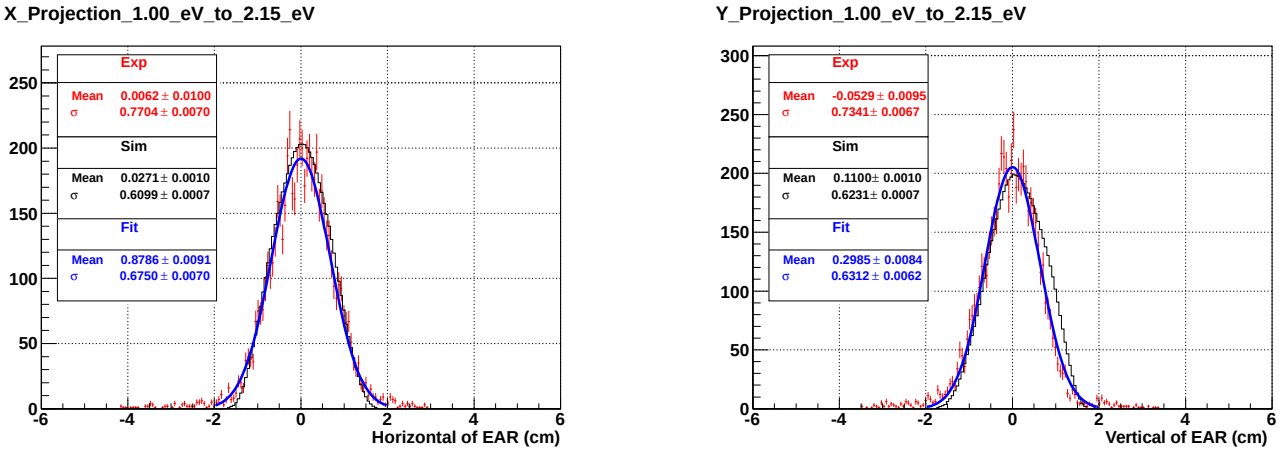

Figure 60. Beam profile in the energy range between 1 eV and 2.15 eV.

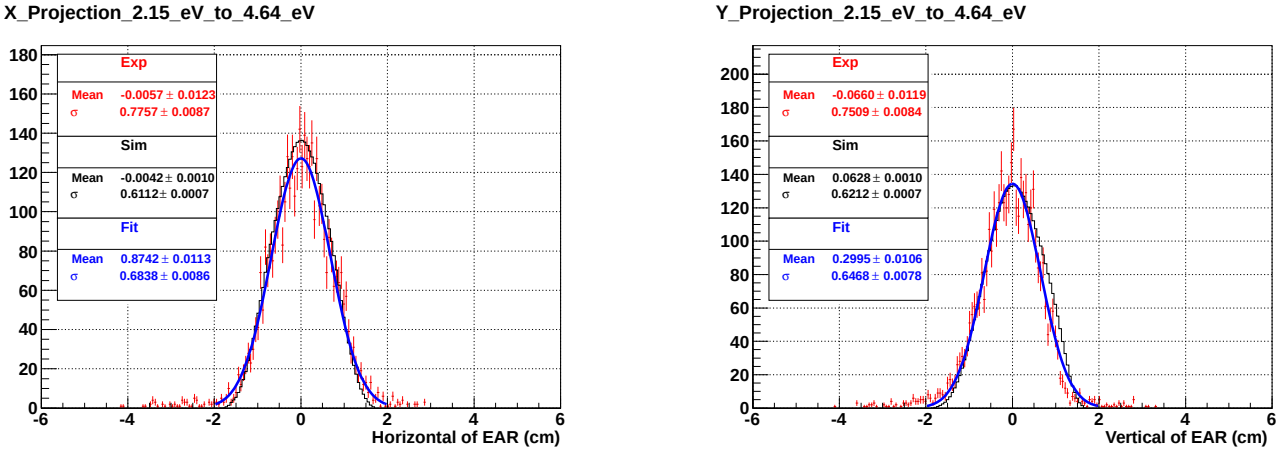

Figure 61. Beam profile in the energy range between 2.15 eV and 4.64 eV.

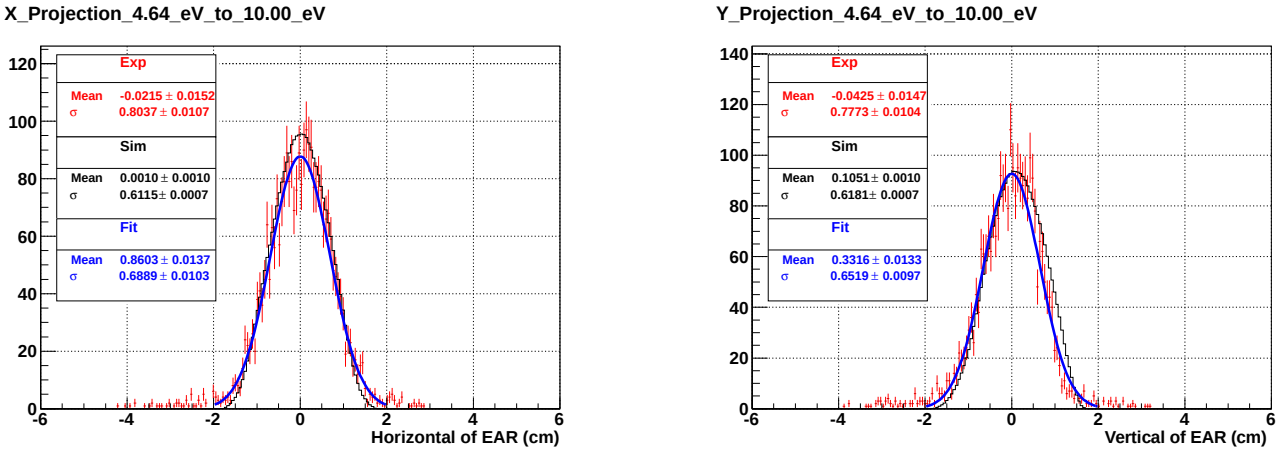

Figure 62. Beam profile in the energy range between 4.64 eV and 10 eV.

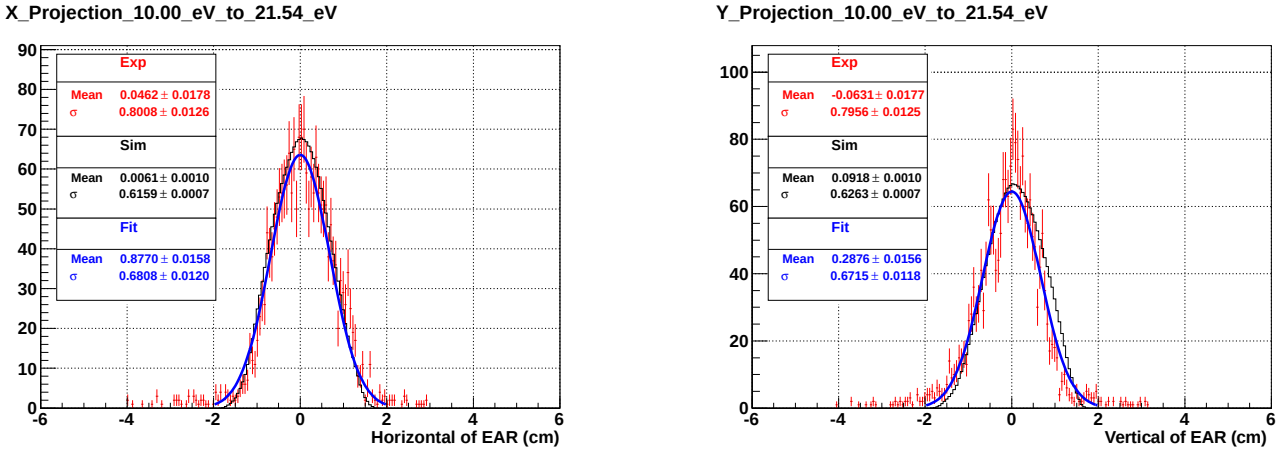

Figure 63. Beam profile in the energy range between 10 eV and 21.54 eV.

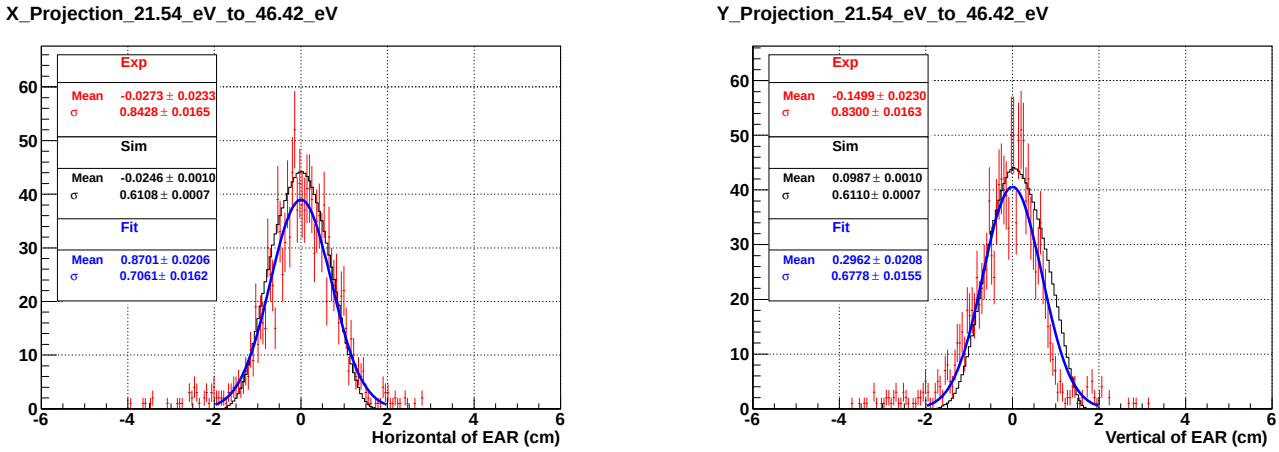

Figure 64. Beam profile in the energy range between 21.54 eV and 46.42 eV.

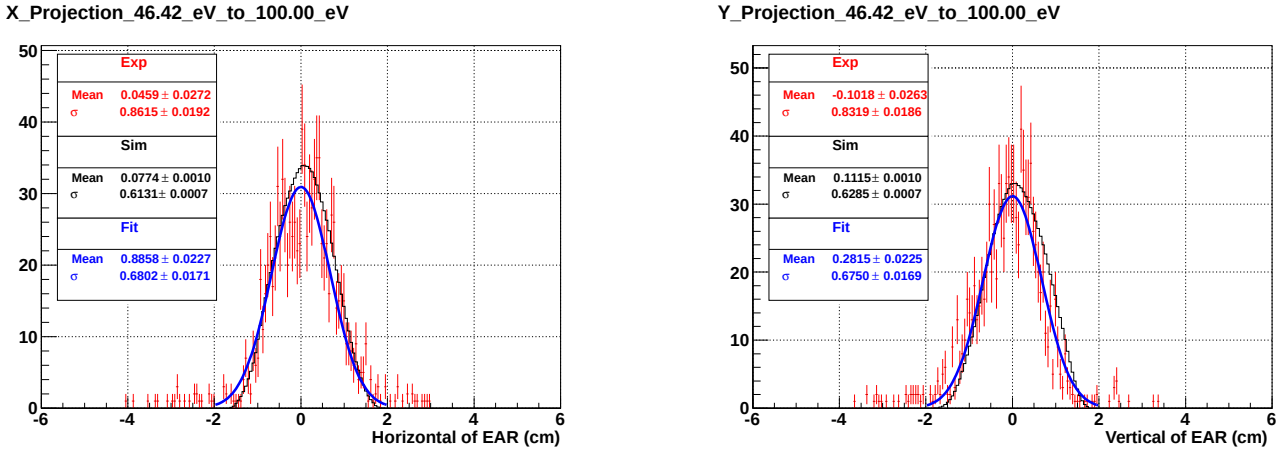

Figure 65. Beam profile in the energy range between 46.42 eV and 100 eV.

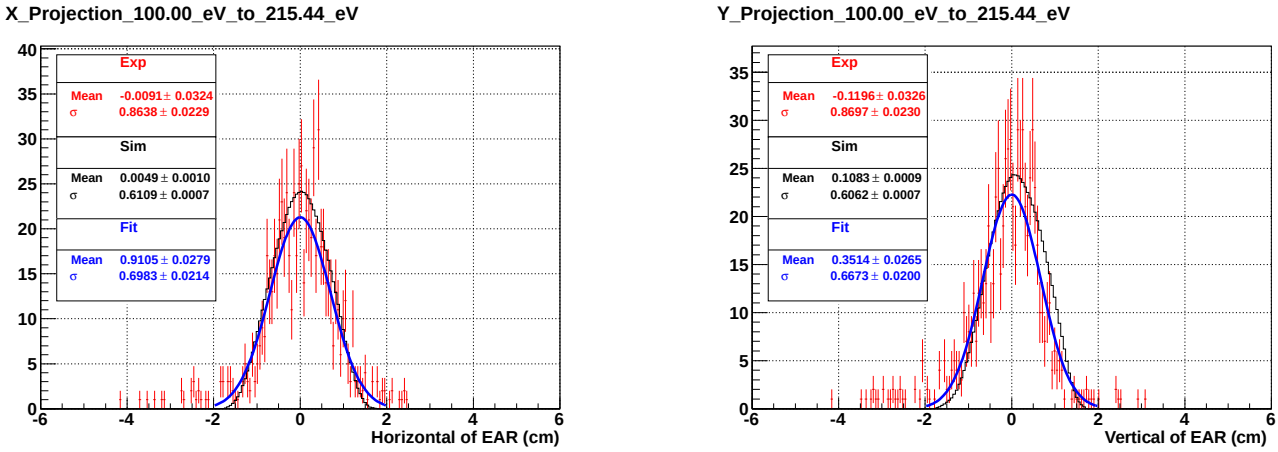

Figure 66. Beam profile in the energy range between 100 eV and 215.44 eV.

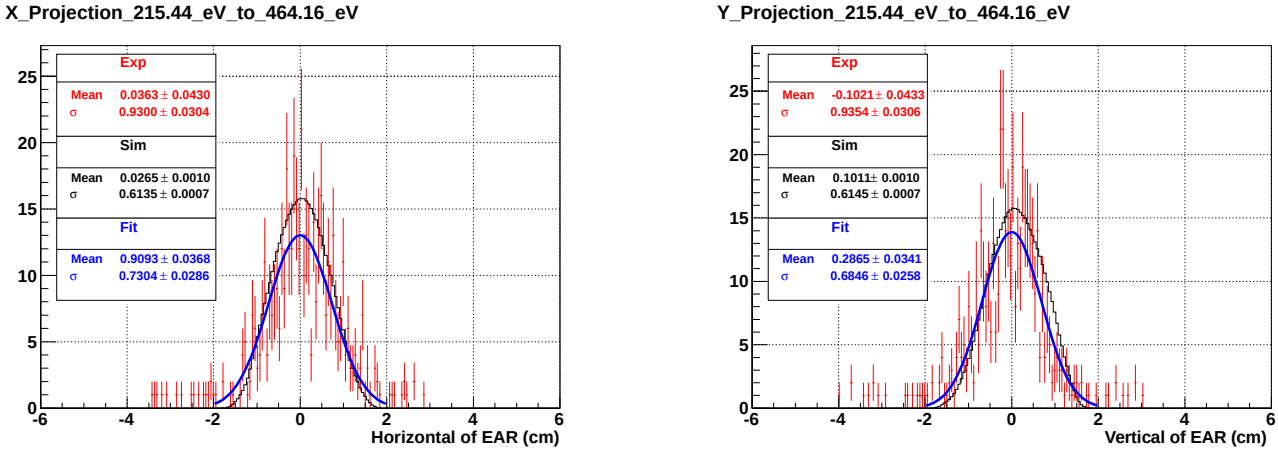

Figure 67. Beam profile in the energy range between 215.44 eV and 464.16 eV.

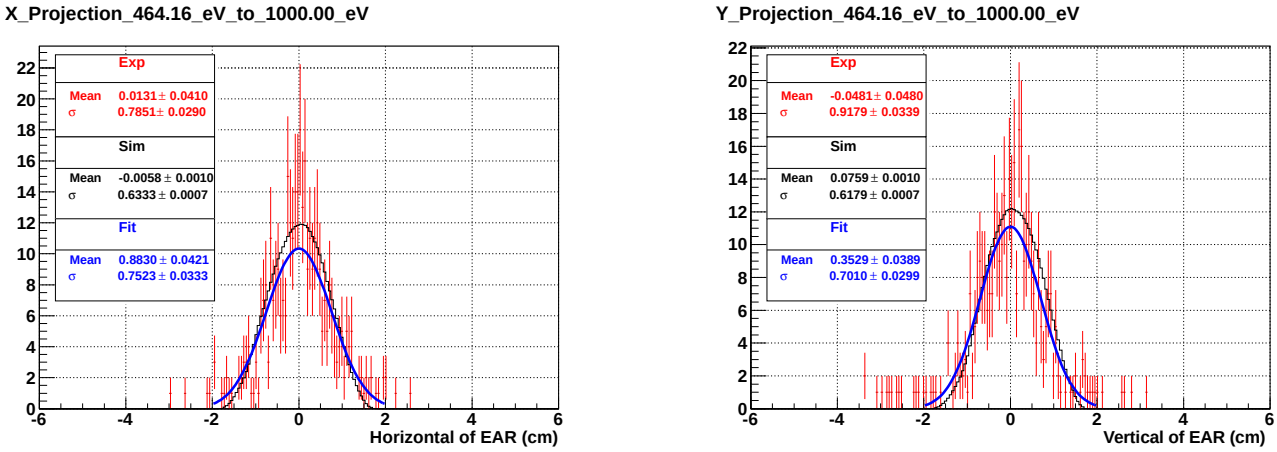

Figure 68. Beam profile in the energy range between 464.16 eV and 1 keV.

5.1.3 16^{th} November 2009

Table 6. Details of the measurement performed the 16^{th} November 2009.

Configuration	No info (it should therefore be: XYMG close to SILI)
Runs	9831, 9832, 9833, 9834, 9835, 9836, 9837, 9838 9839, 9840, 9941, 9842, 9843
Protons	5.16884e+16
Converter thickness	24 nm
Mesh Voltage	No info available
Drift Voltage	No info available

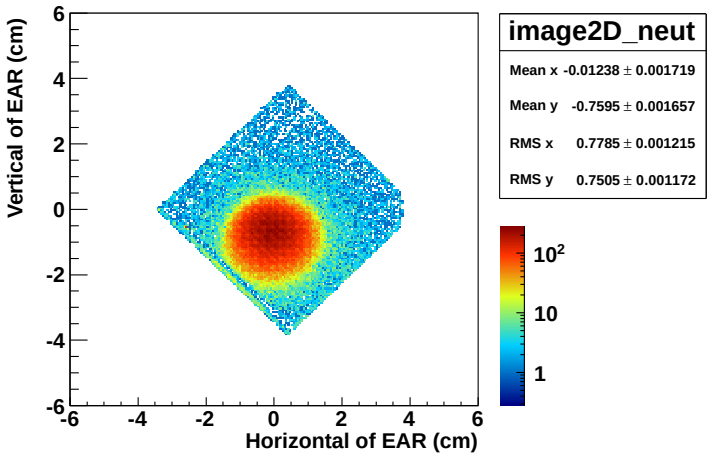

Figure 69. Beam image (μMegas detector seen in the reference system of the EAR.).

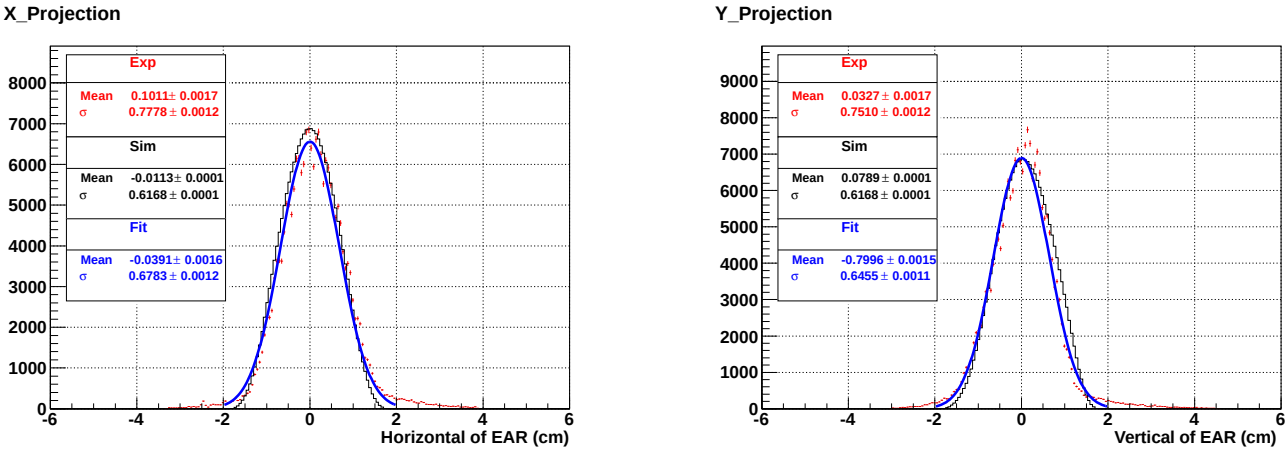

Figure 70. Beam profile obtained by considering all neutron energies.

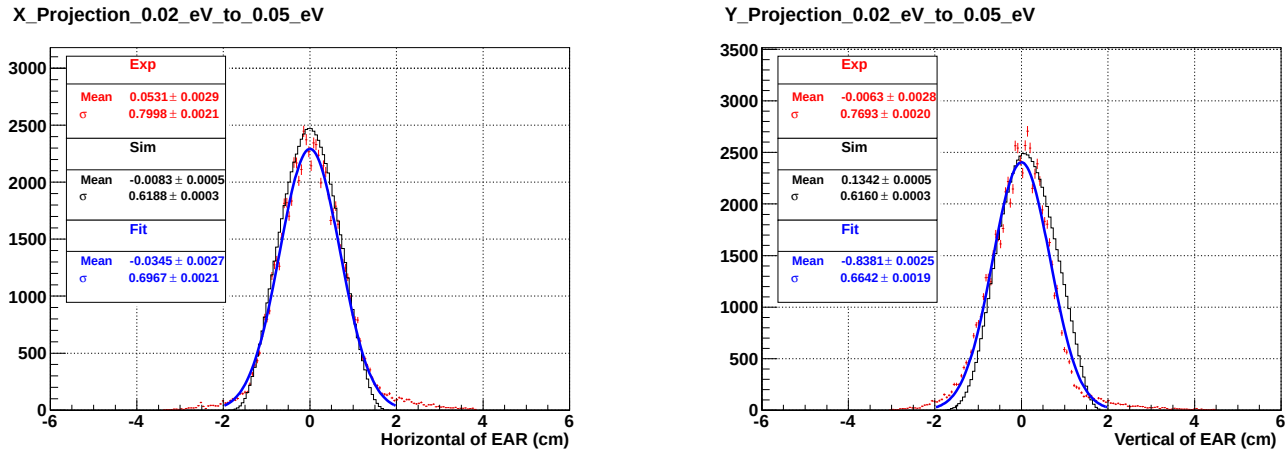

Figure 71. Beam profile in the energy range between 0.022 eV and 0.05 eV.

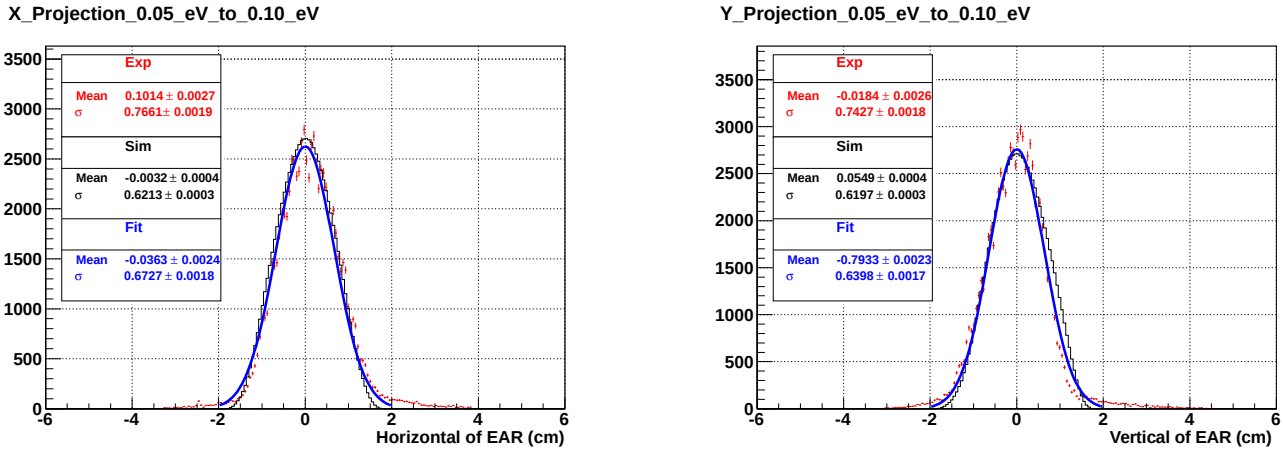

Figure 72. Beam profile in the energy range between 0.05 eV and 0.1 eV.

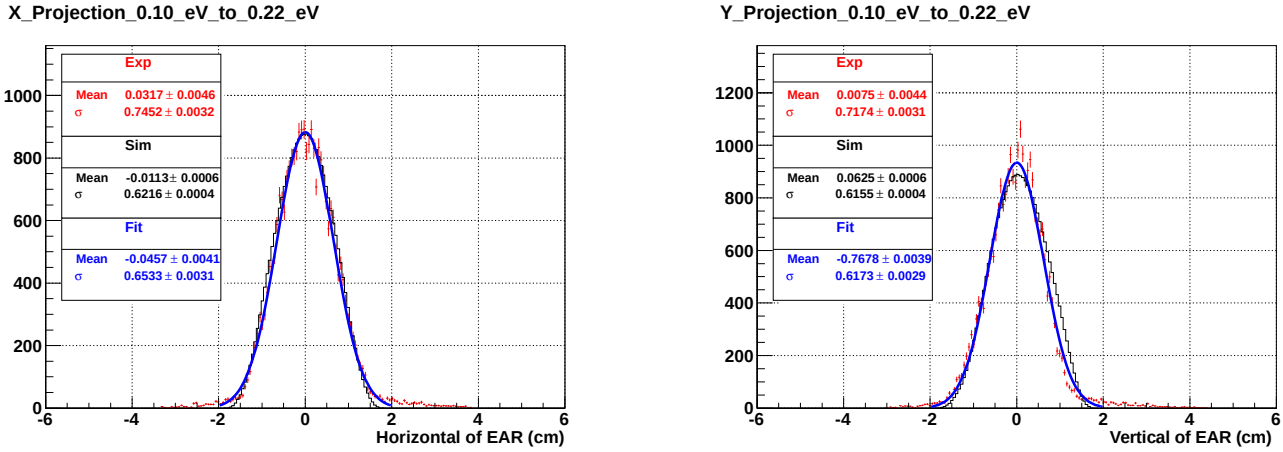

Figure 73. Beam profile in the energy range between 0.1 eV and 0.22 eV.

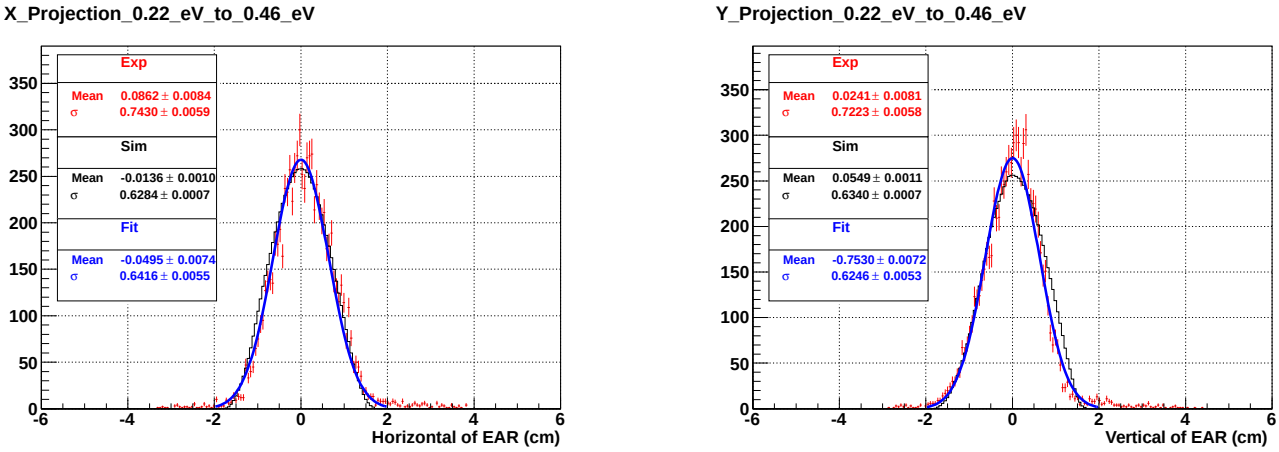

Figure 74. Beam profile in the energy range between 0.22 eV and 0.46 eV.

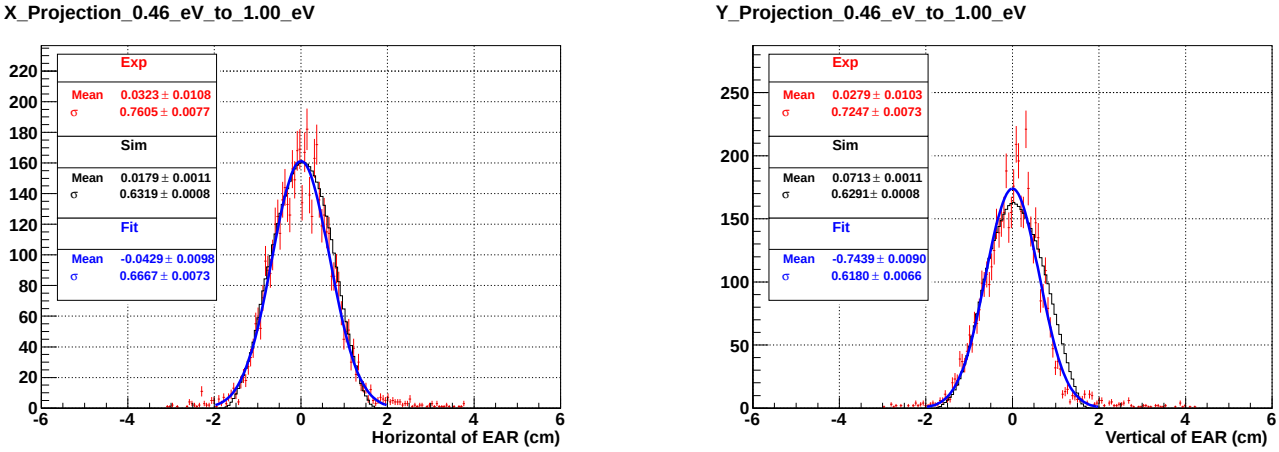

Figure 75. Beam profile in the energy range between 0.46 eV and 1 eV.

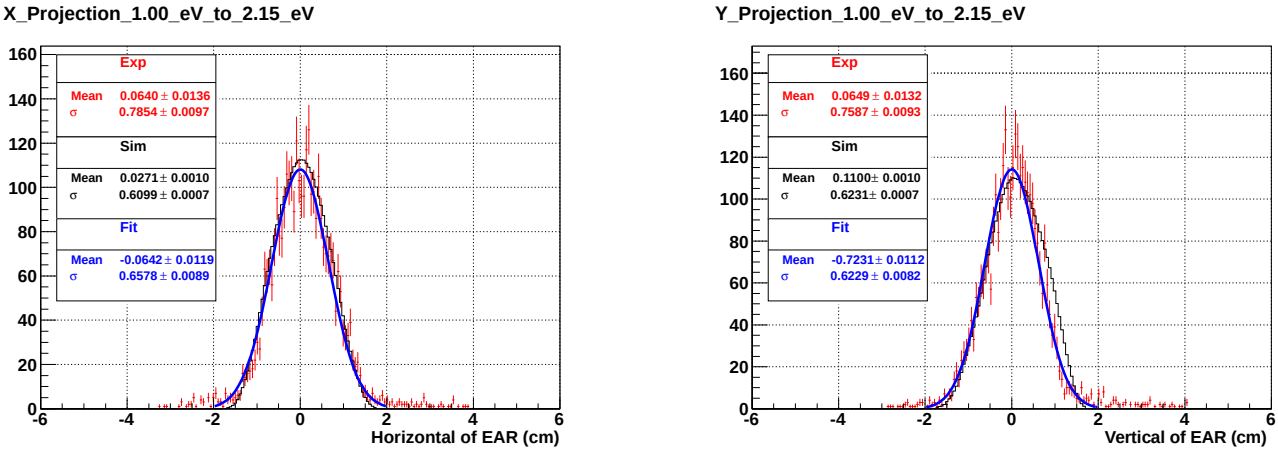

Figure 76. Beam profile in the energy range between 1 eV and 2.15 eV.

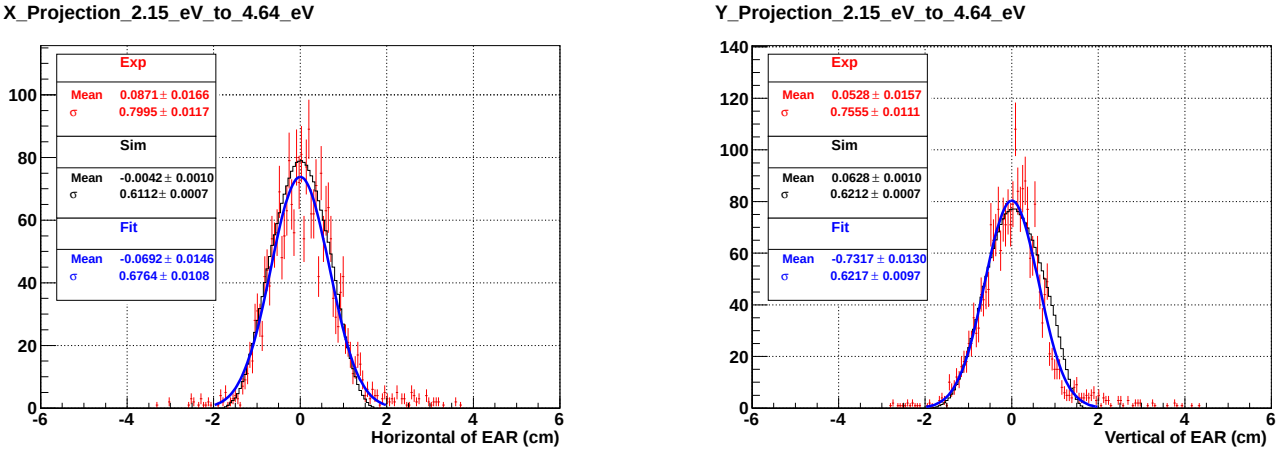

Figure 77. Beam profile in the energy range between 2.15 eV and 4.64 eV.

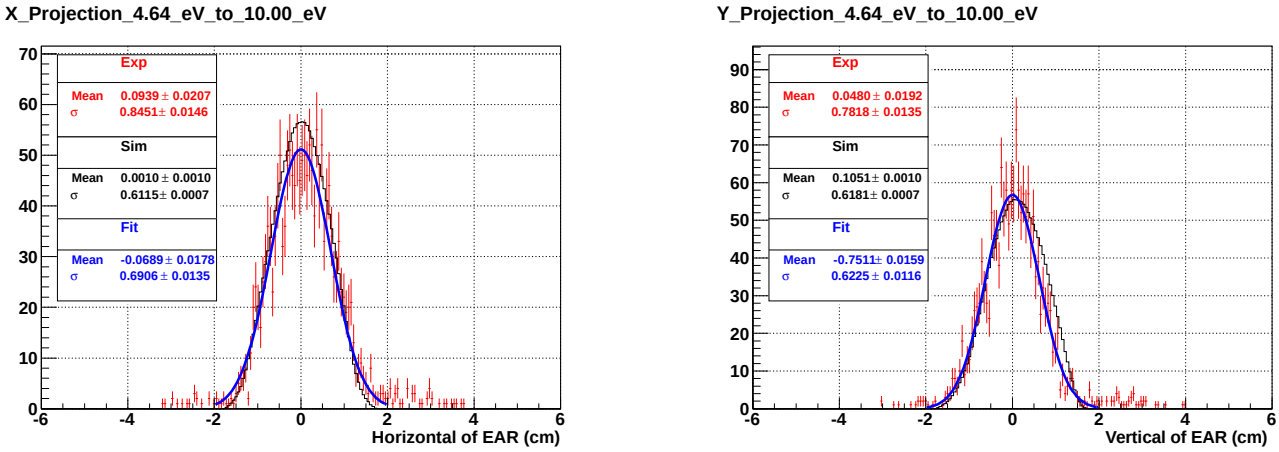

Figure 78. Beam profile in the energy range between 4.64 eV and 10 eV.

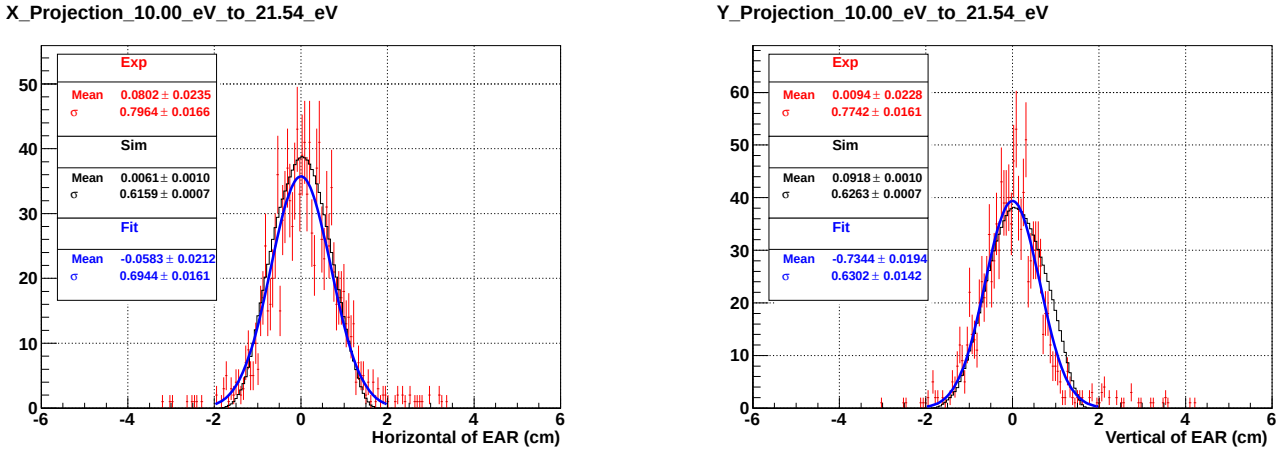

Figure 79. Beam profile in the energy range between 10 eV and 21.54 eV.

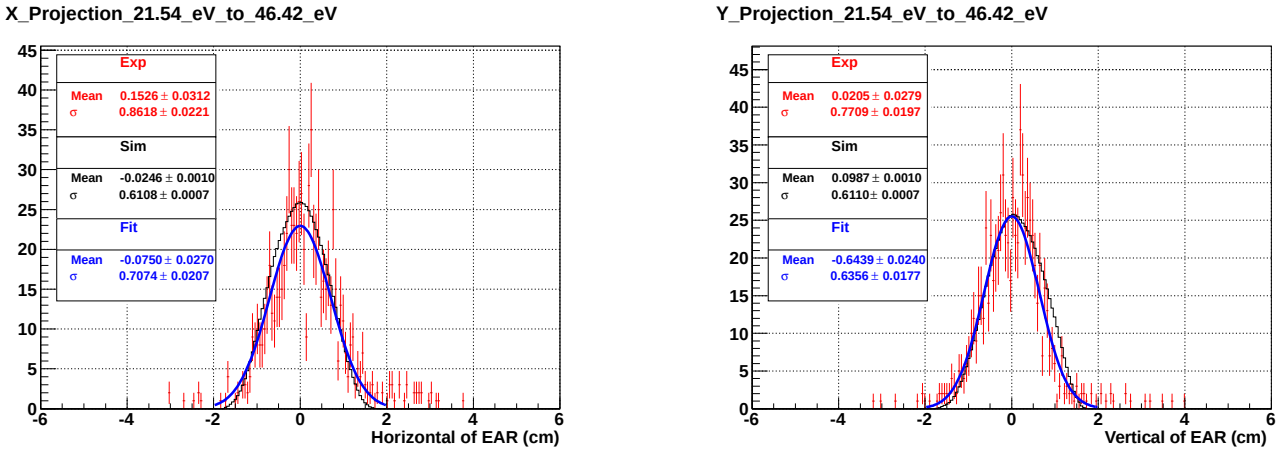

Figure 80. Beam profile in the energy range between 21.54 eV and 46.42 eV.

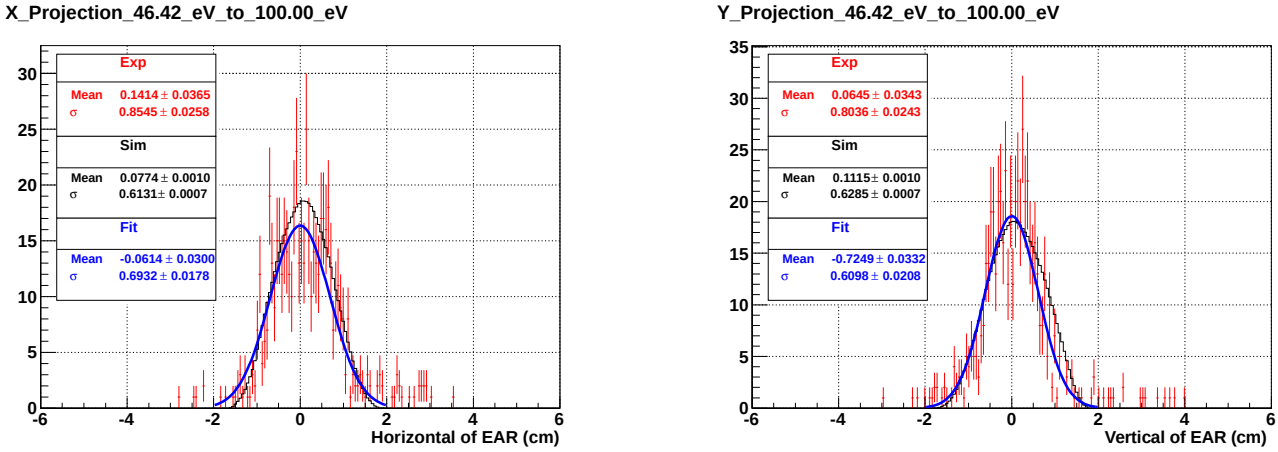

Figure 81. Beam profile in the energy range between 46.42 eV and 100 eV.

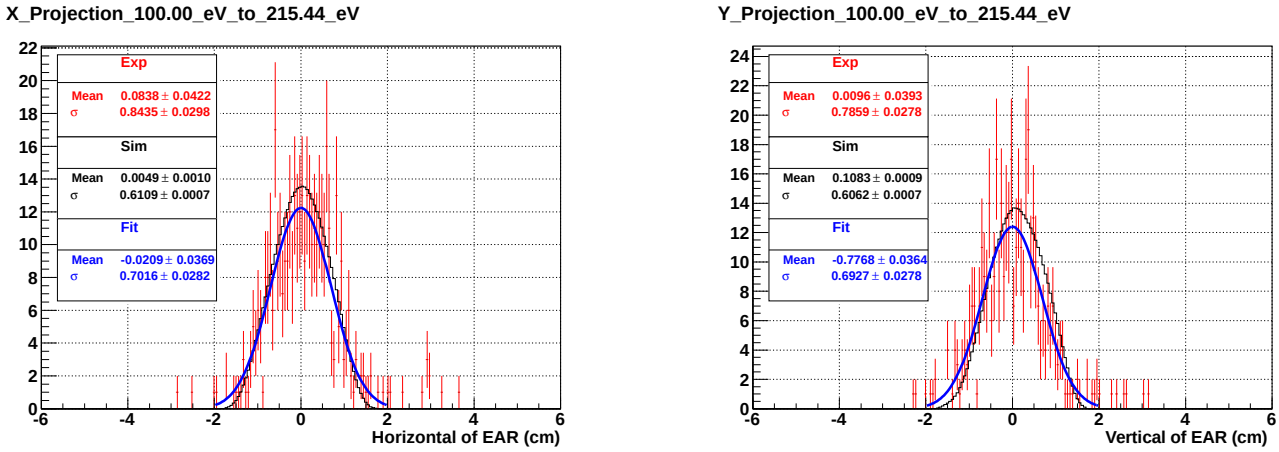

Figure 82. Beam profile in the energy range between 100 eV and 215.44 eV.

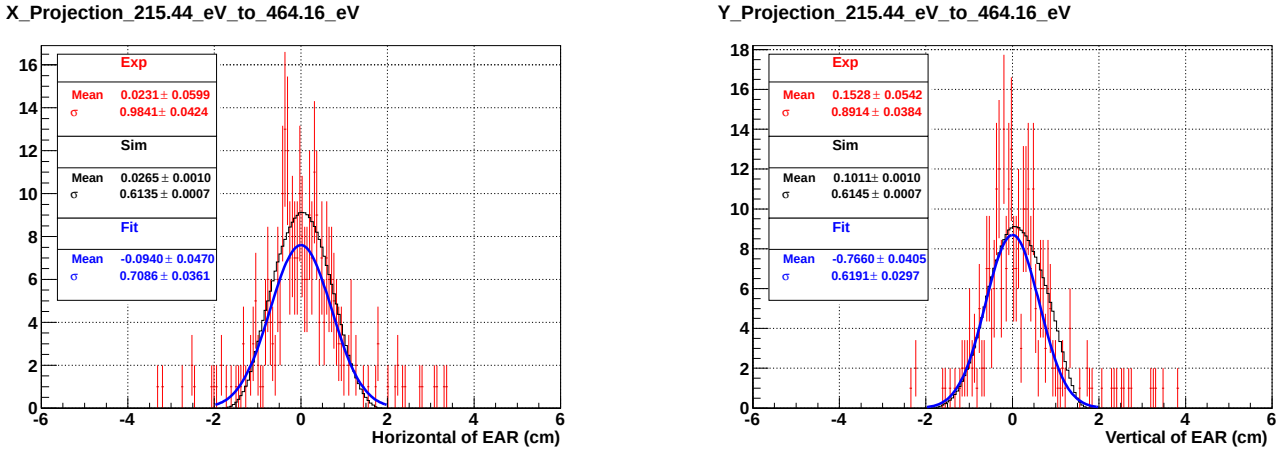

Figure 83. Beam profile in the energy range between 215.44 eV and 464.16 eV.

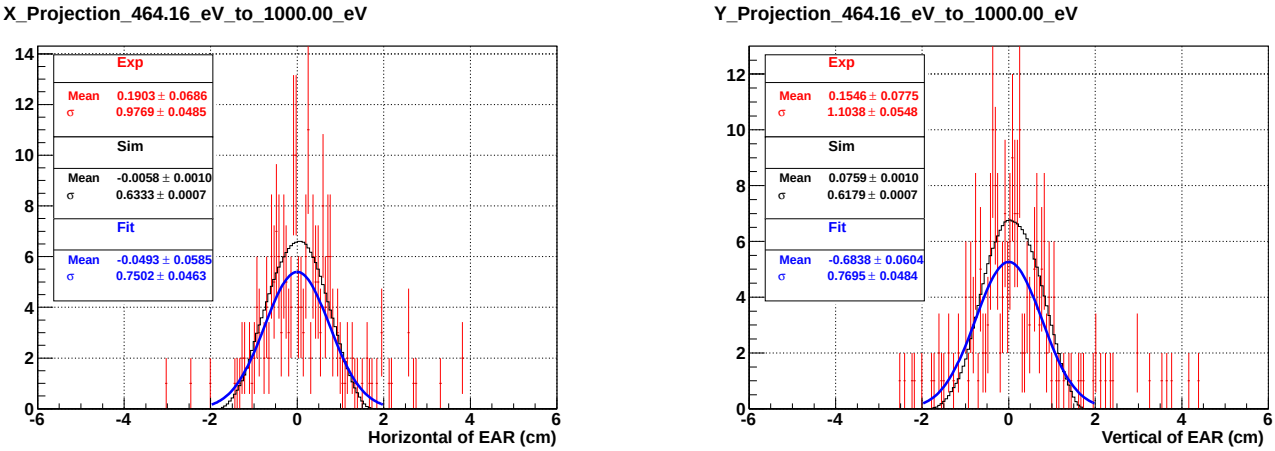

Figure 84. Beam profile in the energy range between 464.16 eV and 1 keV.

5.1.4 17^{th} November 2009

Since the beam profile along the Y axis always looked “bent” (see Figs. (39,54,70), it was decided to monitor its shape for different positions of the second collimator. The table below reports, for each run, the actions taken. All tests were performed in the same conditions, i.e.: XYMG detector close to SILI, mesh voltage 330 V, drift voltage 480 V and converter thickness equal to 24 nm.

Table 7. Details of the measurement performed on 17^{th} November 2009.

Case	Runs	Protons	Actions taken
Ref.	9831 - 9843	5.16884e+16	Reference test
1	9850	2.0e+16	XYMG down by 1 cm. Collimator tilted 4 mm down downstream
2	9851, 9852	2.51e+16	XYMG down by 1 cm. Collimator shifted 4 mm down downstream and upstream
3	9853, 9854	2.309e+16	XYMG down by 1 cm. Collimator tilted 2 mm down upstream (4 mm down parallel shift wrt to nominal run conditions)
4	9858, 9959, 9860	2.944e+16	XYMG down by 1 cm. Collimator tilted further 2 mm down upstream (8 mm down parallel shift wrt to nominal run conditions)
5	9861	1.58e+16	XYMG down by 1 cm. Collimator displacement 9 mm down upstream and 4 mm down downstream wrt to nominal run conditions
6	9863	2.28e+16	XYMG down by 1 cm. Collimator displacement 8 mm down upstream and 6 mm down downstream wrt to nominal run conditions

Fig. 85 and Fig. 86 show a comparison of the beam profile along the Y axis for different test conditions. The role played by the second collimator with respect to the shape of the beam profile is evident.

All curves are normalized to the same maximum. Additional tests were performed, but are not here reported.

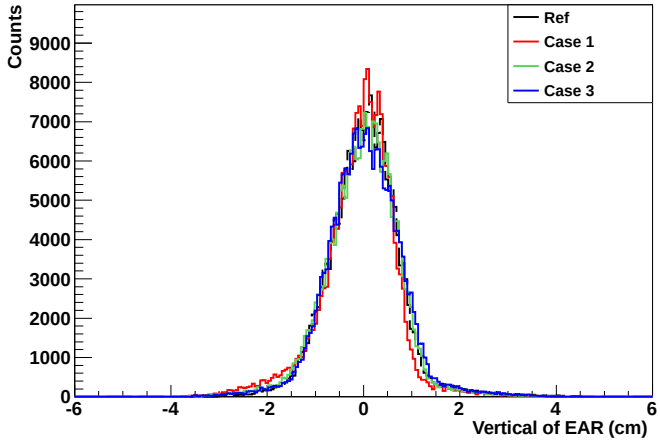

Figure 85. Comparison of the beam profile along the Y axis (all neutron energies considered) for different positions of the second collimator.

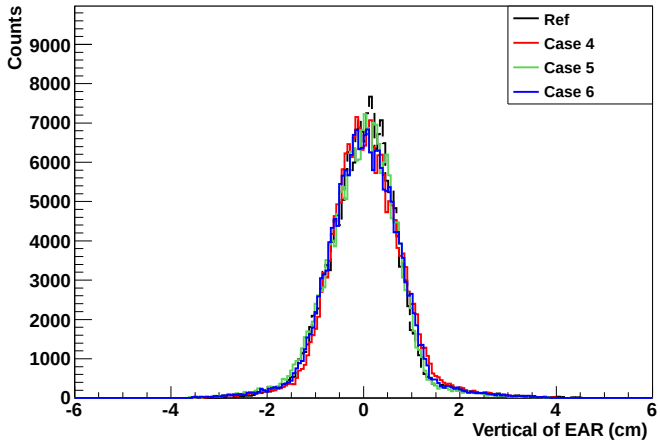

Figure 86. Comparison of the beam profile along the Y axis (all neutron energies considered) for different positions of the second collimator.

5.2 2010

Starting from 2010, only the neutron/charge particle converter of 2 μm thickness was used. The detector was positioned at a TOF distance of 183.74 m. Moreover borated water, and not anymore simple H_2O, was used for moderating the neutrons exiting from the spallation target.

5.2.1 19^{th} May 2010

The first beam image got in 2010 clearly showed some problems.

Table 8. Details of the measurement performed the 19^{th} May 2010.

Configuration	TOF distance of 183.74 m
Runs	9919, 9920, 9921
Protons	1.7513e+16
Converter thickness	2 μm
Mesh Voltage	325 V - 340 V [2]
Drift Voltage	565 V

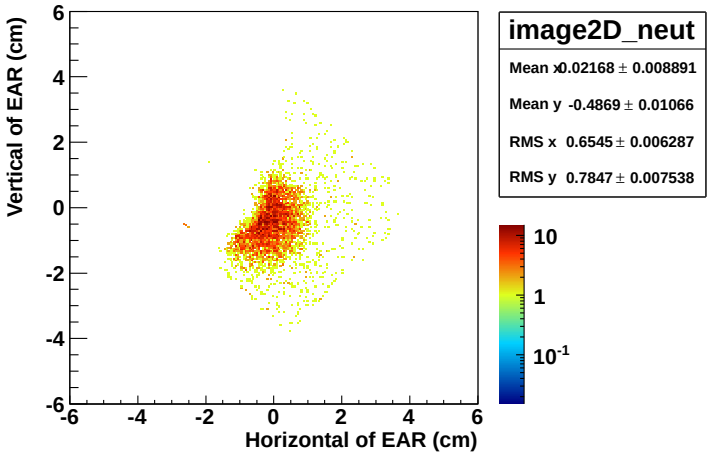

Figure 87. Beam image (μMegas detector seen in the reference system of the EAR.).

[2] A voltage equal to 325 V was set in run 9929, while in the runs 9920 and 9921 the voltage in the mesh was set to 340 V. Nonetheless here results are merged to accumulate more statistics

5.2.2 20^{th} May 2010

The second collimator was moved 2 mm down upstream in order to see if the beam was "cut" due to misalignment, but no positive effect was obtained.

Table 9. Details of the measurement performed the 20^{th} May 2010.

Configuration	TOF distance of 183.74 m
Runs	9922, 9923, 9924
Protons	4.972e+15
Converter thickness	2 μm
Mesh Voltage	340 V
Drift Voltage	565 V

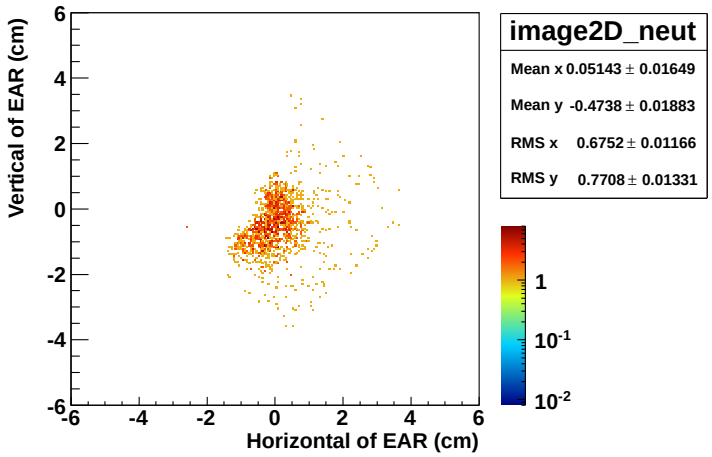

Figure 88. Beam image (μMegas detector seen in the reference system of the EAR.).

5.2.3 21^{st} - 24^{th} May 2010

As a further trial, the second collimator was moved 2 mm up upstream with respect to the position held on 19 th May (or equivalently 4 mm up upstream with respect to the position held on 20^{th} May).

Table 10. Details of the measurement performed in the period 21^{st} - 24^{th} May 2010.

Configuration	TOF distance of 183.74 m
Runs	9925, 9926, 9927, 9928, 9930, 9931, 9932, 9936, 9937, 9938, 9939, 9940, 9941, 9942, 9943, 9944, 9945, 9946, 9947, 9948, 9949, 9950, 9952, 9953, 9954, 9955, 9956, 9957
Protons	2.867312e+17
Converter thickness	2 μm
Mesh Voltage	340 V
Drift Voltage	565 V

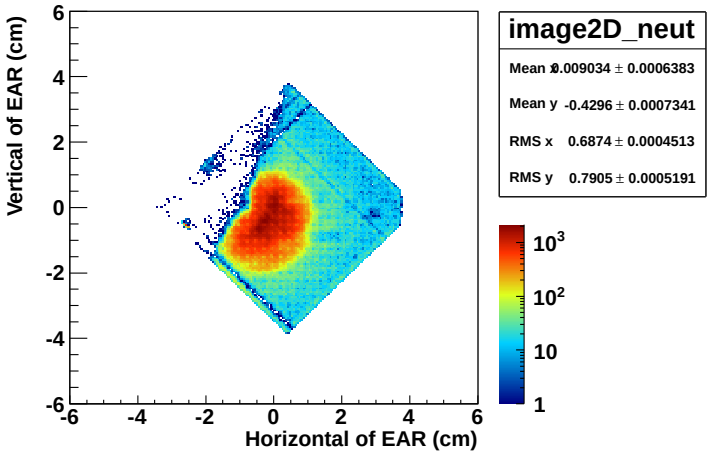

Figure 89. Beam image (μMegas detector seen in the reference system of the EAR.).

5.2.4 25^{th} May 2010

Once excluded that the problem was due to the collimator, the neutron/charged particle converter was rotated by 90° to check if part of the deposit detached from the backing. No striking evidence of lack of uniformity of the $^{10}B_4C$ deposit was obtained.

Table 11. Details of the measurement performed the 25^{th} May 2010.

Configuration	TOF distance of 183.74 m
Runs	9958, 9959, 9960, 9961, 9962, 9963, 9964
Protons	1.1288e+16
Converter thickness	2 μm
Mesh Voltage	340 V
Drift Voltage	565 V

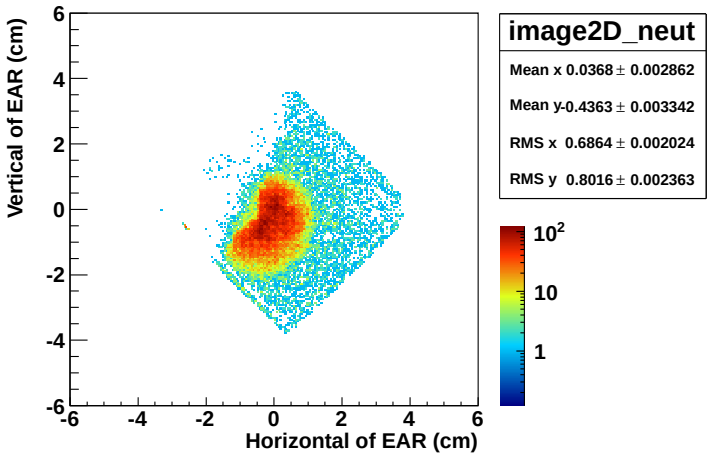

Figure 90. Beam image (μMegas detector seen in the reference system of the EAR.).

5.2.5 26^{th} May 2010

The XYMG detector was shifted 15 mm to the left to search again some trace of lack of uniformity of the neutron/charge particle converter, but it became visible that the problem was in the detector itself. A huge portion of it was not properly working.

Table 12. Details of the measurement performed the 26^{th} May 2010.

Configuration	TOF distance of 183.74 m
Runs	9973, 9974, 9975, 9976, 9977
Protons	2.7781e+16
Converter thickness	2 μm
Mesh Voltage	325 V
Drift Voltage	565 V

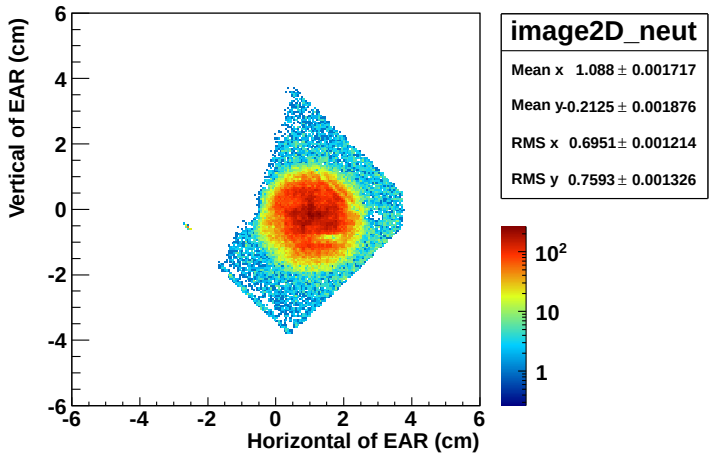

Figure 91. Beam image (μMegas detector seen in the reference system of the EAR.).

5.2.6 2^{nd} June 2010

Different tests were performed: the drift and mesh voltage were changed, the integration and derivation time of the amplifier were increased by 50 ns, the gas and gassiplex connections were checked. In the end the detector was removed.

Table 13. Details of the measurement performed the 2^{nd} June 2010.

Configuration	TOF distance of 183.74 m
Runs	10026, 10027, 10028, 10029, 10030, 10031, 10032, 10033 10034, 10035, 10036, 10037, 10038, 10039, 10040
Protons	6.5521e+16
Converter thickness	2 μm
Mesh Voltage	300 -365 V
Drift Voltage	360 - 500 V

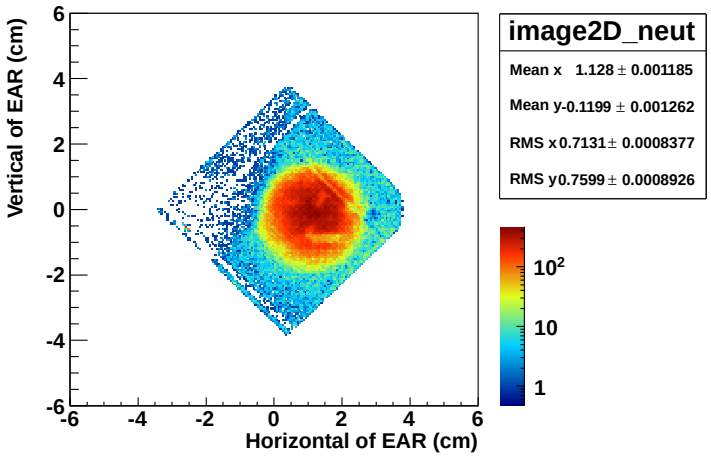

Figure 92. Beam image (μMegas detector seen in the reference system of the EAR.).

5.2.7 14^{th} June 2010

After checking the best mesh and drift operation region, the detector was put again in position. The previously observed problems were due to 2 factors:

1. the mesh of the XYMG detector is not completely flat. This causes the electric field to change in different parts of the multiplication region, with field lines driving the electrons more towards some strips than towards others.

2. the coupling of the mesh and drift voltages set in the previous period, corresponded to a low transparency of the mesh.

Table 14. Details of the measurement performed the 14^{th} June 2010.

Configuration	TOF distance of 183.74 m
Runs	10097, 10098, 10099, 10100, 10101, 10102, 10103
	10104, 10105, 10106, 10107, 10108, 10109, 10110
	10111, 10112, 10113, 10114, 10115, 10116, 10117
	10118, 10119, 10120, 10121, 10122, 10123, 10124, 10125
Protons	5.2592665e+17
Converter thickness	2 μm
Mesh Voltage	330 V [3]
Drift Voltage	385 V [4]

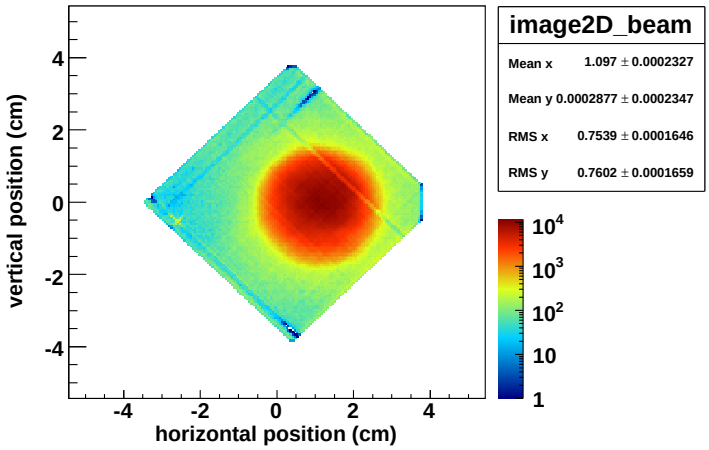

Figure 93. Beam image (μMegas detector seen in the reference system of the EAR.).

[4] In a few runs the drift voltage was set to 350 V and 380 V.
[5] In a few runs the drift voltage was set to 405 V and 415 V.

The study of the beam profile was performed only for data taken from the 14^{th}, because before the beam image was not complete. Since one of the main concerns resides in the shape of the beam profile, Fig 94 shows that along the X and Y axis when all neutron energies are considered. In order to better see the shape of the beam profile, no fit is superimposed.

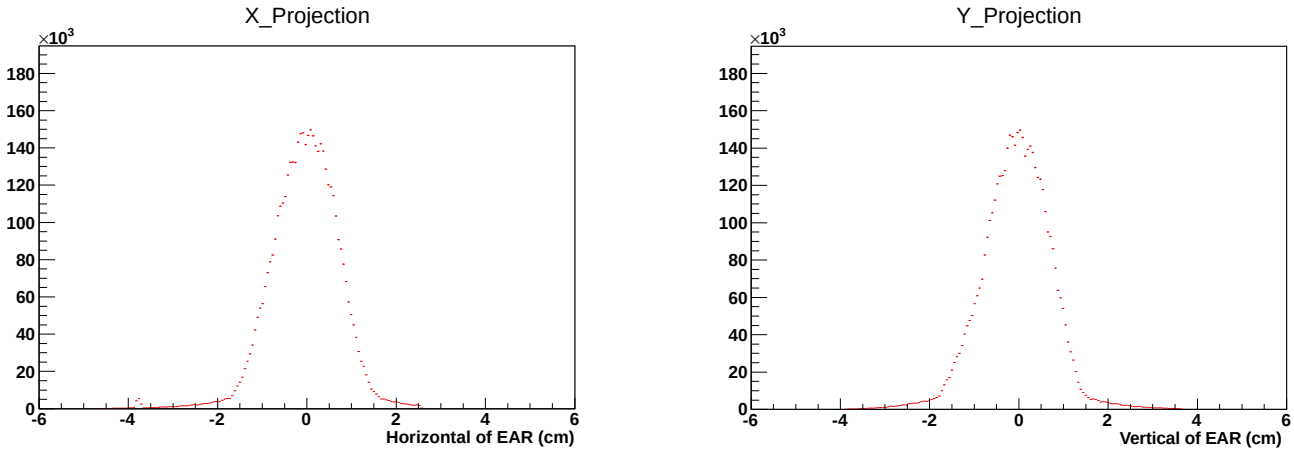

Figure 94. Beam profile obtained by considering all neutron energies. The left panel refers to the X axis, while the right one concerns the Y axis.

The beam profiles still look slightly bent.

Before starting studying the evolution of the beam profile as a function of the incident neutron energy, the best fit was looked for. 3 fits were compared: a simple Gaussian, the convolution of a Gaussian with a rectangular function and a Gaussian superimposed to a quadratic background. The difference among the 3 cases was very small, therefore the first fit was employed for simplicity.

The following pictures show the comparison between the beam profile for different neutron energy ranges and simulations performed by the FLUKA [19] group in n_TOF. The beam profiles obtained accounting for the presence of the PCB with GEANT4 simulations are not shown because of two reasons: on one side the statistics obtained was too low to be conclusive and on the other side the ultimate goal is the determination of the beam spatial characteristics at the XYMG position when the profiler is replaced by a sample (i.e. in absence of the XYMG). The fit to experimental data is always superimposed. Statistical panels report the displacement of the beam profiles along the reference axis, but all experimental curves are shifted so that their peak position coincides with that of the simulated ones they are confronted to.

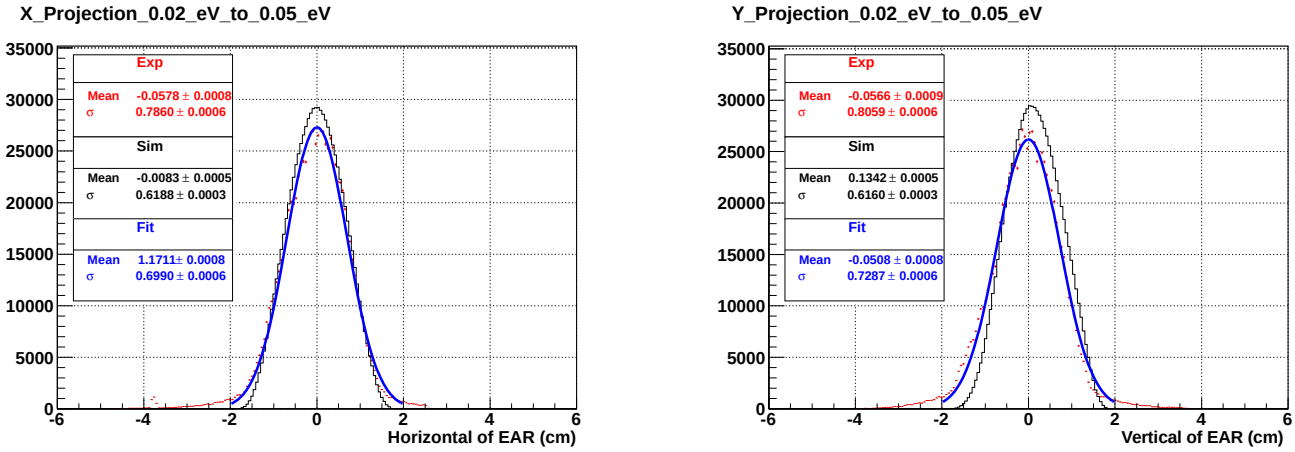

Figure 95. Beam profile in the energy range between 0.025 eV and 0.05 eV.

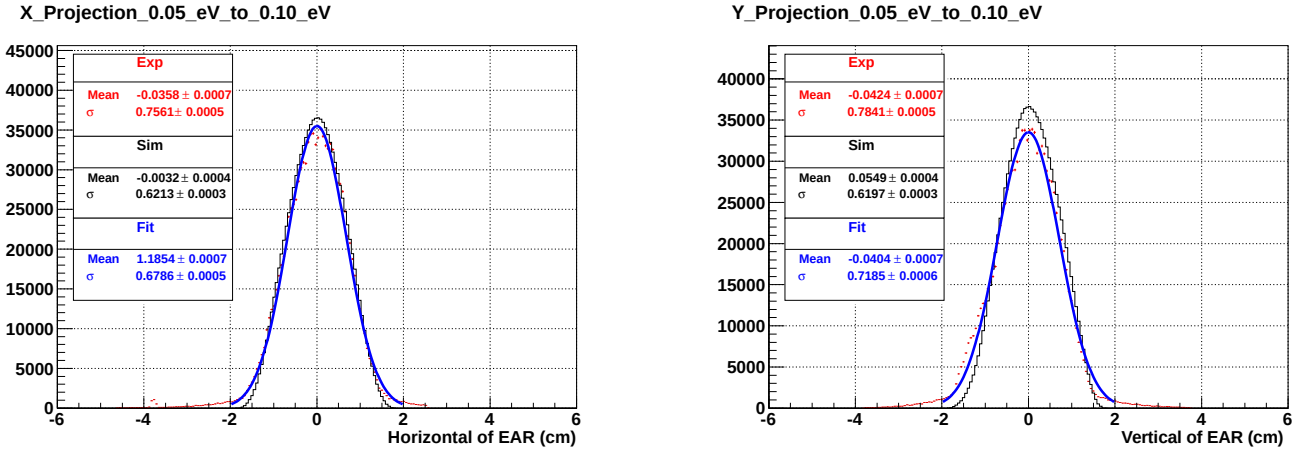

Figure 96. Beam profile in the energy range between 0.05 eV and 0.1 eV.

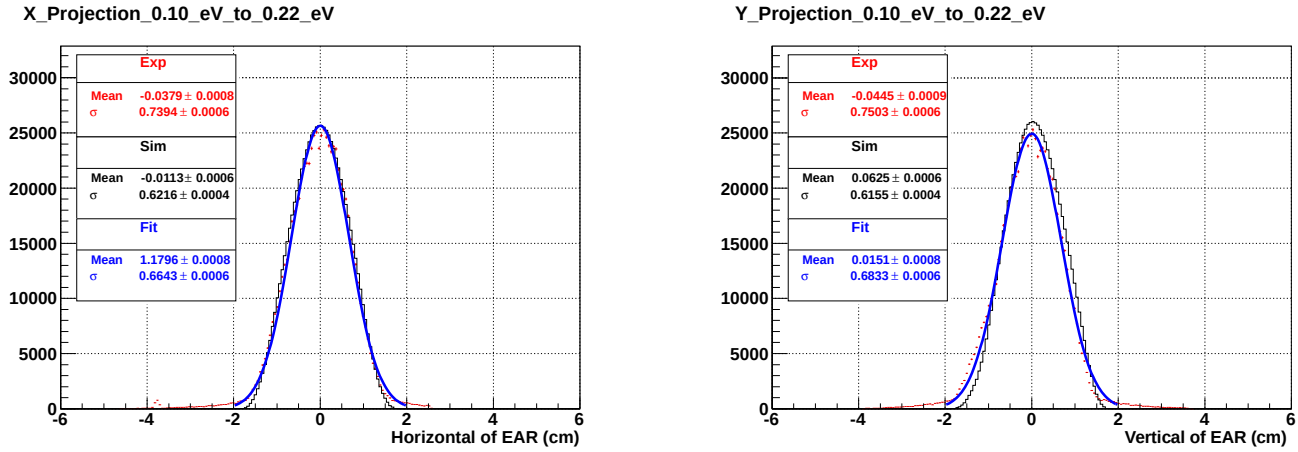

Figure 97. Beam profile in the energy range between 0.1 eV and 0.22 eV.

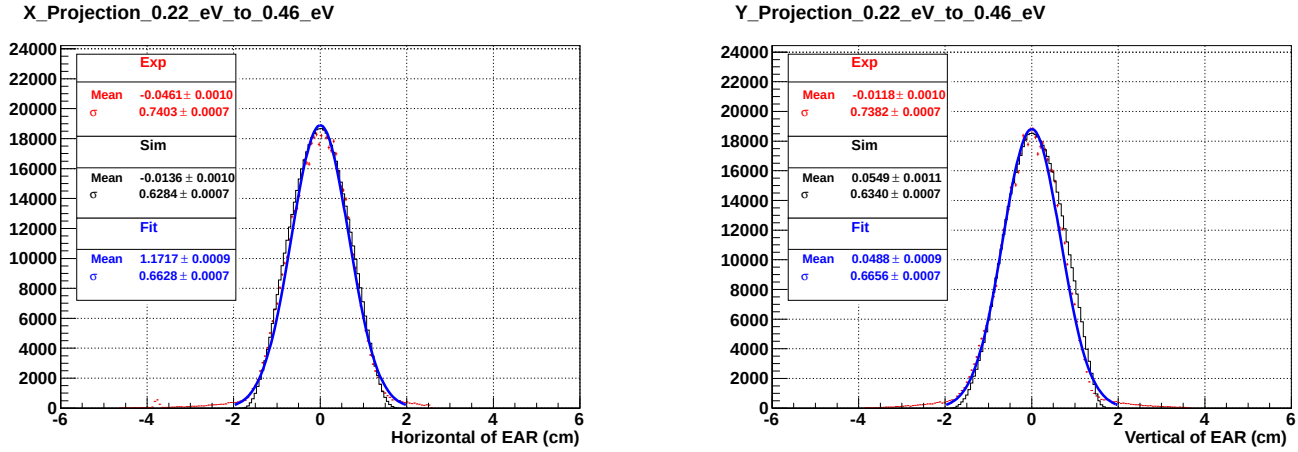

Figure 98. Beam profile in the energy range between 0.22 eV and 0.46 eV.

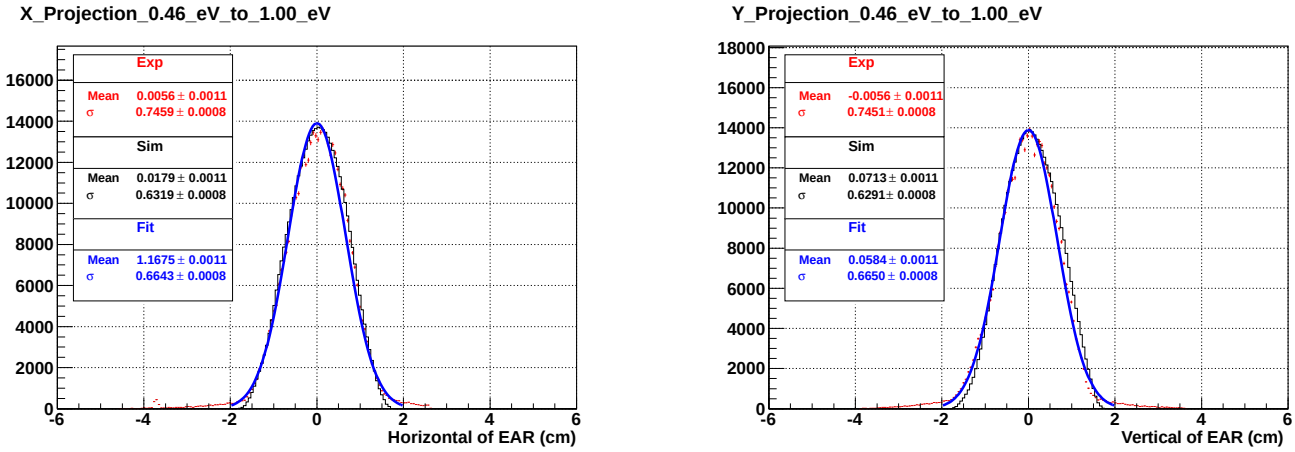

Figure 99. Beam profile in the energy range between 0.46 eV and 1 eV.

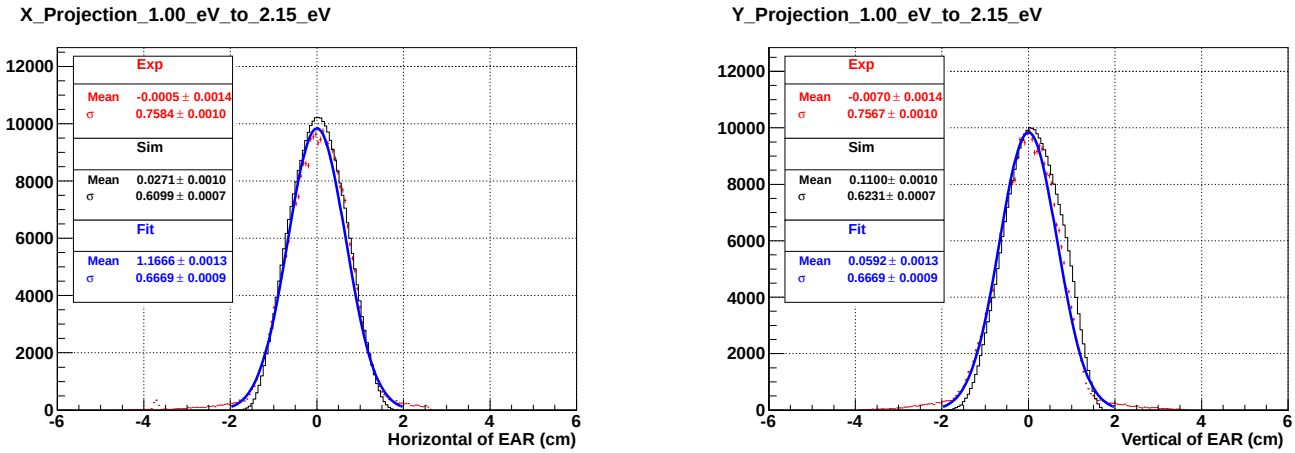

Figure 100. Beam profile in the energy range between 1 eV and 2.15 eV.

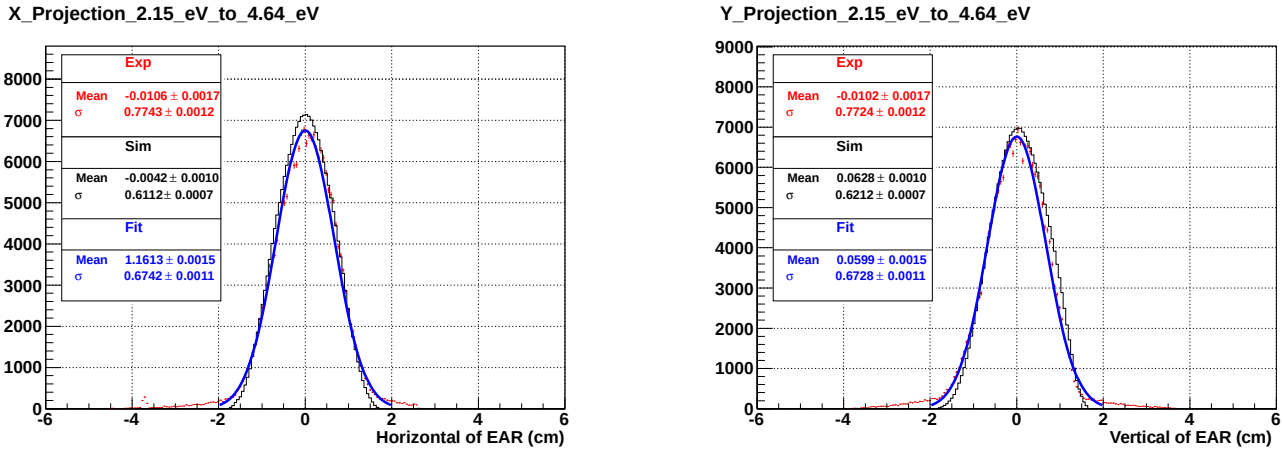

Figure 101. Beam profile in the energy range between 2.15 eV and 4.64 eV.

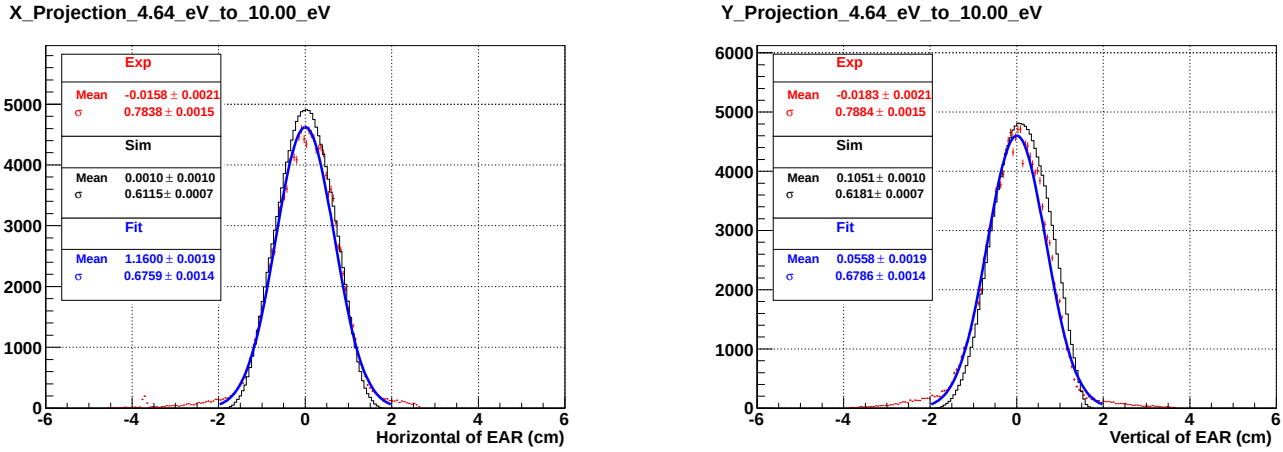

Figure 102. Beam profile in the energy range between 4.64 eV and 10 eV.

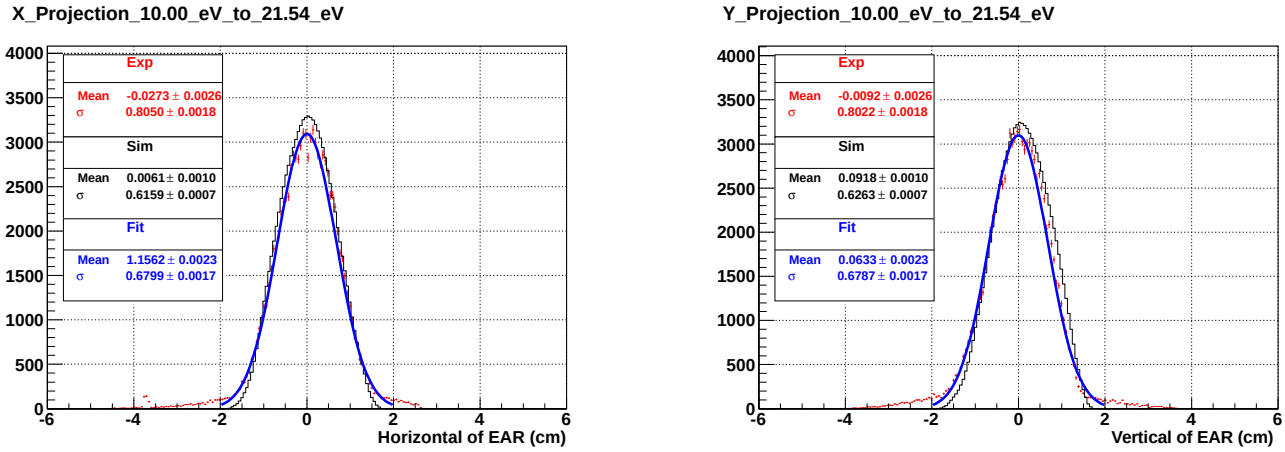

Figure 103. Beam profile in the energy range between 10 eV and 21.54 eV.

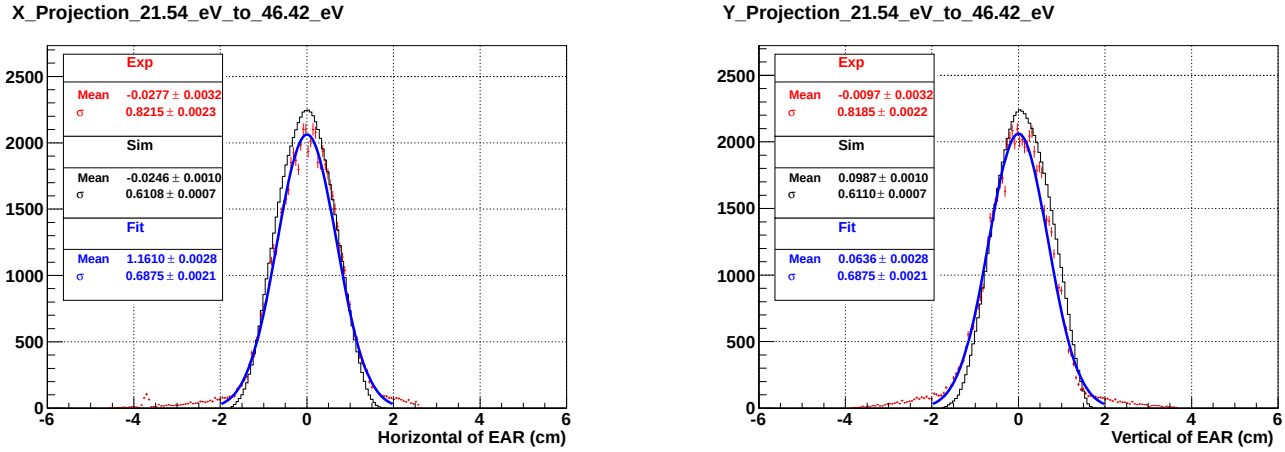

Figure 104. Beam profile in the energy range between 21.54 eV and 46.42 eV.

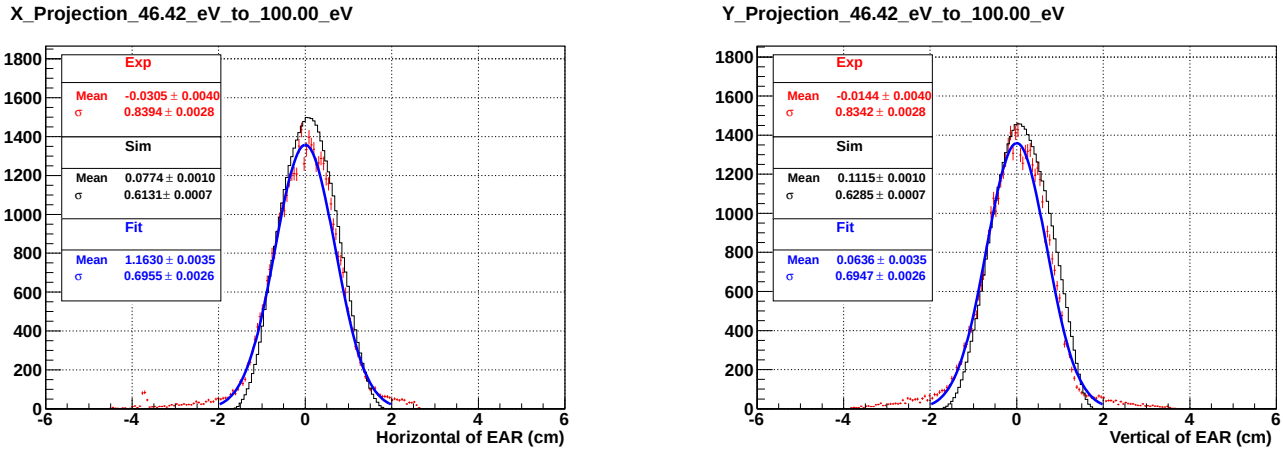

Figure 105. Beam profile in the energy range between 46.42 eV and 100 eV.

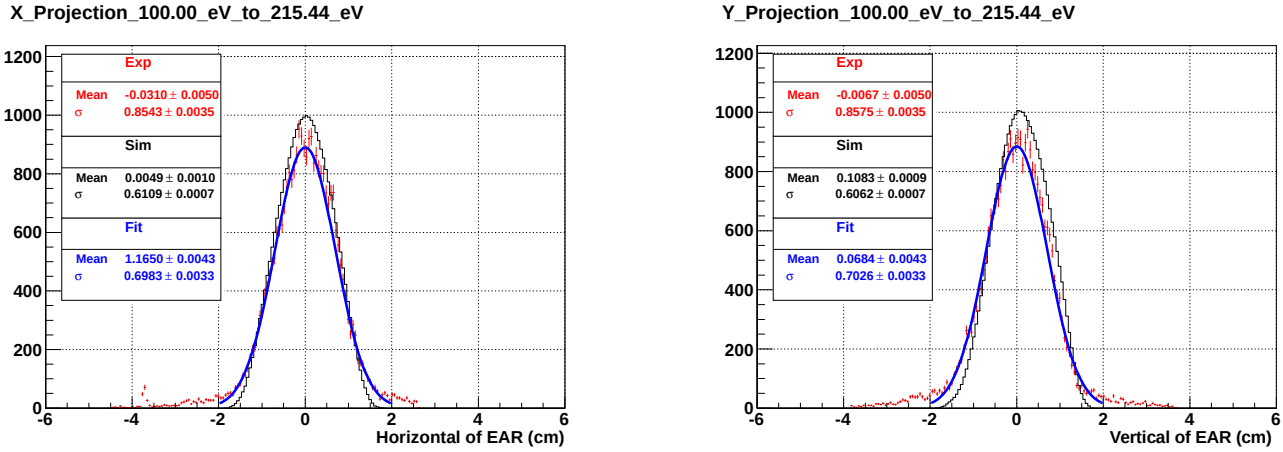

Figure 106. Beam profile in the energy range between 100 eV and 215.44 eV.

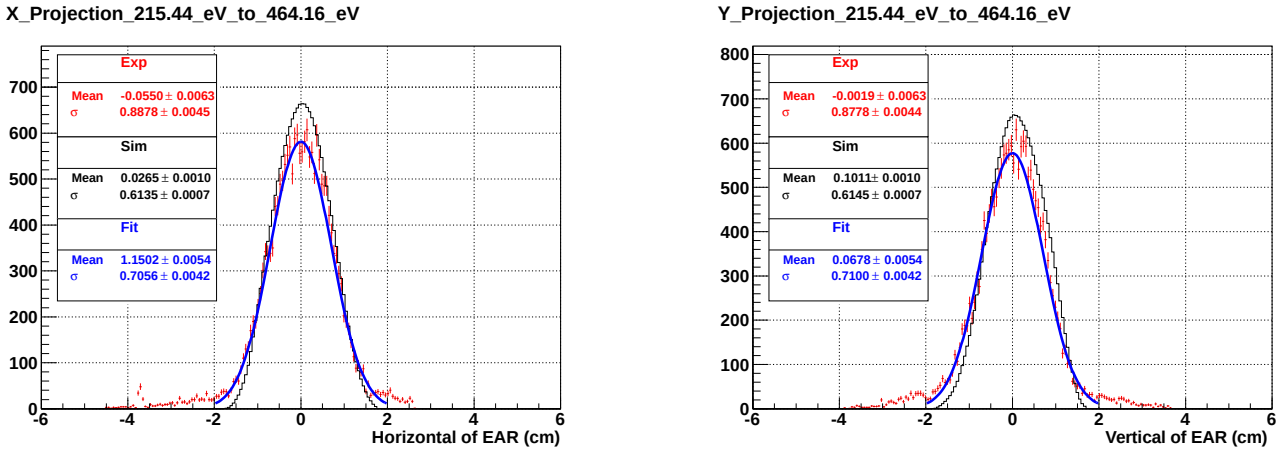

Figure 107. Beam profile in the energy range between 215.44 eV and 464.16 eV.

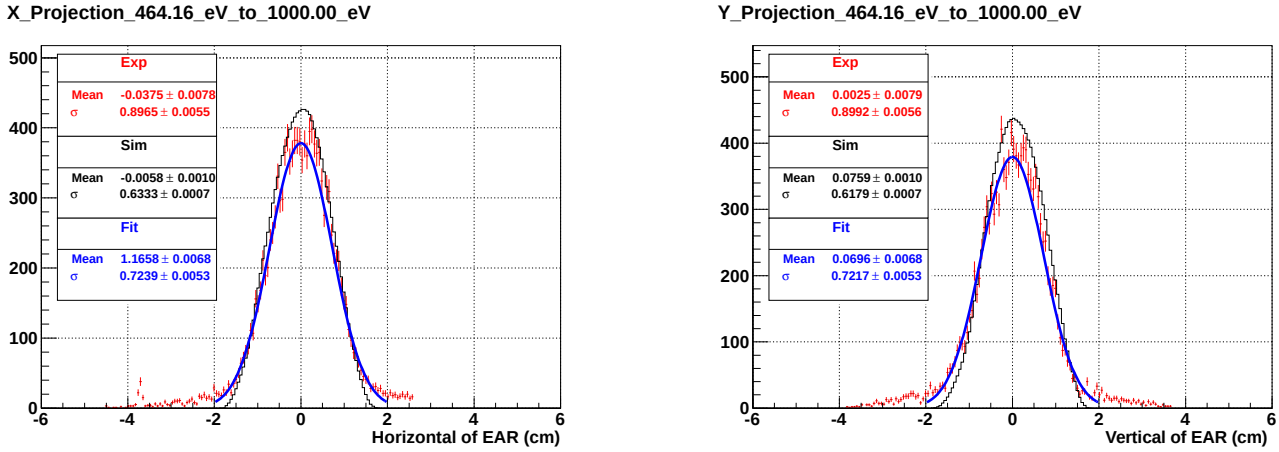

Figure 108. Beam profile in the energy range between 464.16 eV and 1 keV.

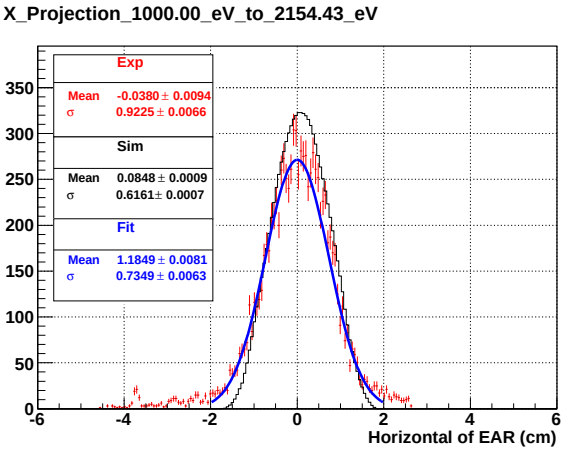

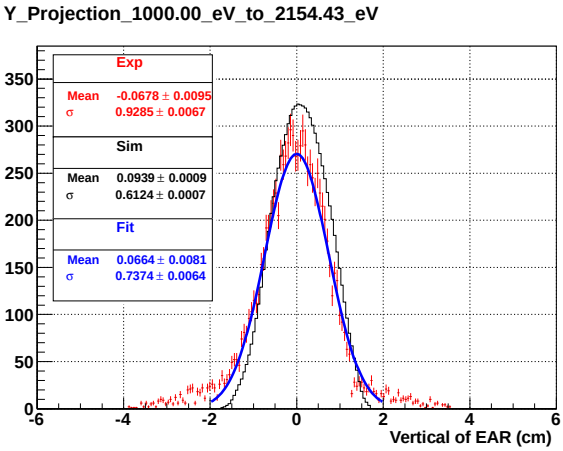

Figure 109. Beam profile in the energy range between 1 keV and 2.15 keV.

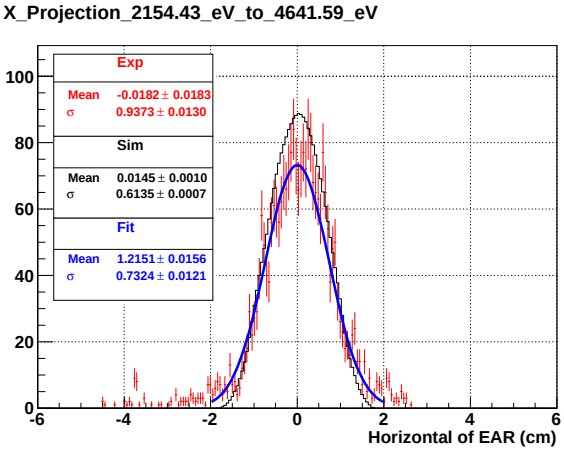

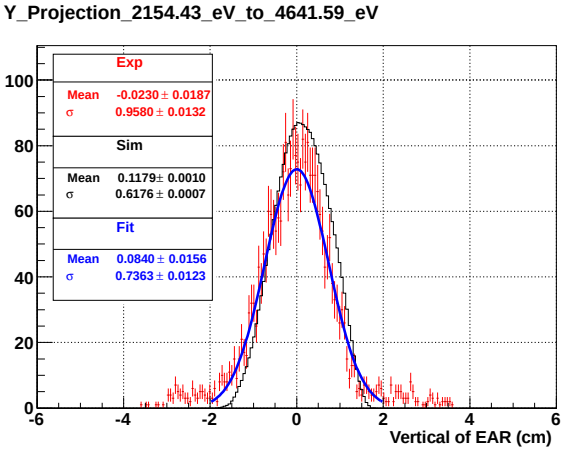

Figure 110. Beam profile in the energy range between 2.15 keV and 4.64 keV.

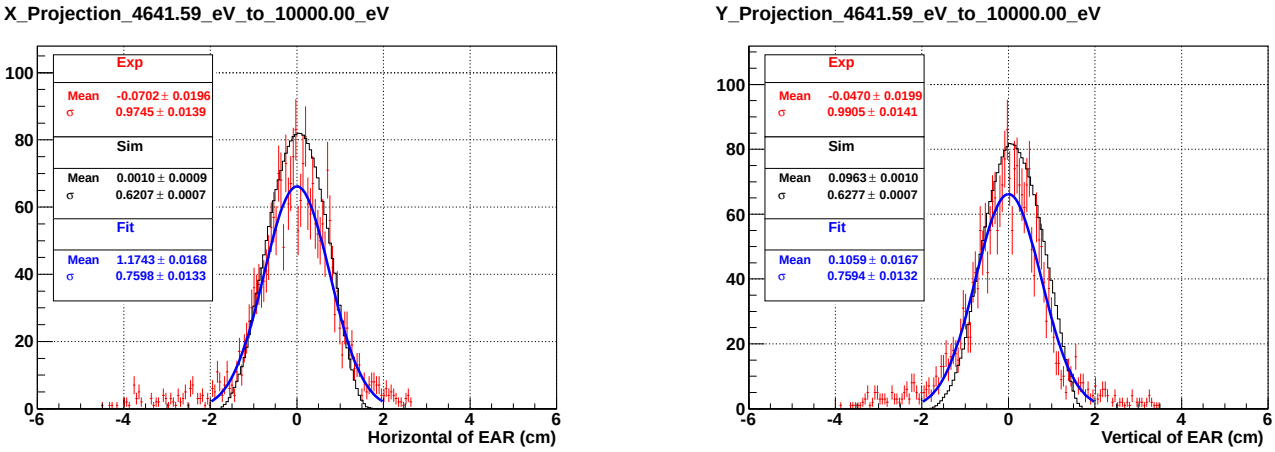

Figure 111. Beam profile in the energy range between 4.64 keV and 10 keV.

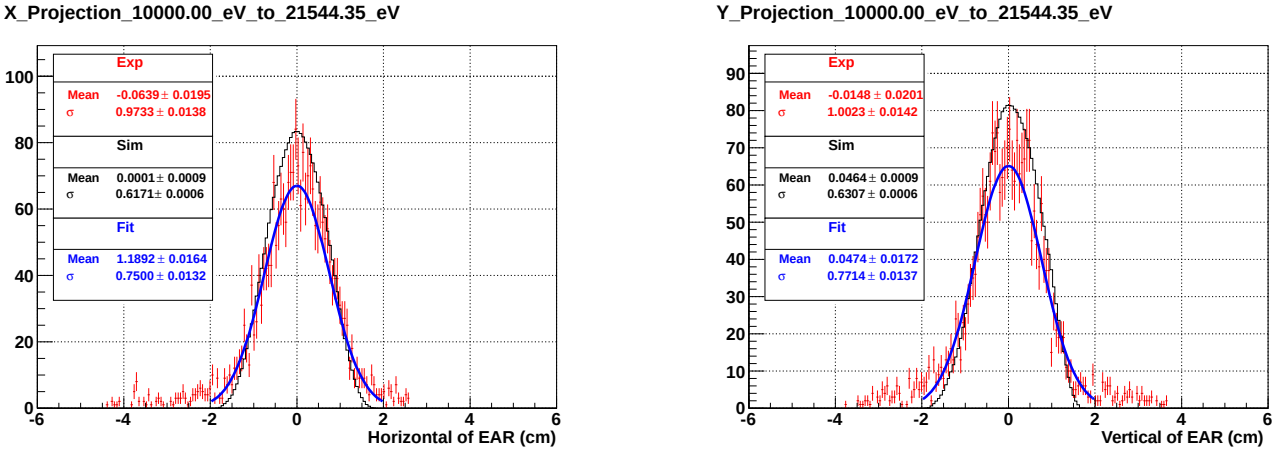

Figure 112. Beam profile in the energy range between 10 keV and 21.5 keV.

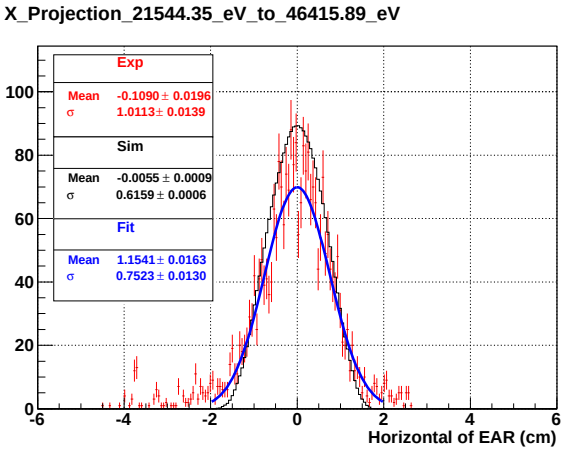

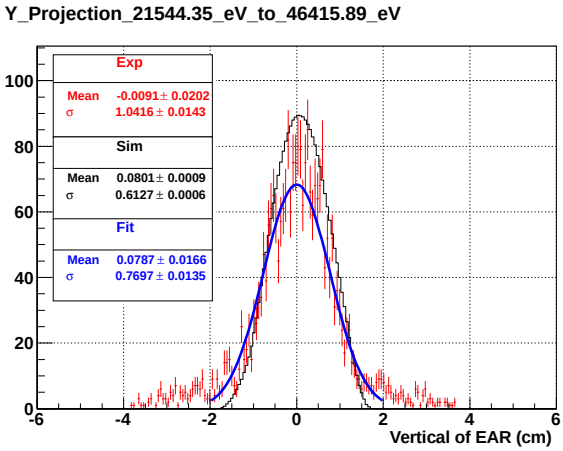

Figure 113. Beam profile in the energy range between 21.5 keV and 46.4 keV.

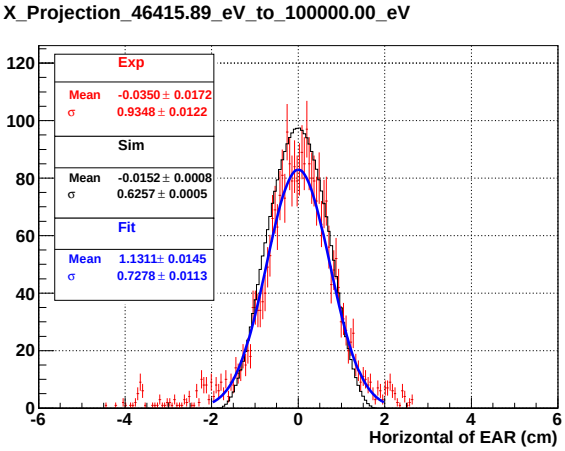

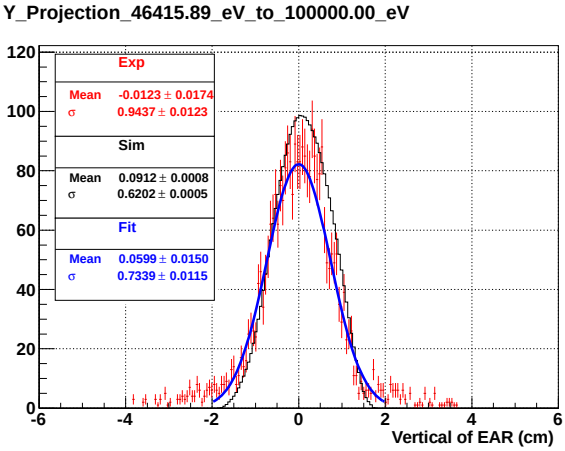

Figure 114. Beam profile in the energy range between 46.4 keV and 100 keV.

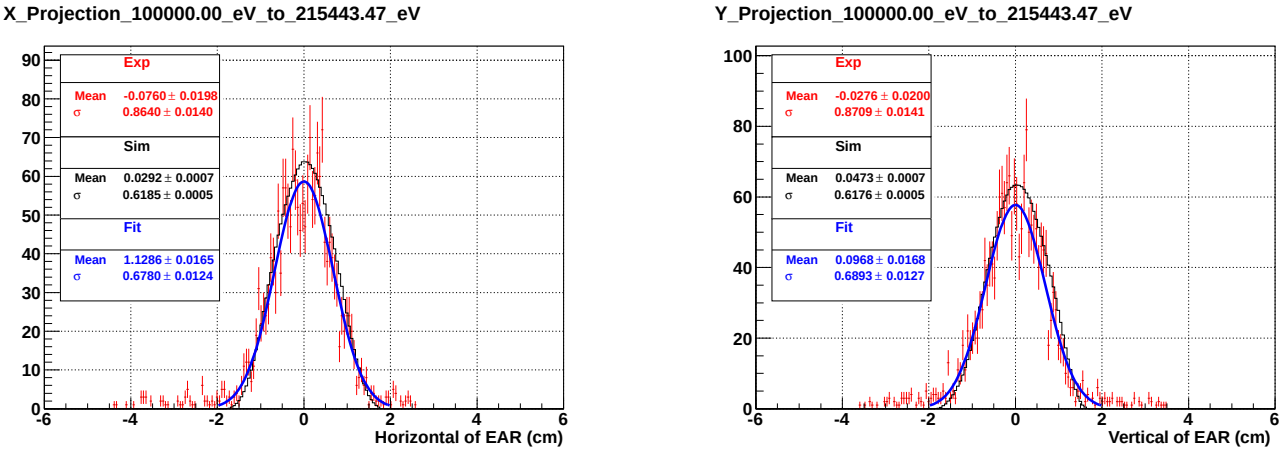

Figure 115. Beam profile in the energy range between 100 keV and 215.4 keV.

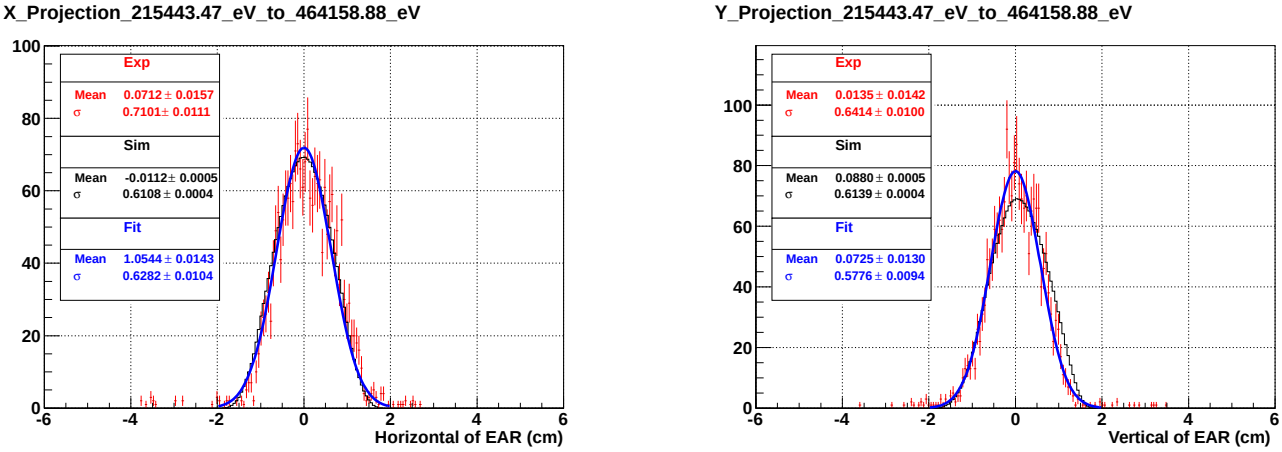

Figure 116. Beam profile in the energy range between 215.4 keV and 464.15 keV.

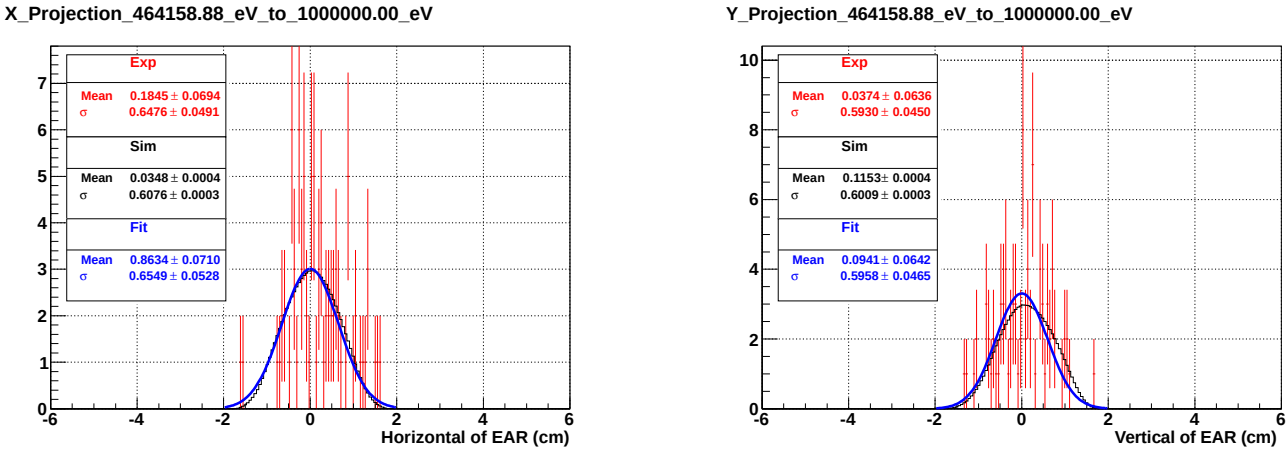

Figure 117. Beam profile in the energy range between 464.15 keV and 1 MeV.

Table 15 reports the widths of the beam profile obtained by the fit as a function of the neutron energy, while in Fig. 118 the corresponding plots are shown.

Table 15. Fit parameters. A 2D Gaussian fit was considered.

Energy range	σ_x **[cm]**	$\delta\sigma_x$ **[cm]**	σ_y **[cm]**	$\delta\sigma_y$ **[cm]**	χ^2
0.0215443 eV - 0.0464159 eV	0.6990	0.0006	0.7287	0.0006	10.02
0.0464159 eV - 0.1 eV	0.6786	0.0005	0.7185	0.0006	13.54
0.1 eV - 0.215443 eV	0.6643	0.0006	0.6833	0.0006	9.92
0.215443 eV - 0.464159 eV	0.6628	0.0007	0.6656	0.0007	7.69
0.464159 eV - 1 eV	0.6643	0.0008	0.6650	0.0008	6.25
1 eV - 2.15443 eV	0.6669	0.0009	0.6669	0.0009	5.04
2.15443 eV - 4.64159 eV	0.6742	0.0011	0.6728	0.0011	4.01
4.64159 eV - 10 eV	0.6759	0.0014	0.6786	0.0014	3.13
10 eV - 21.5443 eV	0.6799	0.0017	0.6787	0.0017	2.58
21.5443 eV - 46.4159 eV	0.6875	0.0021	0.6875	0.0021	2.06
46.4159 eV - 100 eV	0.6955	0.0026	0.6947	0.0026	1.62
100 eV - 215.443 eV	0.6893	0.0033	0.7206	0.0033	1.24
215.443 eV - 464.159 eV	0.7056	0.0042	0.7100	0.0042	1.06
464.159 eV - 1 keV	0.7239	0.0053	0.7217	0.0053	0.86
1 keV - 2.15443 keV	0.7349	0.0063	0.7374	0.0064	0.77
2.15443 keV - 4.64159 keV	0.7324	0.0121	0.7363	0.0123	0.28
4.64159 keV - 10 keV	0.7598	0.0133	0.7594	0.0132	0.28
10 keV - 21.5443 keV	0.7500	0.0132	0.7714	0.0137	0.28
21.5443 keV - 46.4159 keV	0.7523	0.0130	0.7697	0.0135	0.29
46.4159 keV - 100 keV	0.7278	0.0113	0.7339	0.0115	0.30

100 keV - 215.443 keV	0.6780	0.0124	0.6893	0.0127	0.22
215.443 keV - 464.159 keV	0.6282	0.0104	0.5776	0.0094	0.25
464.159 keV - 1 MeV	0.6549	0.0528	0.5958	0.0465	0.07

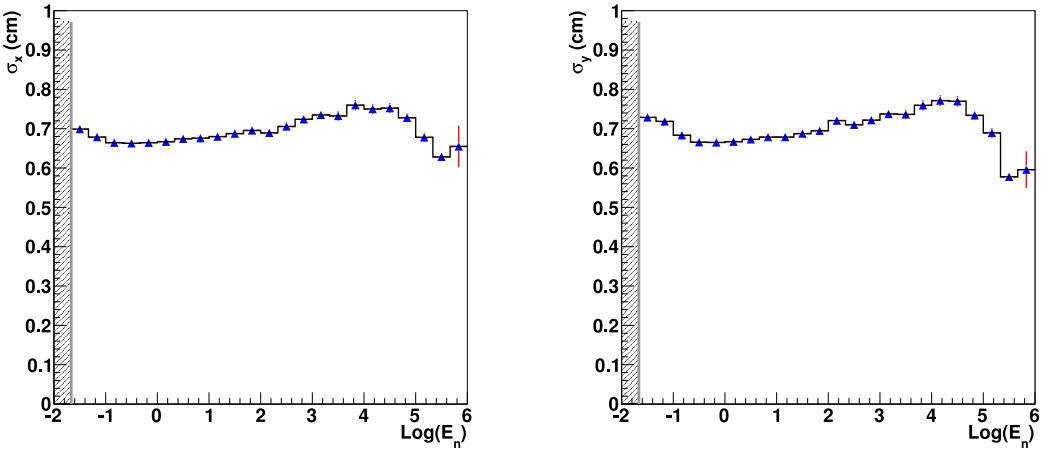

Figure 118. Relation between the Gaussian width obtained by fitting the beam profiles and the neutron energy.

The beam interception factor was extracted at the XYMG position for two samples: one with ⌀ = 1 cm and the other with ⌀ = 2 cm. Given the huge horizontal misalignment of the detector with respect to the center of the beam, the computation was performed by correcting for the shifts along both Cartesian axis. Experimental results are reported in Table 16 and Fig 119 shows the corresponding plots. It was decided not to extract the bif from the fit to the experimental data because this operation would not correct for the presence of the PCB and therefore would not improve the results.

Table 16. Experimental beam interception factor for 2 samples of different diameters.

Energy range	**B.I.F. for sample ⌀ = 1 cm [%]**	**B.I.F. for sample ⌀ = 2 cm [%]**
0.0215443 eV - 0.0464159 eV	25.085 ± 0.054	74.904 ± 0.067
0.0464159 eV - 0.1 eV	25.535 ± 0.048	76.010 ± 0.059
0.1 eV - 0.215443 eV	26.361 ± 0.057	77.928 ± 0.068
0.215443 eV - 0.464159 eV	26.615 ± 0.066	78.783 ± 0.077
0.464159 eV - 1 eV	26.504 ± 0.077	78.659 ± 0.090

1 eV - 2.15443 eV	26.636 ± 0.092	78.464 ± 0.108
2.15443 eV - 4.64159 eV	26.429 ± 0.110	78.242 ± 0.130
4.64159 eV - 10 eV	26.391 ± 0.133	77.930 ± 0.158
10 eV - 21.5443 eV	26.179 ± 0.161	77.898 ± 0.193
21.5443 eV - 46.4159 eV	25.977 ± 0.197	77.640 ± 0.239
46.4159 eV - 100 eV	26.074 ± 0.242	77.114 ± 0.295
100 eV - 215.443 eV	26.024 ± 0.299	77.236 ± 0.366
215.443 eV - 464.159 eV	25.495 ± 0.365	76.045 ± 0.456
464.159 eV - 1 keV	24.975 ± 0.448	75.716 ± 0.573
1 keV - 2.15443 keV	25.292 ± 0.533	75.065 ± 0.690
2.15443 keV - 4.64159 keV	26.457 ± 1.055	77.617 ± 1.358
4.64159 keV - 10 keV	24.618 ± 1.055	74.181 ± 1.395
10 keV - 21.5443 keV	26.220 ± 1.086	75.480 ± 1.410
21.5443 keV - 46.4159 keV	25.601 ± 1.052	74.608 ± 1.393
46.4159 keV - 100 keV	25.776 ± 0.963	75.155 ± 1.223
100 keV - 215.443 keV	26.794 ± 1.182	77.814 ± 1.422
215.443 keV - 464.159 keV	28.328 ± 1.081	82.288 ± 1.115
464.159 keV - 1 MeV	25.316 ± 4.975	72.152 ± 5.666

The bif extracted from the FLUKA simulations is reported in Table 17. Since when extracting neutron induced capture cross sections the data are often normalized at the 4.9 eV ^{197}Au resonance, it can be convenient to determine the ratio of the experimentally determined bif to the simulated one, after matching the two data sets in correspondence of the energy bin containing the 4.9 eV resonance. Therefore the experimental bif, in each energy region, is scaled by a factor equal to the ratio of value of the simulated bif at 4.9 eV to the value of the simulated bif at 4.9 eV. The obtained normalized bif is subsequently divided for the simulated bif. The result is reported in Fig 120, where the huge error bars highlight the poor statistics. A region of good agreement between the experimental and simulated bif is put in evidence through a grid around y = 1. It is important to underline that the FLUKA simulations used as a meter of comparison in this report were performed for the 2012 setup configuration (meaning a well defined concentration of ^{10}B in the moderator), therefore at low neutron energies a comparison is meaningful only for 2012 data.

Table 17. Simulated beam interception factor for 2 samples of different diameters.

Energy range	**B.I.F. for sample ⌀ = 1 cm [%]**	**B.I.F. for sample ⌀ = 2 cm [%]**
0.0215443 eV - 0.0464159 eV	23.104 ± 0.033	69.925 ± 0.036
0.0464159 eV - 0.1 eV	22.995 ± 0.028	69.562 ± 0.030
0.1 eV - 0.215443 eV	23.220 ± 0.042	69.853 ± 0.046
0.215443 eV - 0.464159 eV	22.352 ± 0.069	67.994 ± 0.078
0.464159 eV - 1 eV	22.256 ± 0.072	68.289 ± 0.080
1 eV - 2.15443 eV	23.420 ± 0.069	70.498 ± 0.075
2.15443 eV - 4.64159 eV	23.526 ± 0.068	70.295 ± 0.074
4.64159 eV - 10 eV	23.646 ± 0.068	70.703 ± 0.073
10 eV - 21.5443 eV	23.144 ± 0.069	69.804 ± 0.075
21.5443 eV - 46.4159 eV	23.636 ± 0.070	71.375 ± 0.075
46.4159 eV - 100 eV	23.100 ± 0.070	69.794 ± 0.076
100 eV - 215.443 eV	23.948 ± 0.067	71.673 ± 0.070
215.443 eV - 464.159 eV	23.724 ± 0.070	70.977 ± 0.075
464.159 eV - 1 keV	22.938 ± 0.066	69.512 ± 0.072
1 keV - 2.15443 keV	23.680 ± 0.065	71.039 ± 0.069
2.15443 keV - 4.64159 keV	23.528 ± 0.068	70.696 ± 0.073
4.64159 keV - 10 keV	22.882 ± 0.064	69.408 ± 0.070
10 keV - 21.5443 keV	23.104 ± 0.060	69.696 ± 0.065
21.5443 keV - 46.4159 keV	23.897 ± 0.061	71.185 ± 0.065
46.4159 keV - 100 keV	23.136 ± 0.051	69.949 ± 0.056
100 keV - 215.443 keV	23.327 ± 0.045	70.437 ± 0.048
215.443 keV - 464.159 keV	23.751 ± 0.035	71.208 ± 0.037
464.159 keV - 1 MeV	24.231 ± 0.026	72.540 ± 0.027

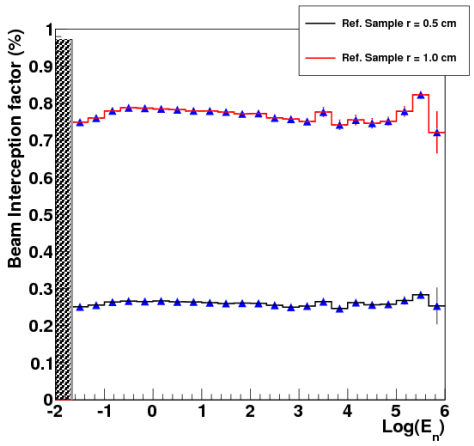

Figure 119. Experimental beam interception factor for different sample radii.

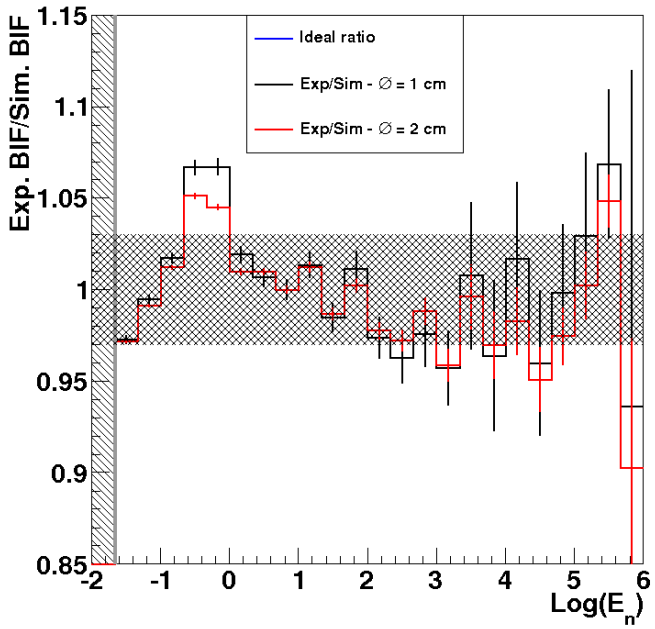

Figure 120. Ratio between the experimental and simulated bif (after renormalization of the experimental bif).

5.3 2011

In 2011 two separate measurements were taken. The detector was positioned at the same TOF distance as in 2010. On the other side, the ^{10}B concentration in borated water was changed.

5.3.1 15^{th} March 2011

In a first moment the PKUP was not working, therefore the number of allocated protons is unknown.

Table 18. Details of the measurement performed the 15^{th} March 2011.

Configuration	TOF distance of 183.74 m
Runs	1121, 11622, 11623, 11624, 11625, 11626,11627
Protons	No info available
Converter thickness	2 μm
Mesh Voltage	330 V
Drift Voltage	400 V

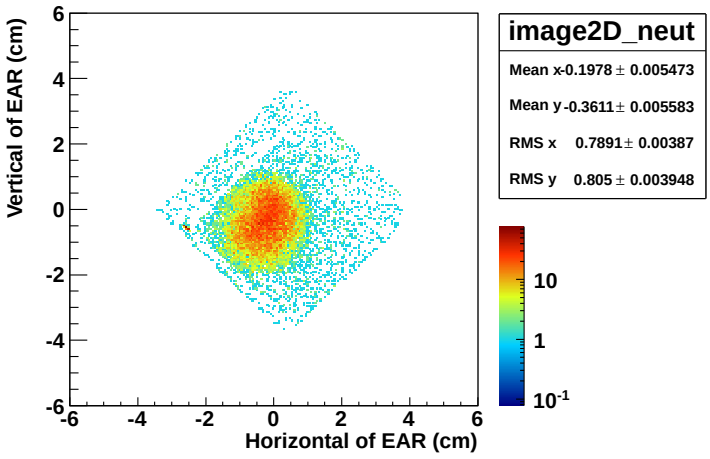

Figure 121. Beam image (μMegas detector seen in the reference system of the EAR.).

The next pictures show the beam profiles obtained by considering all neutron energies. As usual, a simple Gaussian fit is shown.

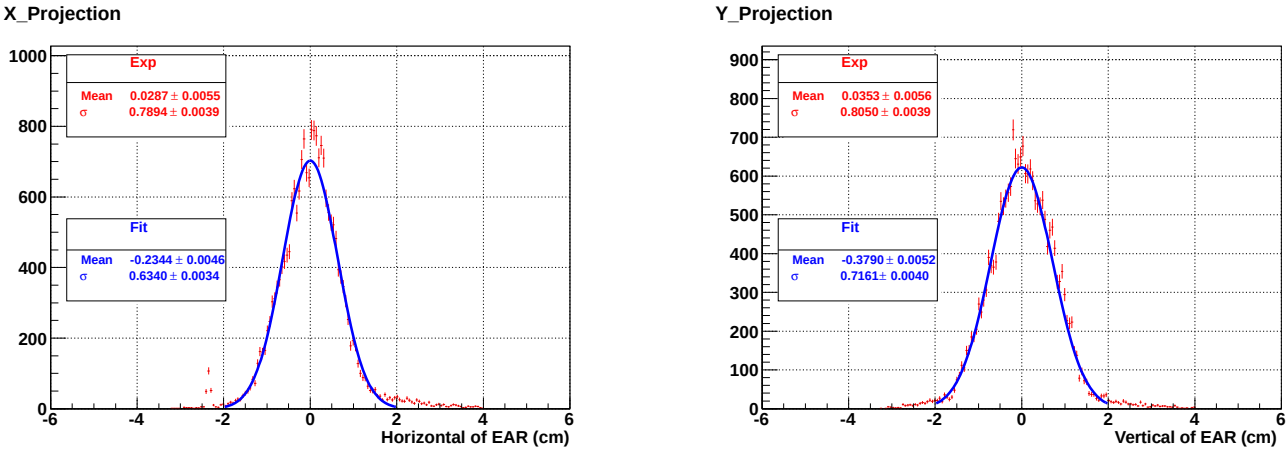

Figure 122. Beam profile obtained by considering all neutron energies. The left panel refers to the X axis, while the right one concerns the Y axis.

5.3.2 15^{th} - 16^{th} March

Table 19. Details of the measurement performed the period 15^{th} - 16^{th} March 2011.

Configuration	TOF distance of 183.74 m
Runs	11629, 11630, 11631, 11632, 11633, 11634, 11635, 11636, 11637, 11638, 11639, 11640 , 11641, 11642 , 11643
Protons	1.06448e+17
Converter thickness	2 μm
Mesh Voltage	330 V
Drift Voltage	400 V

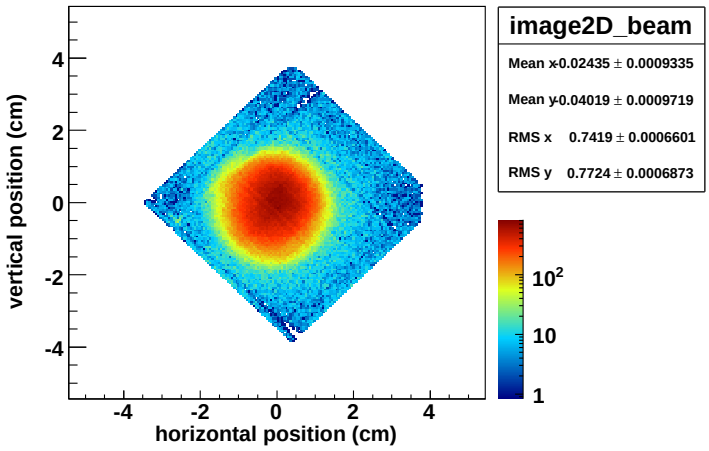

Figure 123. Beam image (μMegas detector seen in the reference system of the EAR.).

As done for 2010 data, before reporting the analysis, the beam profile along the X and Y axis reconstructed by considering all neutron energies is shown (see Fig 124). In order to better see the shape of the beam profile, no fit is superimposed.

The analysis of the beam profile follows. Experimental data were fitted with a bidimensional Gaussian function. Because of low statistics the analysis was carried on by considering only 1 bin per decade.

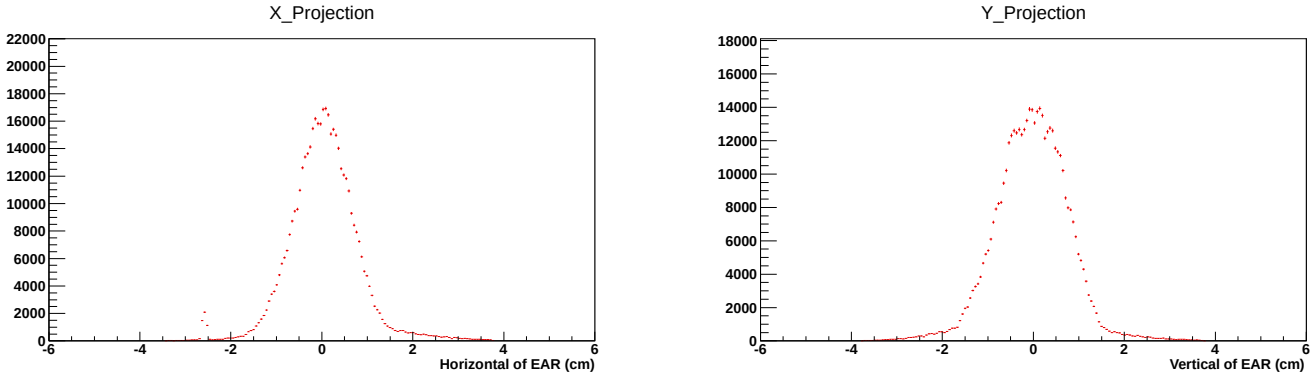

Figure 124. Beam profile along the X axis. All neutron energies are considered. The left panel refers to results obtained with the original routines, while the right one concerns the modified routines.

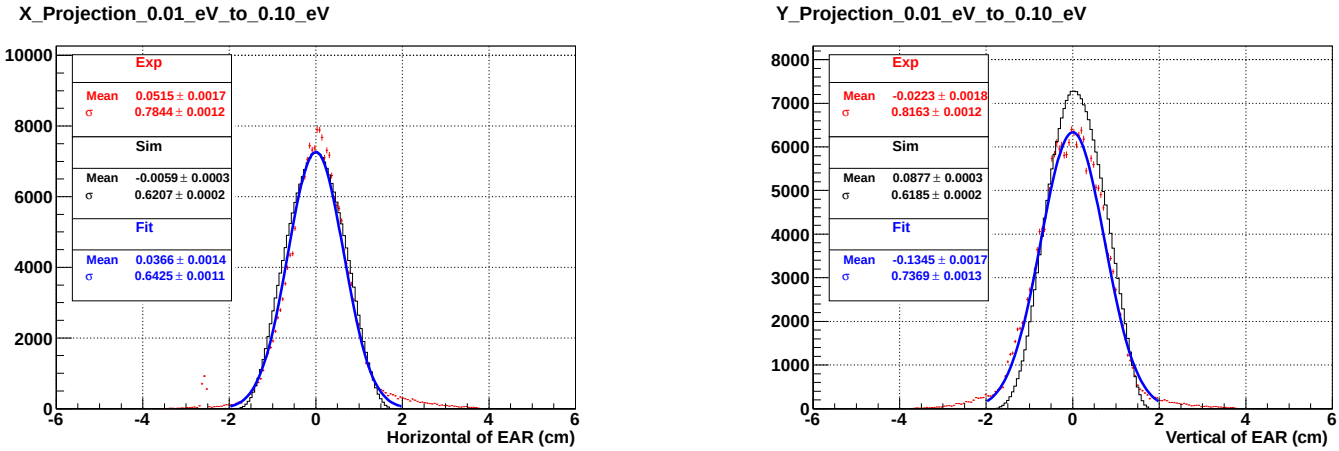

Figure 125. Beam profile in the energy range between 0.01 eV and 0.1 eV are considered. The left panel refers to the X axis, while the right one concerns the Y axis.

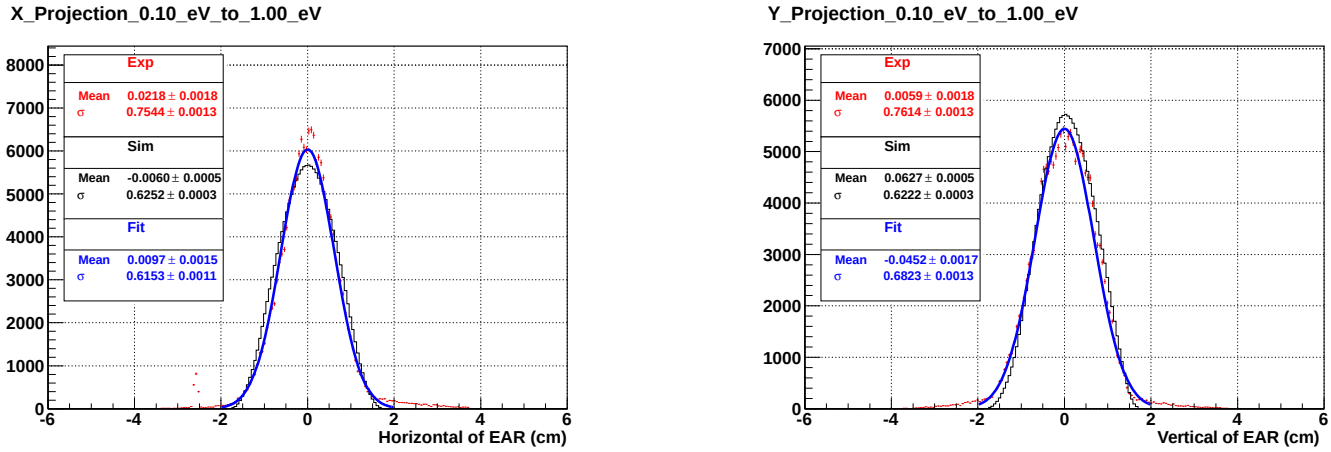

Figure 126. Beam profile in the energy range between 0.1 eV and 1 eV are considered. The left panel refers to the X axis, while the right one concerns the Y axis.

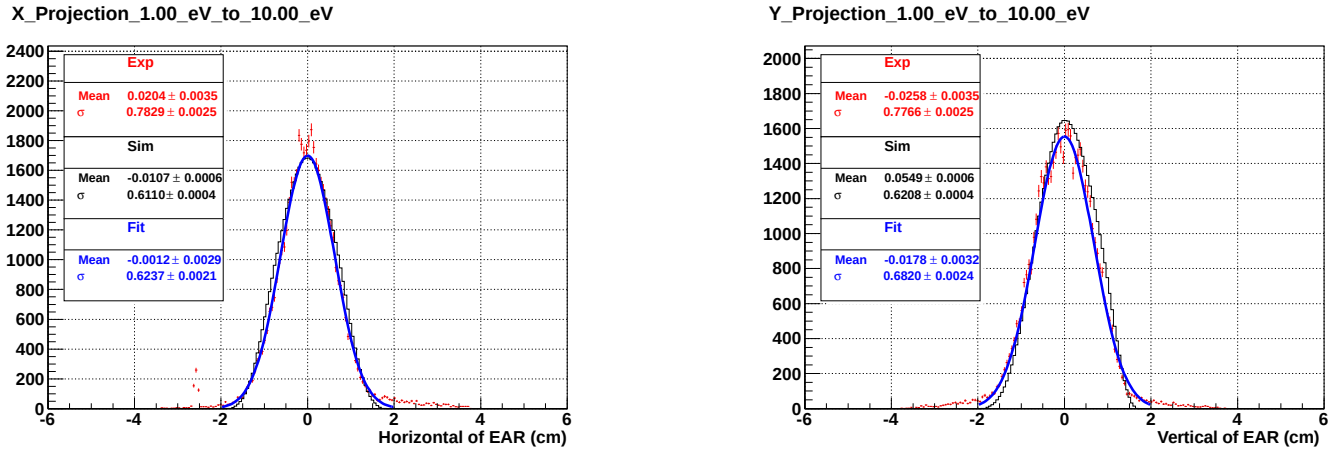

Figure 127. Beam profile in the energy range between 1 eV and 10 eV are considered. The left panel refers to the X axis, while the right one concerns the Y axis.

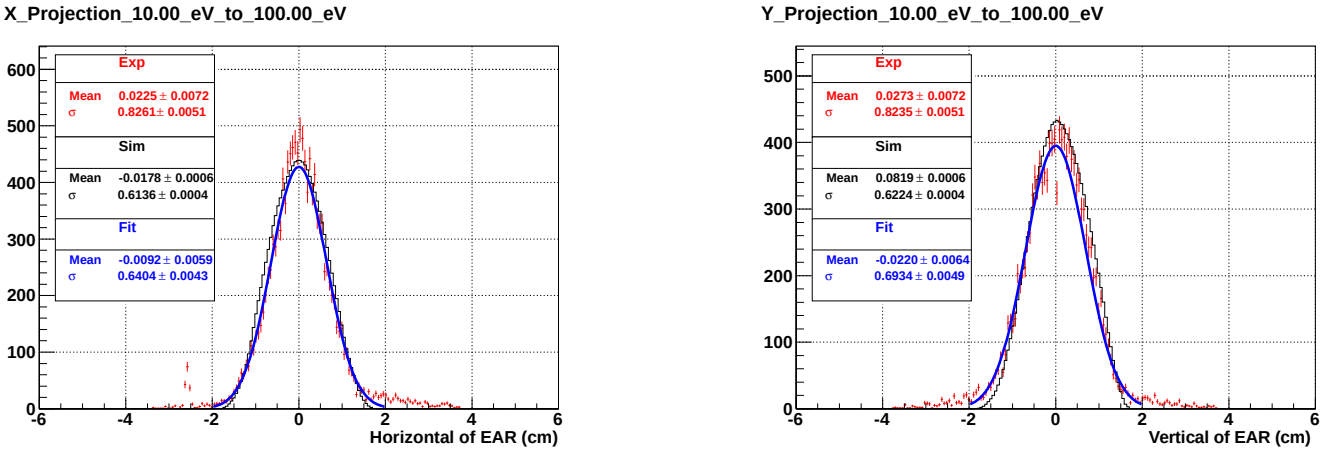

Figure 128. Beam profile in the energy range between 10 eV and 100 eV are considered. The left panel refers to the X axis, while the right one concerns the Y axis.

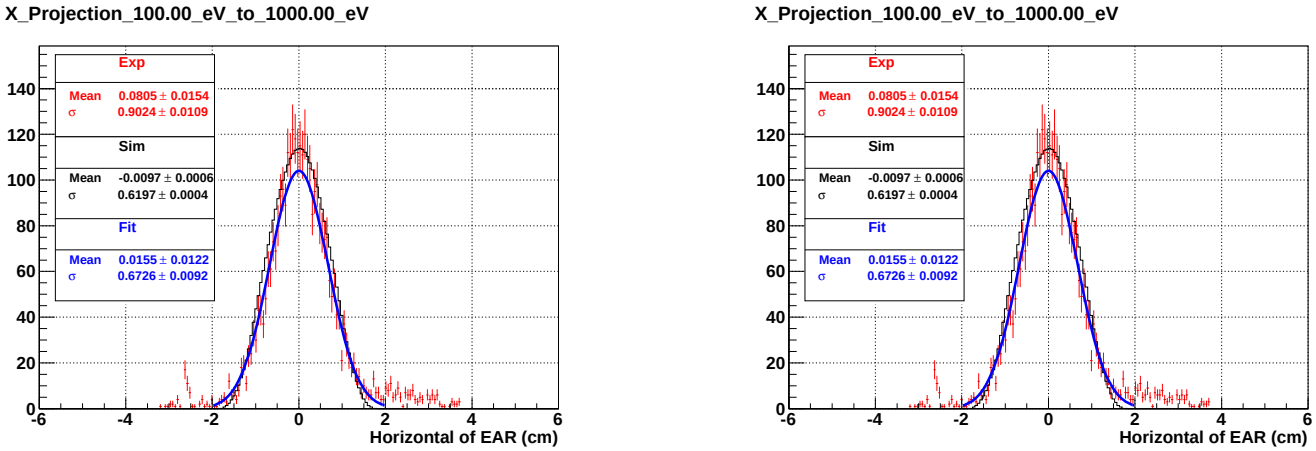

Figure 129. Beam profile in the energy range between 100 eV and 1 keV are considered. The left panel refers to the X axis, while the right one concerns the Y axis.

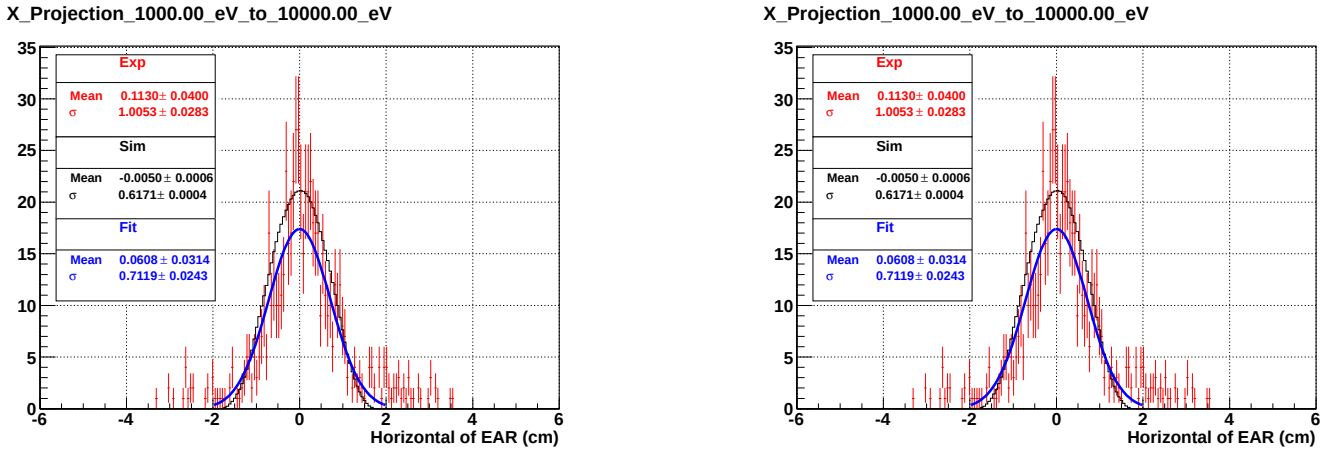

Figure 130. Beam profile in the energy range between 1 keV and 10 keV are considered. The left panel refers to the X axis, while the right one concerns the Y axis.

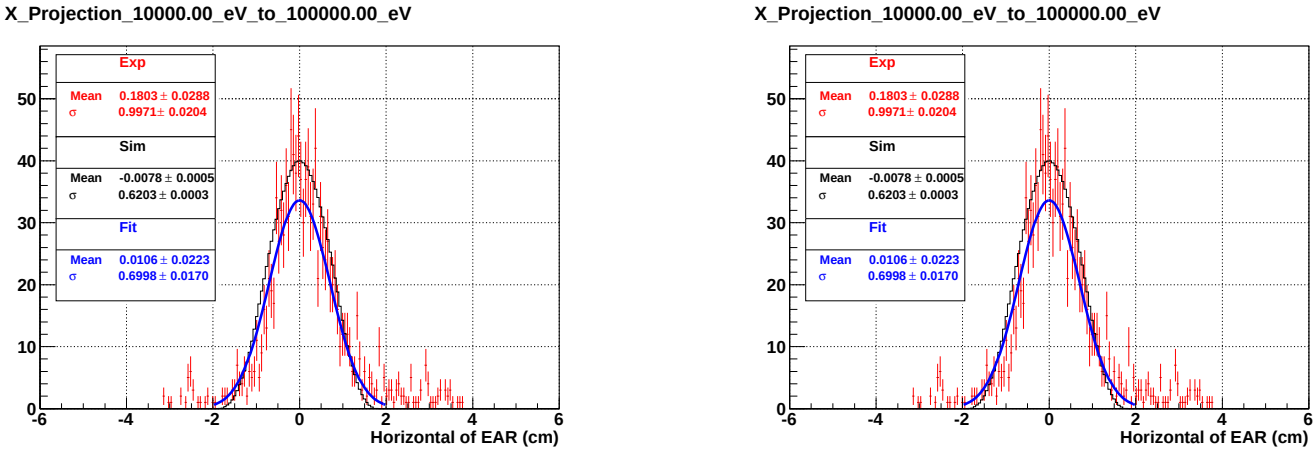

Figure 131. Beam profile in the energy range between 10 keV and 100 keV are considered. The left panel refers to the X axis, while the right one concerns the Y axis.

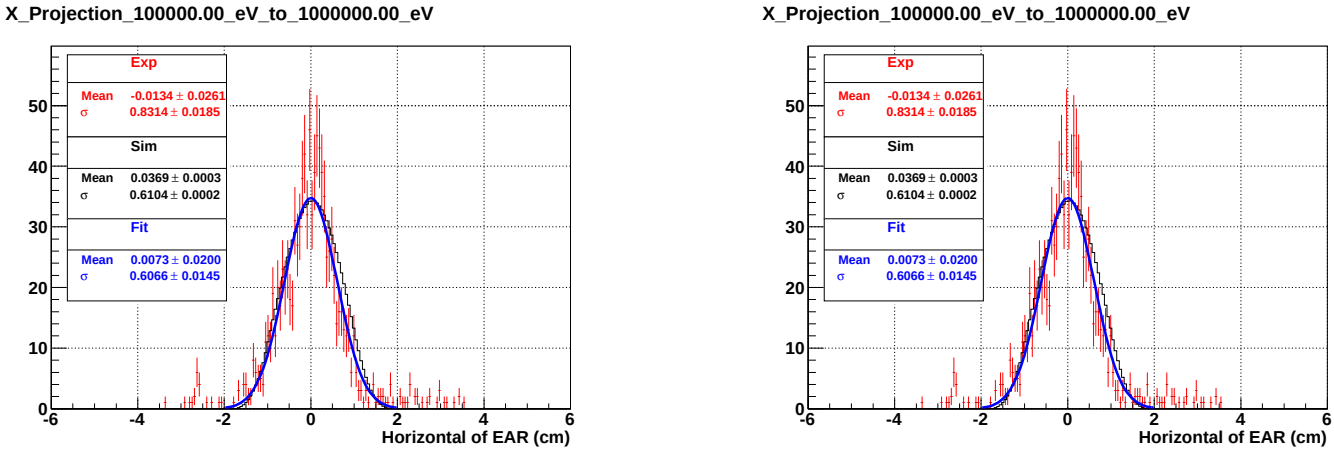

Figure 132. Beam profile in the energy range between 100 keV and 1 MeV are considered. The left panel refers to the X axis, while the right one concerns the Y axis.

Table 20 reports the widths of the beam profile obtained by the fit as a function of the neutron energy, while in Fig. 133 the corresponding plots are shown.

Table 20. Fit parameters. A 2D Gaussian fit was considered.

Energy range	σ_x **[cm]**	$\delta\sigma_x$ **[cm]**	σ_y **[cm]**	$\delta\sigma_y$ **[cm]**	χ^2
0.01 eV - 10 eV	0.6425	0.0011	0.7369	0.0013	6.40
0.1 eV - 1 eV	0.6152	0.0011	0.6823	0.0013	5.13
1 eV - 10 eV	0.6237	0.0021	0.6820	0.0024	1.77
10 eV - 100 eV	0.6404	0.0043	0.6934	0.0048	0.85
100 eV - 1 keV	0.6726	0.0092	0.7114	0.0100	0.36
1 keV - 10 keV	0.7119	0.0243	0.7826	0.0283	0.09
10 keV - 100 keV	0.6998	0.0170	0.7475	0.0189	0.14
100 keV - 1 MeV	0.6065	0.0145	0.6585	0.0164	0.13

Table 22 reports the values of the bif experimentally determined and in Fig. 133 the corresponding plots are shown. Tab 22 lists the bif obtained from FLUKA simulations. We underline again that the FLUKA simulations used as a meter of comparison in this report are tuned on the 2012 facility characteristics, and therefore at low neutron energies a comparison between simulated and experimental data is not conclusive.

Table 21. Beam interception factor calculated for 2 samples of different diameters.

Energy range	**B.I.F. for sample ⌀ = 1 cm [%]**	**B.I.F. for sample ⌀ = 2 cm [%]**
0.01 eV - 0.1 eV	22.990 ± 0.020	69.646 ± 0.021
0.1 eV - 1 eV	22.845 ± 0.032	69.149 ± 0.035
1 eV - 10 eV	23.532 ± 0.040	70.499 ± 0.043
10 eV - 100 eV	23.291 ± 0.040	70.317 ± 0.043
100 eV - 1 keV	23.531 ± 0.039	70.713 ± 0.042
1 keV - 10 keV	23.358 ± 0.038	70.372 ± 0.041
10 keV - 100 keV	23.351 ± 0.033	70.238 ± 0.035
100 keV - 1 MeV	23.938 ± 0.019	71.796 ± 0.020

Table 22. Beam interception factor calculated for 2 samples of different diameters.

Energy range	**B.I.F. for sample ⌀ = 1 cm [%]**	**B.I.F. for sample ⌀ = 2 cm [%]**
0.01 eV - 0.1 eV	24.471 ± 0.097	67.877 ± 0.111
0.1 eV - 1 eV	26.200 ± 0.110	71.882 ± 0.120
1 eV - 10 eV	26.401 ± 0.208	72.186 ± 0.226
10 eV - 100 eV	26.459 ± 0.412	71.291 ± 0.046
100 eV - 1 keV	25.595 ± 0.814	70.653 ± 0.094
1 keV - 10 keV	24.272 ± 1.946	69.708 ± 2.428
10 keV - 100 keV	25.202 ± 1.421	70.344 ± 1.726
100 keV - 1 MeV	29.934 ± 1.544	75.329 ± 1.603

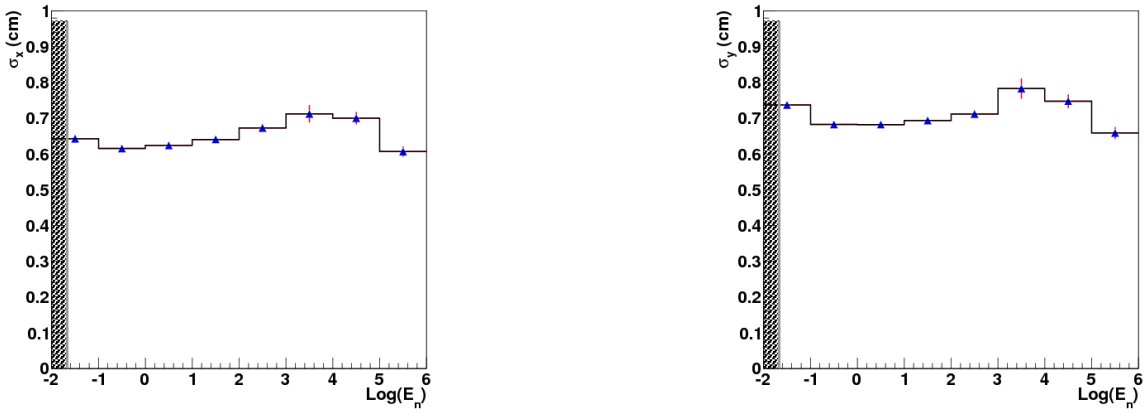

Figure 133. Relation between the Gaussian width obtained by fitting the beam profiles and the neutron energy.

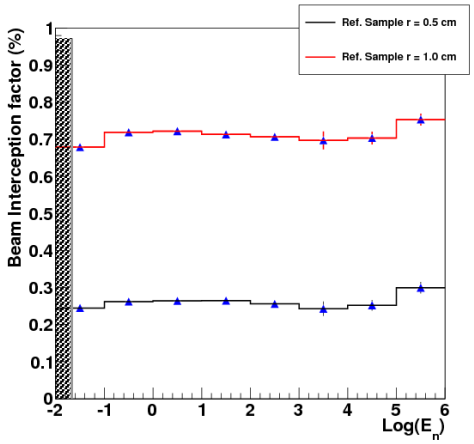

Figure 134. Beam interception factor for different sample radii.

5.4 2012

5.4.1 24^{th} March 2012

Table 23. Details of the measurement performed on 24^{th} March 2012.

Configuration	TOF distance of 183.74 m
Runs	13518, 13519, 13520, 13521, 13522, 13523, 13524, 13525, 13526, 13527, 13529 , 13530, 13531 , 13532, 13533
Protons	2.60463e+17
Converter thickness	2 μm
Mesh Voltage	330 V
Drift Voltage	400 V

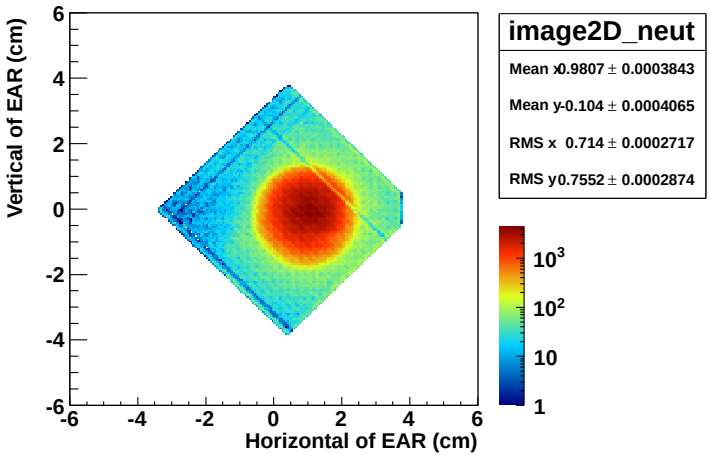

Figure 135. Beam image (μMegas detector seen in the reference system of the EAR.).

Again, the following pictures show the comparison between the beam profile for different neutron energy ranges and simulations performed by the FLUKA [19] group in n_TOF. The fit is superimposed. Statistical panels report the displacement of the beam profiles along the reference axis, but all experimental curves are shifted so that their peak position coincides with that of the simulated ones they are confronted to.

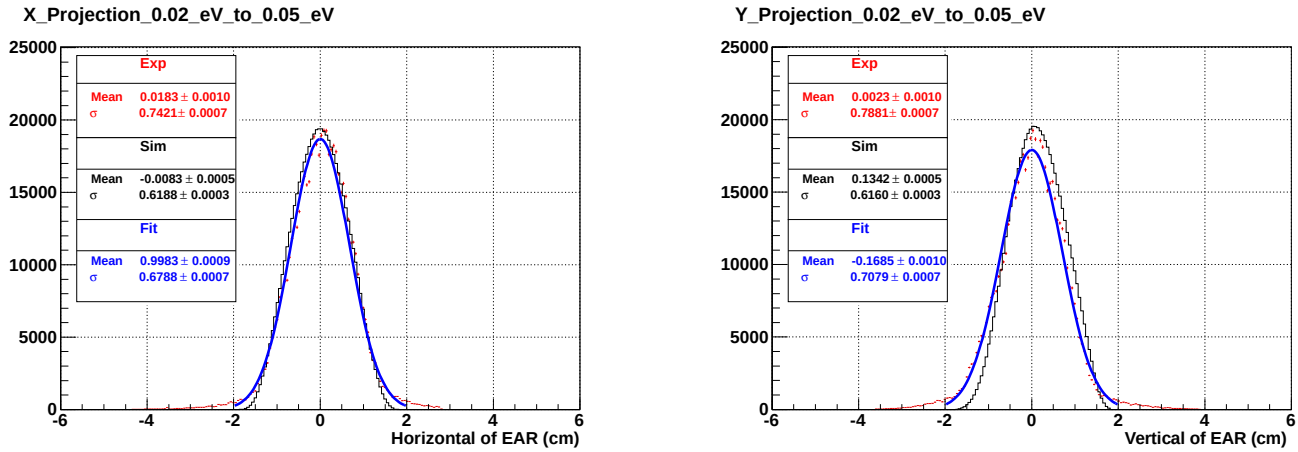

Figure 136. Beam profile in the energy range between 0.025 eV and 0.05 eV.

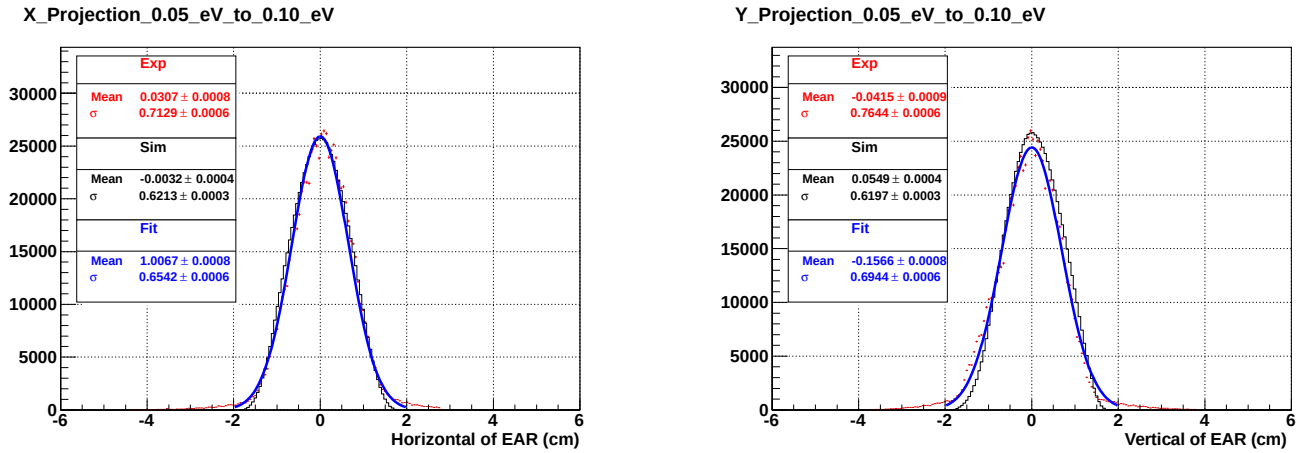

Figure 137. Beam profile in the energy range between 0.05 eV and 0.1 eV.

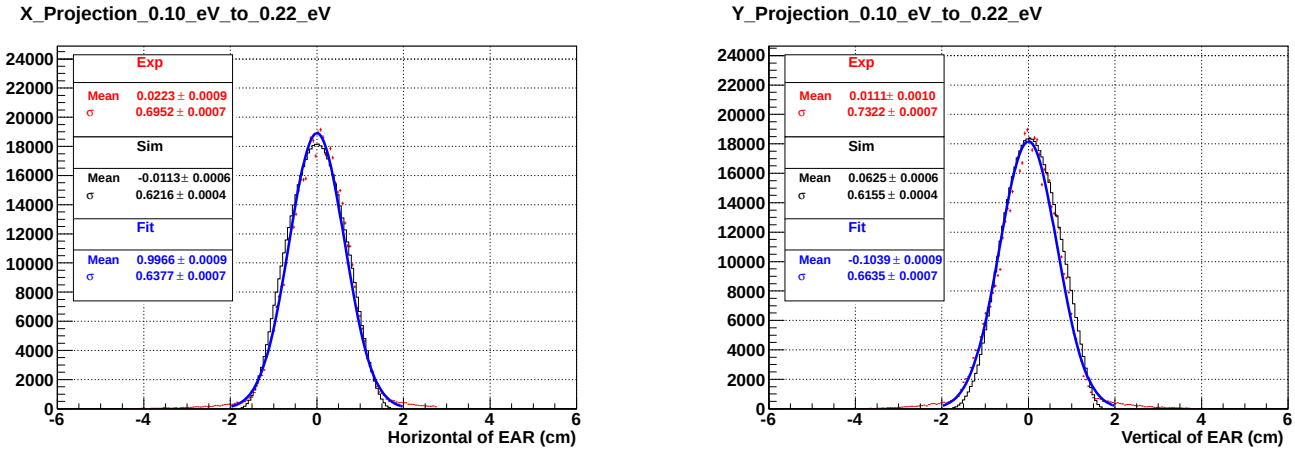

Figure 138. Beam profile in the energy range between 0.1 eV and 0.22 eV.

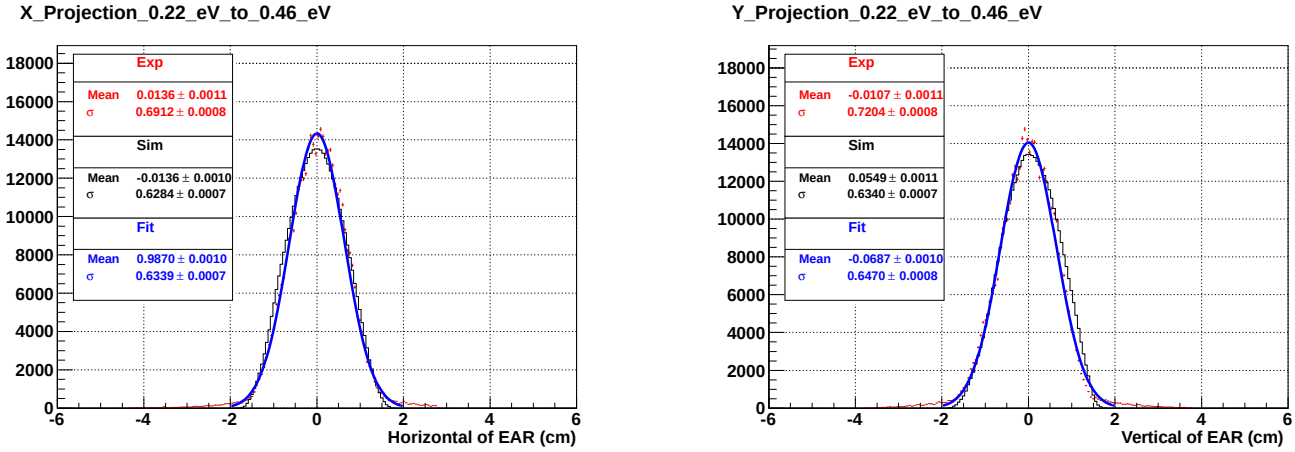

Figure 139. Beam profile in the energy range between 0.22 eV and 0.46 eV.

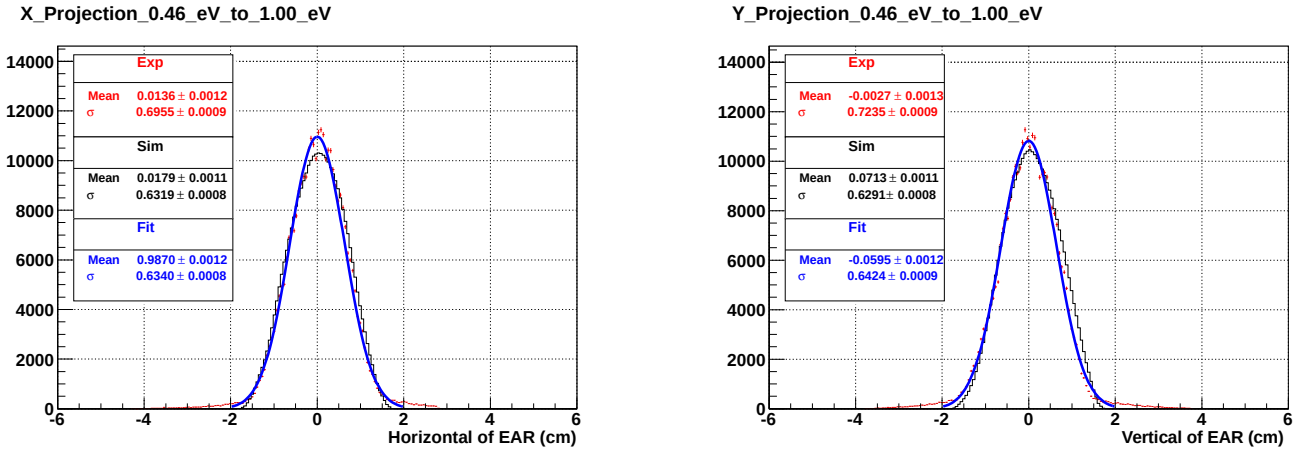

Figure 140. Beam profile in the energy range between 0.46 eV and 1 eV.

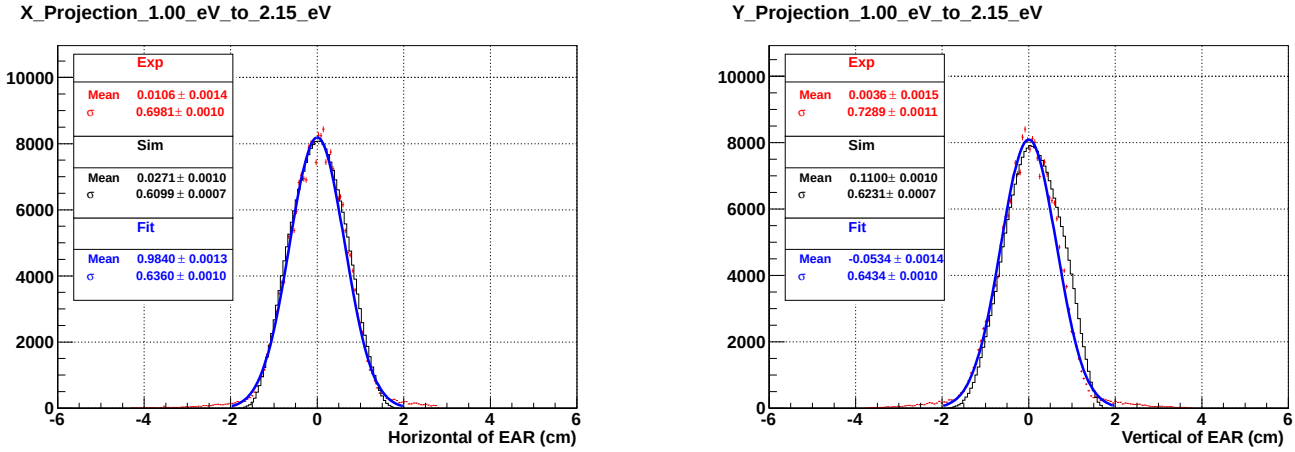

Figure 141. Beam profile in the energy range between 1 eV and 2.15 eV.

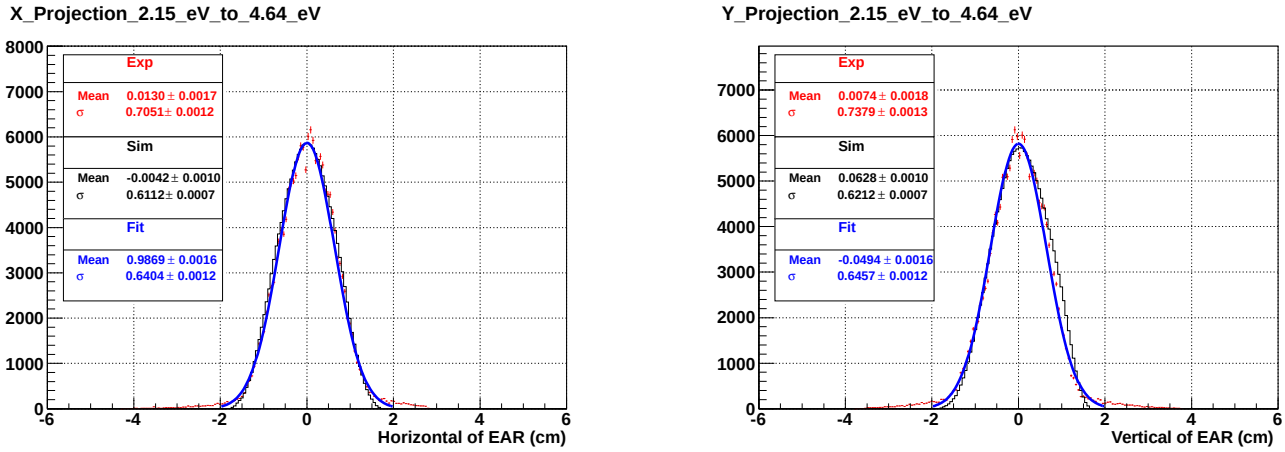

Figure 142. Beam profile in the energy range between 2.15 eV and 4.64 eV.

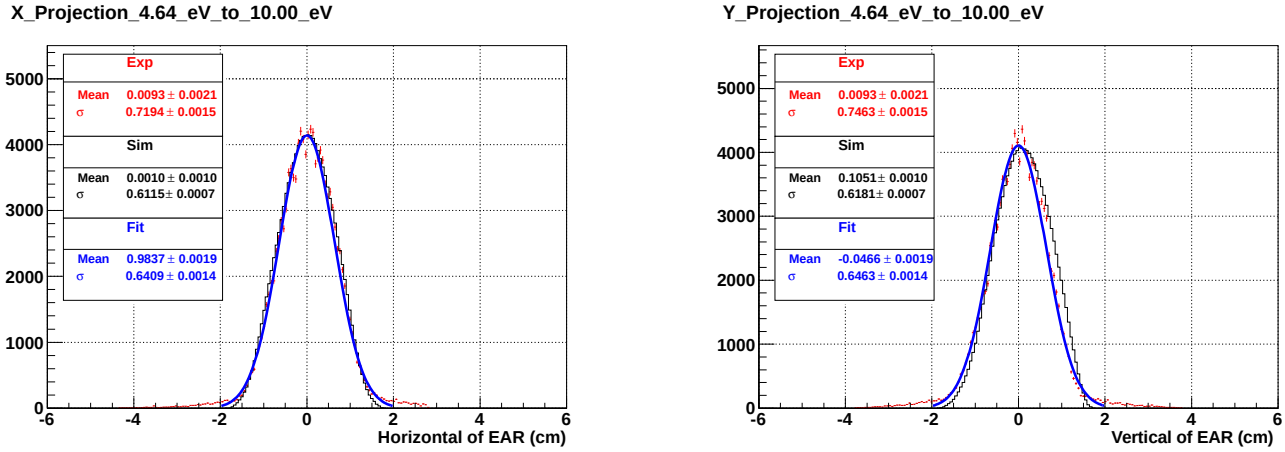

Figure 143. Beam profile in the energy range between 4.64 eV and 10 eV.

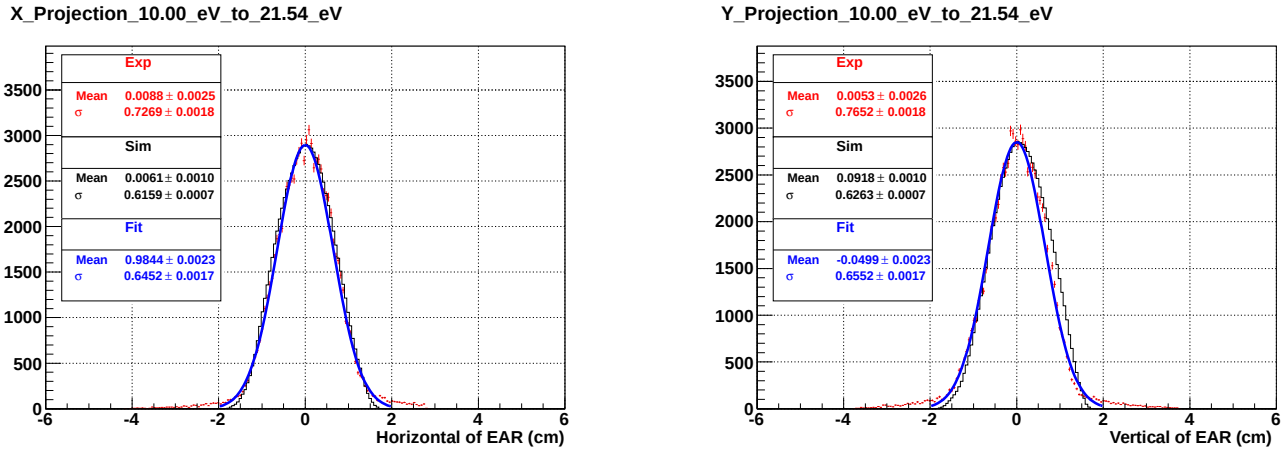

Figure 144. Beam profile in the energy range between 10 eV and 21.54 eV.

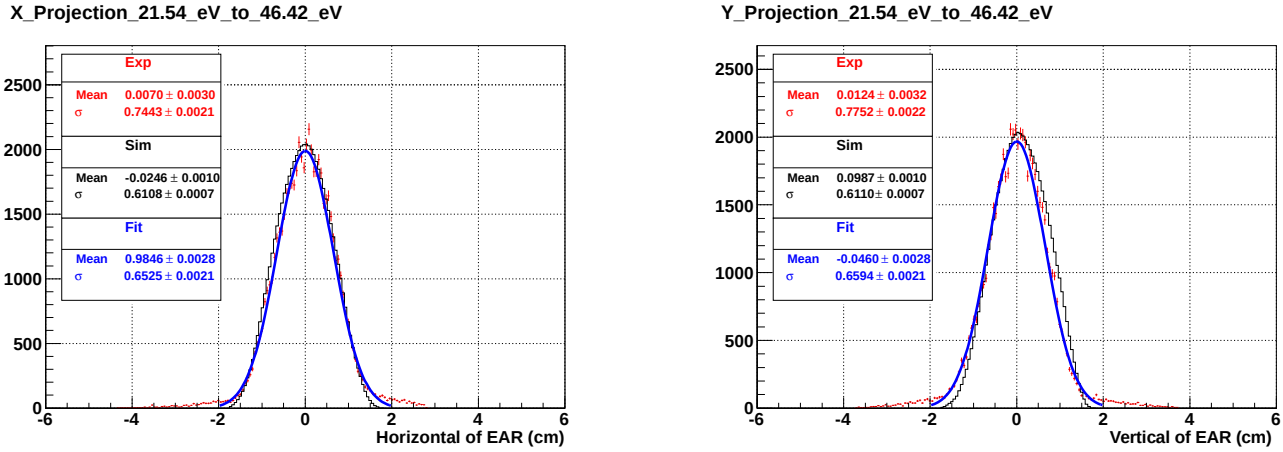

Figure 145. Beam profile in the energy range between 21.54 eV and 46.42 eV.

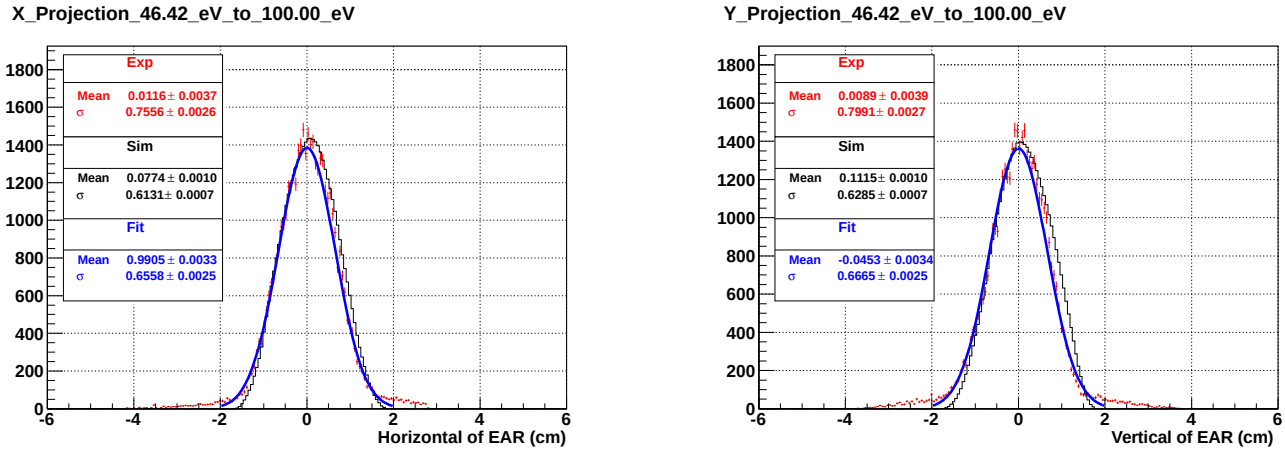

Figure 146. Beam profile in the energy range between 46.42 eV and 100 eV.

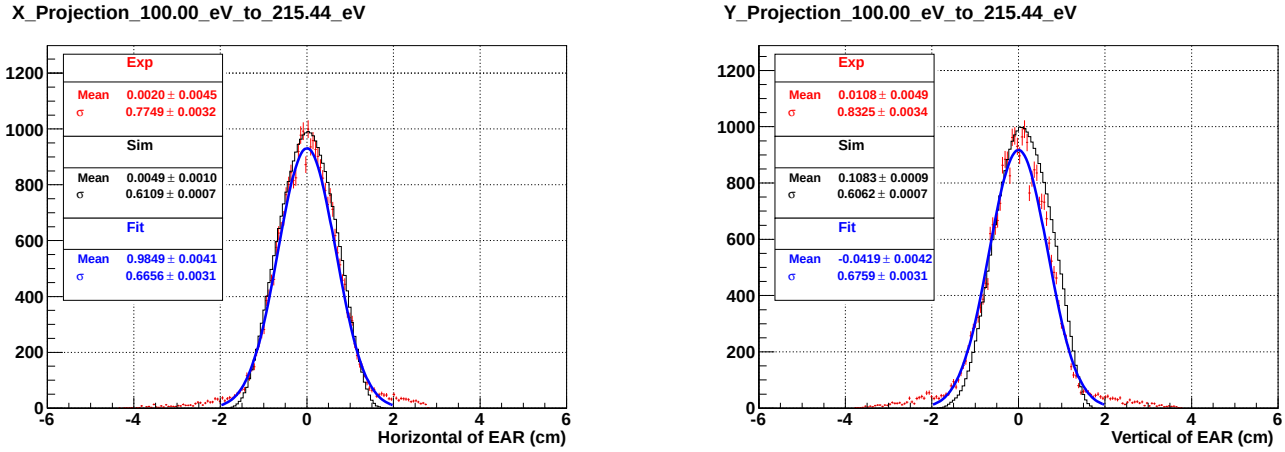

Figure 147. Beam profile in the energy range between 100 eV and 215.44 eV.

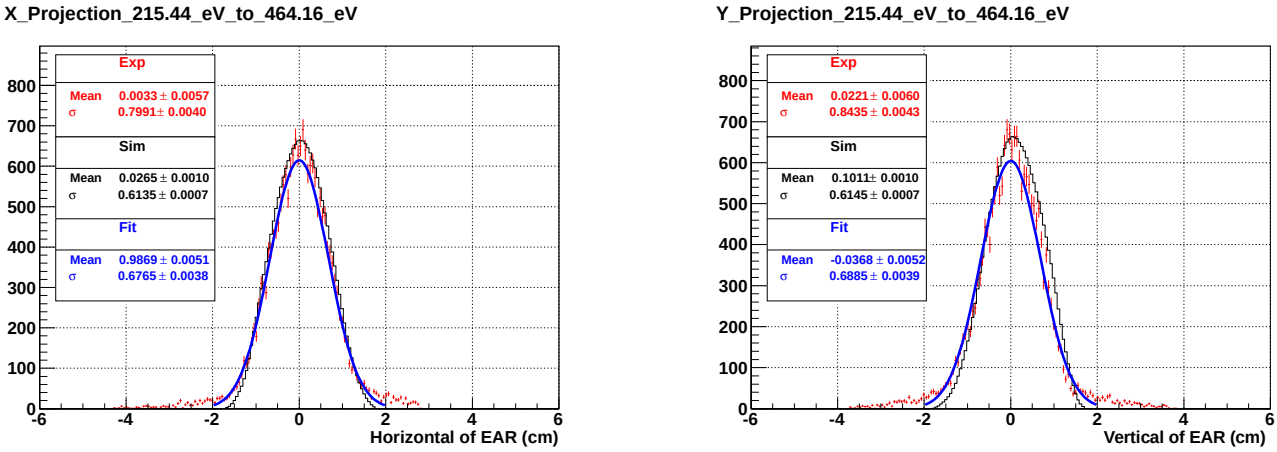

Figure 148. Beam profile in the energy range between 215.44 eV and 464.16 eV.

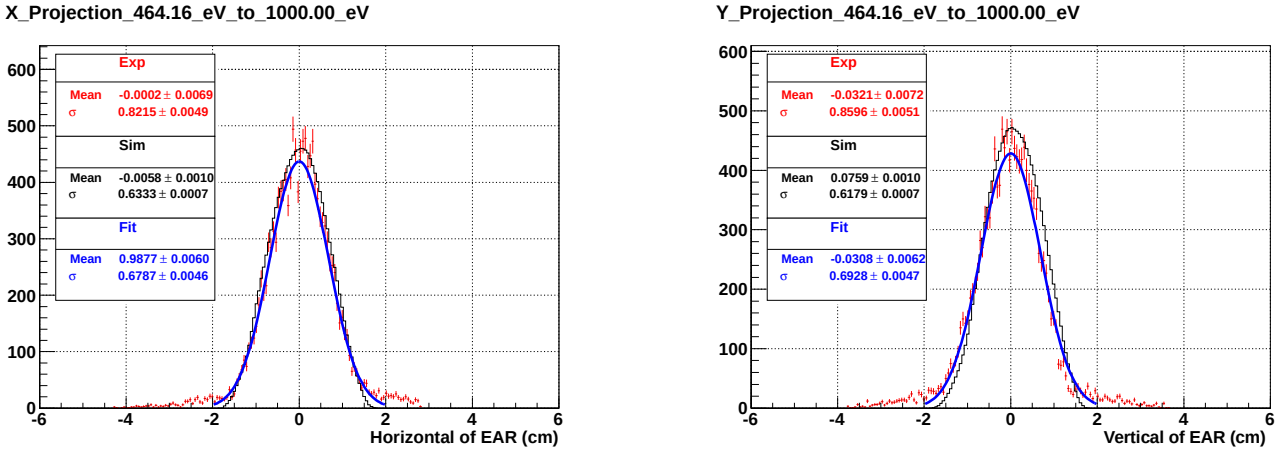

Figure 149. Beam profile in the energy range between 464.16 eV and 1 keV.

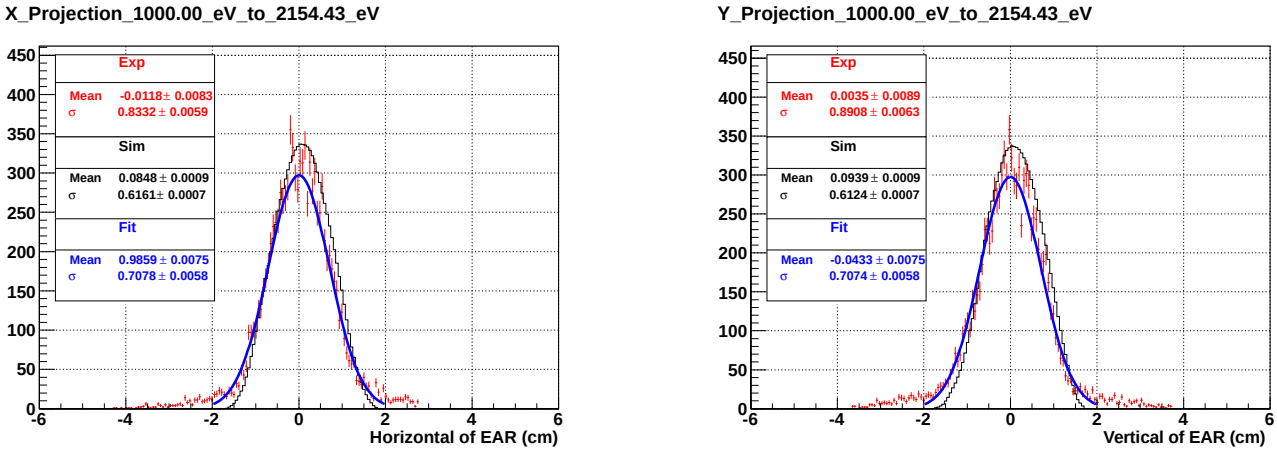

Figure 150. Beam profile in the energy range between 1 keV and 2.15 keV.

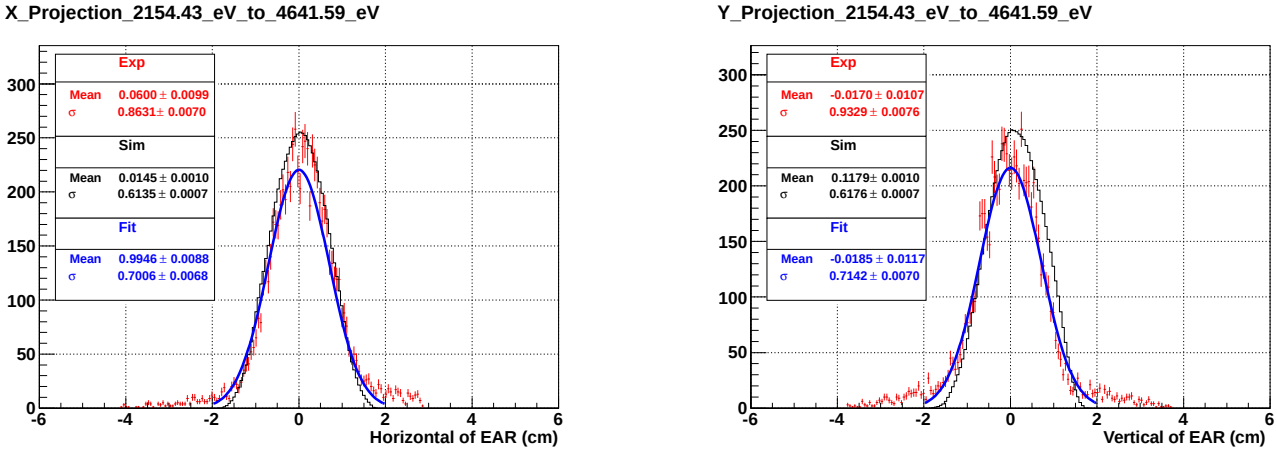

Figure 151. Beam profile in the energy range between 2.15 keV and 4.64 keV.

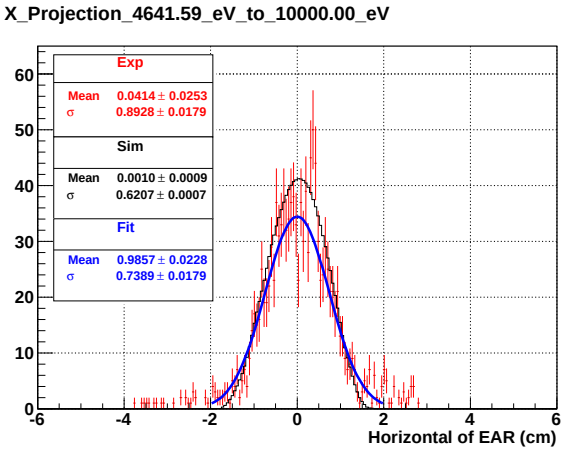

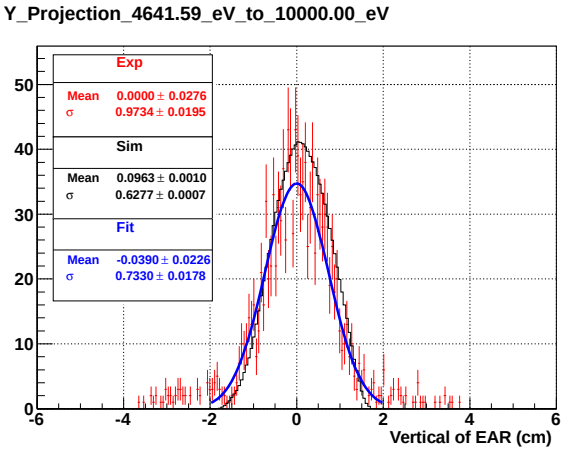

Figure 152. Beam profile in the energy range between 4.64 keV and 10 keV.

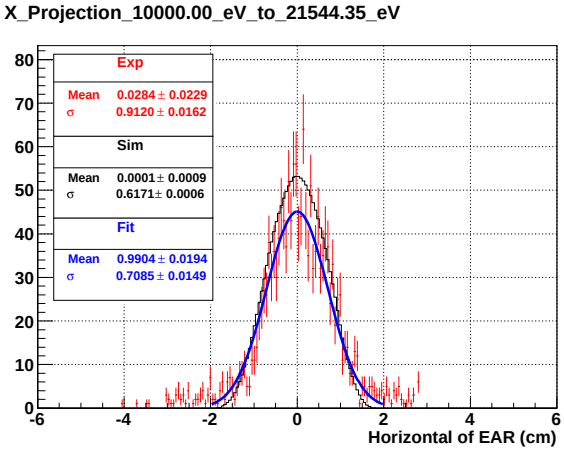

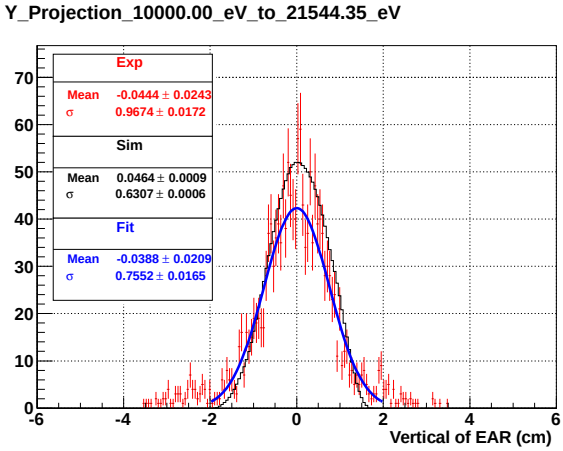

Figure 153. Beam profile in the energy range between 10 keV and 21.5 keV.

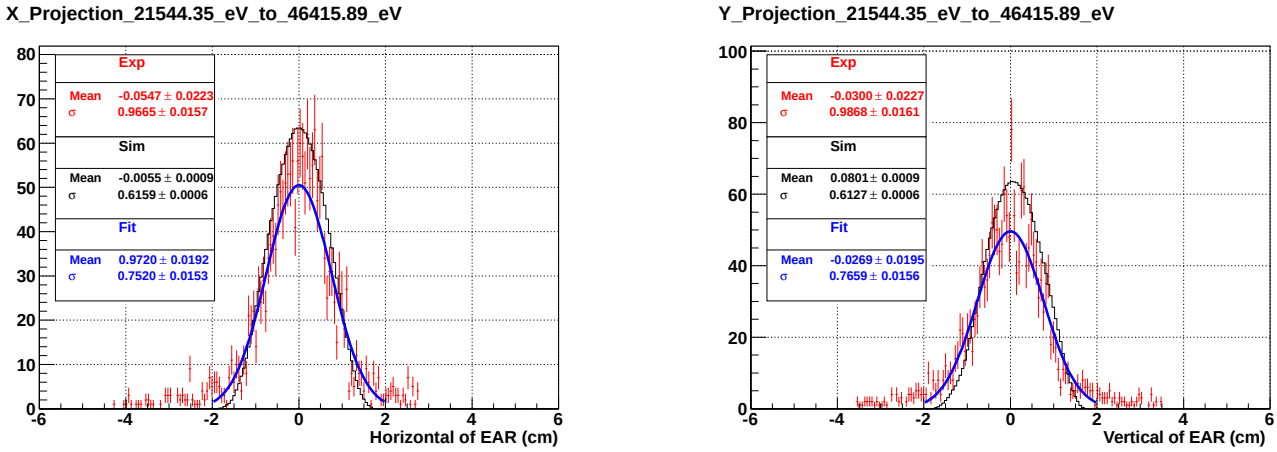

Figure 154. Beam profile in the energy range between 21.5 keV and 46.4 keV.

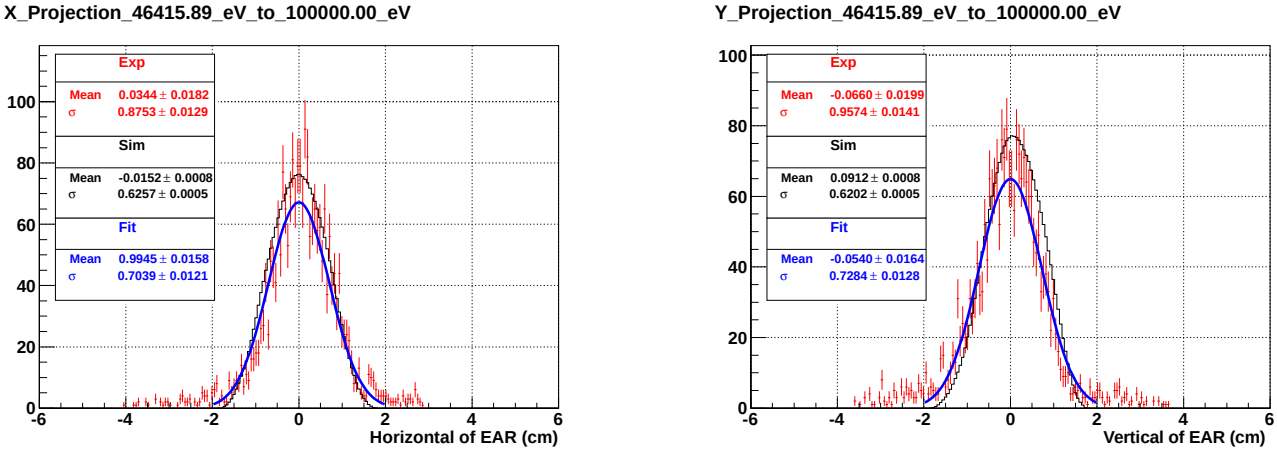

Figure 155. Beam profile in the energy range between 46.4 keV and 100 keV.

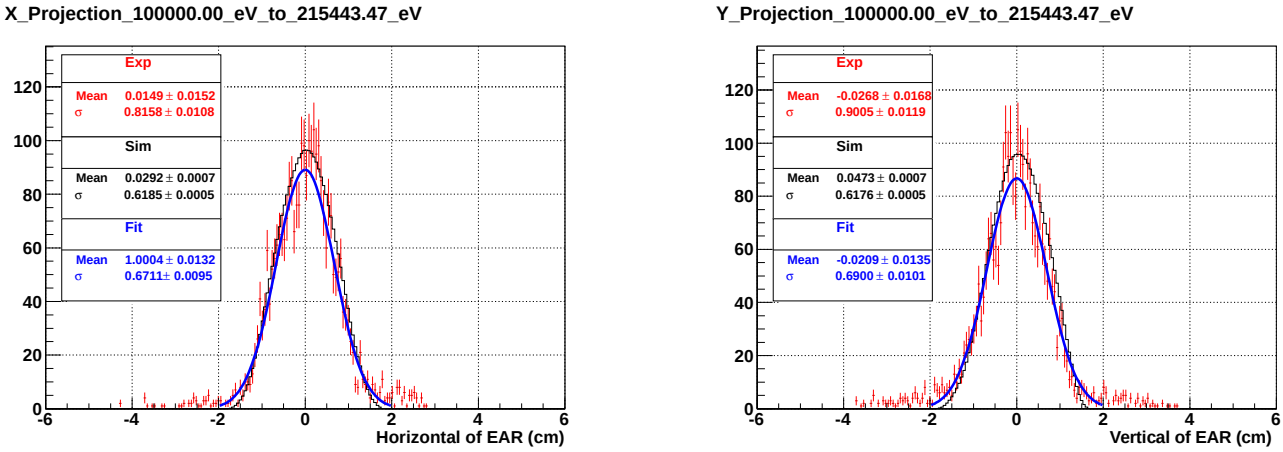

Figure 156. Beam profile in the energy range between 100 keV and 215.4 keV.

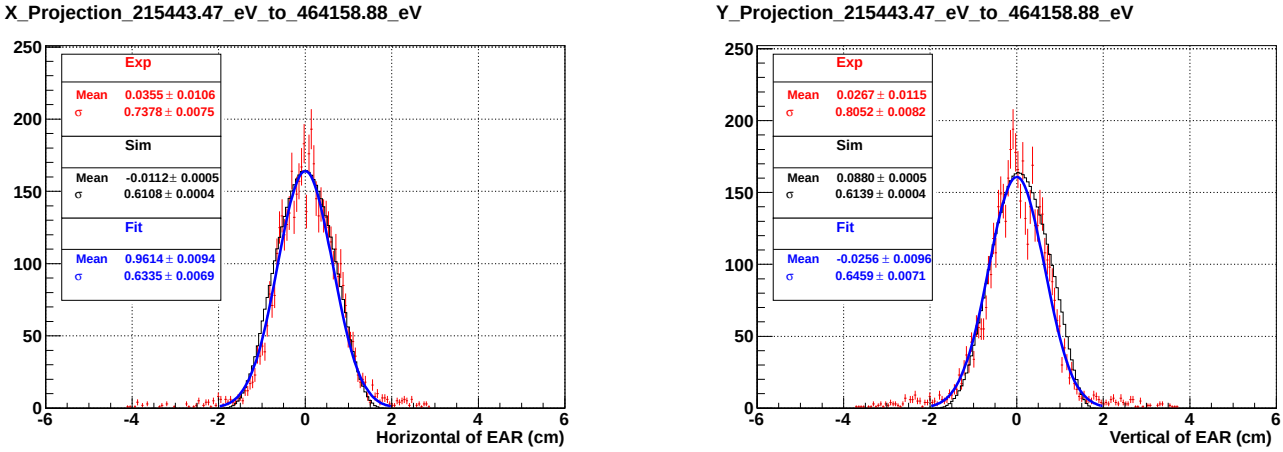

Figure 157. Beam profile in the energy range between 215.4 keV and 464.15 keV.

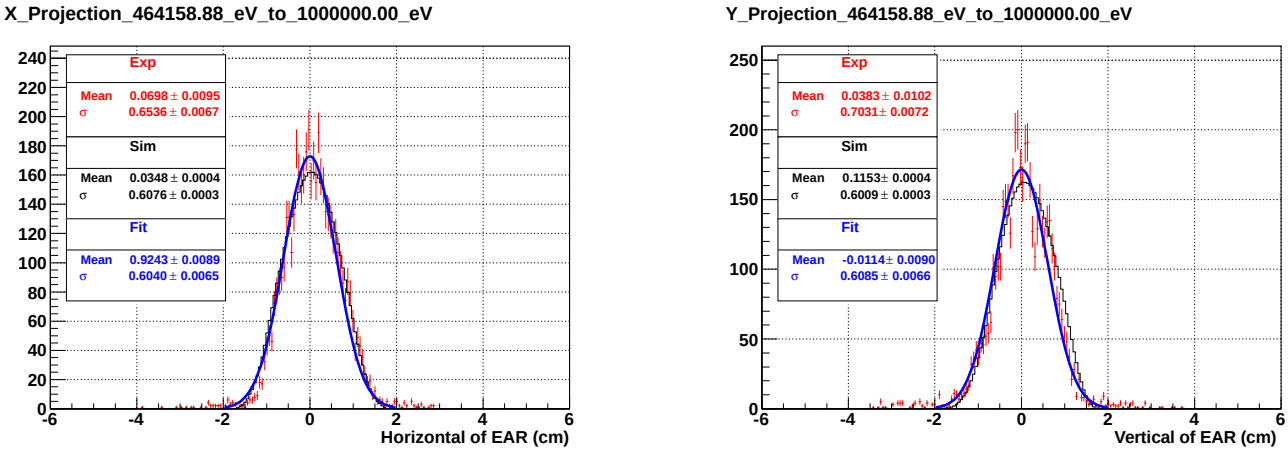

Figure 158. Beam profile in the energy range between 464.15 keV and 1 MeV.

Table 24 reports the widths of the beam profile obtained by the fit as a function of the neutron energy, while in Fig. 159 the corresponding plots are shown.

Table 24. Fit parameters. A 2D Gaussian fit was considered.

Energy range	σ_x **[cm]**	$\delta\sigma_x$ **[cm]**	σ_y **[cm]**	$\delta\sigma_y$ **[cm]**	χ^2
0.0215443 eV - 0.0464159 eV	0.6788	0.0007	0.7079	0.0007	7.38
0.0464159 eV - 0.1 eV	0.6542	0.0006	0.6944	0.0006	10.10
0.1 eV - 0.215443 eV	0.6377	0.0007	0.6635	0.0007	7.73
0.215443 eV - 0.464159 eV	0.6339	0.0007	0.6470	0.0008	6.74
0.464159 eV - 1 eV	0.6340	0.0008	0.6424	0.0009	5.51
1 eV - 2.15443 eV	0.6360	0.0010	0.6434	0.0010	4.32
2.15443 eV - 4.64159 eV	0.6404	0.0012	0.6457	0.0012	3.68
4.64159 eV - 10 eV	0.6409	0.0014	0.6462	0.0014	3.16
10 eV - 21.5443 eV	0.6452	0.0017	0.6552	0.0017	2.46
21.5443 eV - 46.4159 eV	0.6525	0.0021	0.6594	0.0021	1.99
46.4159 eV - 100 eV	0.6558	0.0025	0.6665	0.0025	1.64
100 eV - 215.443 eV	0.6656	0.0031	0.6759	0.0031	1.31
215.443 eV - 464.159 eV	0.6765	0.0038	0.6885	0.0039	1.07
464.159 eV - 1 keV	0.6787	0.0046	0.6928	0.0047	0.87
1 keV - 2.15443 keV	0.7078	0.0058	0.7074	0.0058	0.81
2.15443 keV - 4.64159 keV	0.7006	0.0068	0.7142	0.0070	0.65
4.64159 keV - 10 keV	0.7389	0.0179	0.7330	0.0178	0.16
10 keV - 21.5443 keV	0.7085	0.0149	0.7552	0.0165	0.19
21.5443 keV - 46.4159 keV	0.7520	0.0153	0.7659	0.0156	0.22
46.4159 keV - 100 keV	0.7039	0.0121	0.7284	0.0128	0.25

100 keV - 215.443 keV	0.6711	0.0095	0.6900	0.0101	0.30
215.443 keV - 464.159 keV	0.6335	0.0069	0.6459	0.0071	0.45
464.159 keV - 1 MeV	0.6040	0.0065	0.6085	0.0066	0.47

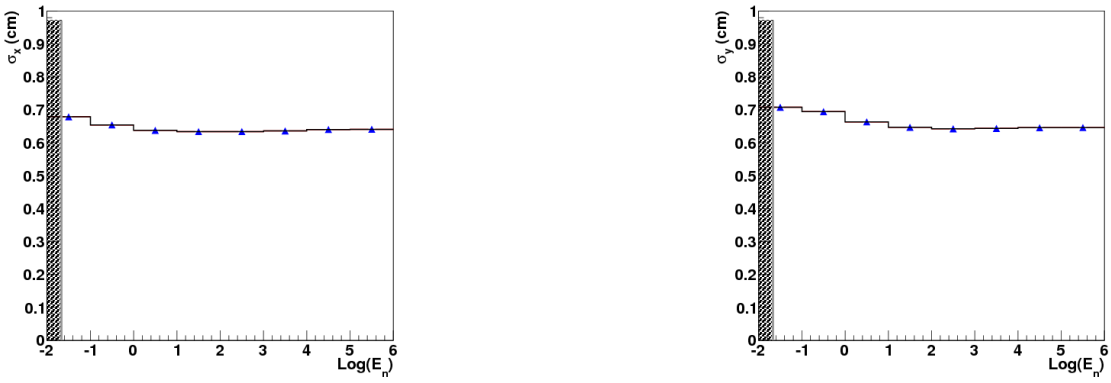

Figure 159. Relation between the Gaussian width obtained by fitting the beam profiles and the neutron energy.

Table 25 reports the beam interception factor experimentally obtained for different sample radii and Fig 160 shows the corresponding plots.

Table 25. Beam interception factor calculated for 2 samples of different diameters.

Energy range	**B.I.F. for sample ⌀ = 1 cm [%]**	**B.I.F. for sample ⌀ = 2 cm [%]**
0.0215443 eV - 0.0464159 eV	25.085 ± 0.054	74.904 ± 0.067
0.0464159 eV - 0.1 eV	25.535 ± 0.048	76.010 ± 0.059
0.1 eV - 0.215443 eV	26.361 ± 0.057	77.928 ± 0.068
0.215443 eV - 0.464159 eV	26.615 ± 0.066	78.783 ± 0.077
0.464159 eV - 1 eV	26.504 ± 0.077	78.659 ± 0.090
1 eV - 2.15443 eV	26.636 ± 0.092	78.464 ± 0.108
2.15443 eV - 4.64159 eV	26.429 ± 0.110	78.242 ± 0.130
4.64159 eV - 10 eV	26.391 ± 0.133	77.930 ± 0.158
10 eV - 21.5443 eV	26.179 ± 0.161	77.898 ± 0.193
21.5443 eV - 46.4159 eV	25.977 ± 0.197	77.640 ± 0.239
46.4159 eV - 100 eV	26.074 ± 0.242	77.114 ± 0.295

100 eV - 215.443 eV	26.024 ± 0.299	77.236 ± 0.366
215.443 eV - 464.159 eV	25.495 ± 0.365	76.045 ± 0.456
464.159 eV - 1 keV	24.975 ± 0.448	75.716 ± 0.573
1 keV - 2.15443 keV	25.292 ± 0.533	75.065 ± 0.690
2.15443 keV - 4.64159 keV	26.457 ± 1.055	77.617 ± 1.358
4.64159 keV - 10 keV	24.618 ± 1.055	74.181 ± 1.395
10 keV - 21.5443 keV	26.220 ± 1.086	75.480 ± 1.410
21.5443 keV - 46.4159 keV	25.601 ± 1.052	74.608 ± 1.393
46.4159 keV - 100 keV	25.776 ± 0.963	75.155 ± 1.223
100 keV - 215.443 keV	26.794 ± 1.182	77.814 ± 1.422
215.443 keV - 464.159 keV	28.328 ± 1.081	82.288 ± 1.115
464.159 keV - 1 MeV	25.316 ± 4.975	72.152 ± 5.666

Fig.161 reports the ratio between the experimental and simulated bif, after normalization of the experimental bif at the value of the simulated bif at the energy of 4.9 eV.

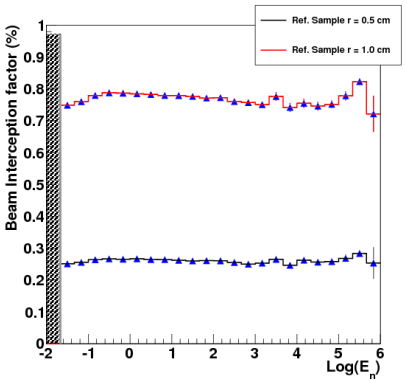

Figure 160. Beam interception factor for different sample radii.

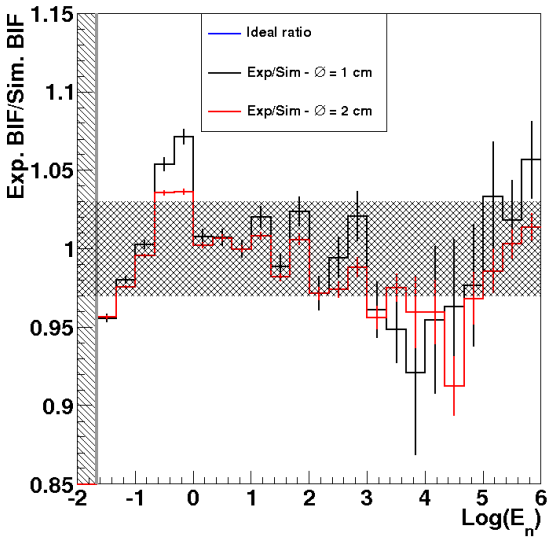

Figure 161. Ratio between the experimental and simulated (FLUKA) BIF, after the experimental results had been normalized to the simulated ones in the energy bin containing the 4.9 eV ^{197}Au resonance.

6 Second beam profiler: PXMG-MicroMegas at n_TOF

6.1 Detector description

A new micromegas detector with a pixelized anode was built in 2012 to replace the previous beam profiler and correct this way for the non flatness of the mesh. This “PXMG-micromegas" is a circular bulk of 5 cm diameter, with an anode to mesh distance equal to 128 μm. The mesh is in stainless steel, while the vacrel in the bulk is supplanted by pyralux. Each quarter of the detector is divided in 77 pixels. The interpixel distance is 150 μm and the pixel pitch measures 2.5 mm, allowing a resolution of $2.5/\sqrt{12}$ = 0.67 mm as a function of the neutron energy determined by the time of flight.

The detector is equipped with the same 2 μm $^{10}B_4C$ thick converter deposited on a kapton (12.5 μm) coppered (1 μm) foil as in the previous years (see Fig. 162). The bulk lays on a PC board in glass epoxy and is encapsulated in the cylindrical chamber employed in the past, filled again with gas (88% Ar and 10% CF_4 and 2% isobutane) at atmospheric pressure.

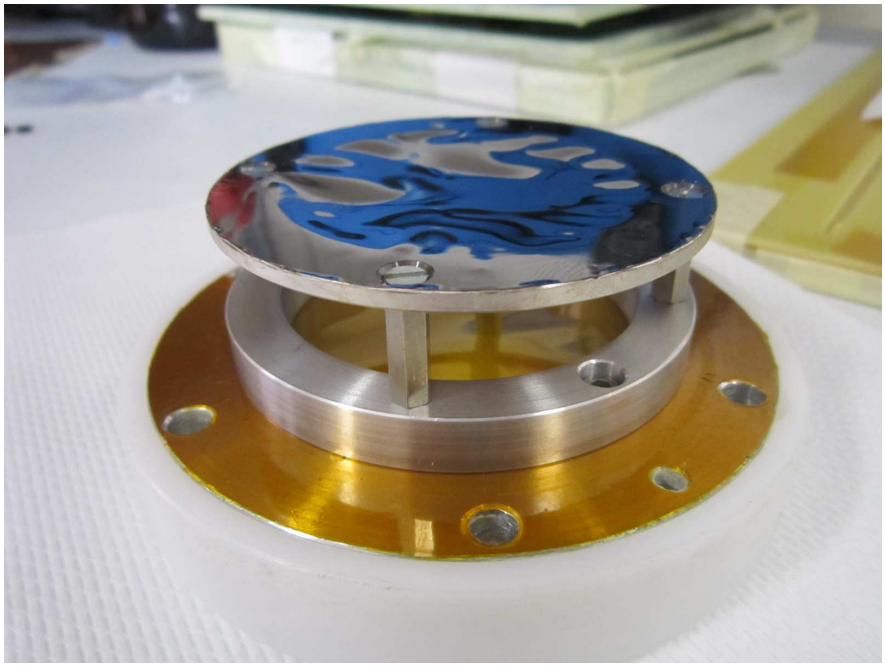

Figure 162. 2 μm $^{10}B_4C$ thick converter deposited on kapton (12.5 μm) coppered (1 μm) foil.

The left panel of Fig. 163 shows the bulk mounted on the PCB. The pixels are visible, as well as the soldering and pistes corresponding to 2 raws of connectors in every quarter of the detector. The central picture of Fig. 163 is a photo of the back part of the PCB, while the right panel shows the pistes for the readout.

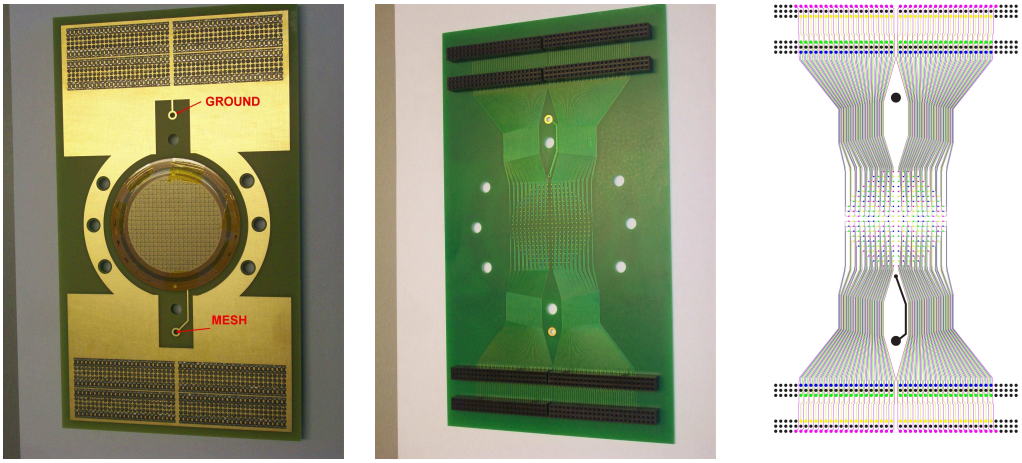

Figure 163. Left panel: detector mounted on the PCB. Central panel: back side of the PCB. Right panel: pistes for the readout of the signals induced in the pixels of the anode.

6.2 Electronics

As in the past, the readout of the signals induced in the anode is carried out by employing gassiplex cards (see Fig. 164). Each gassiplex card accomodates 6 gassiplex chips, and is predisposed for 2 connectors. The chips are the same as in the past, and what reported in §4.2 still holds. Each one of the 2 male connectors has 3 rows of 24 pins. The central row is for the ground reference, while the external ones carry the electric signals. Therefore every male connector can be used for the readout of 48 pixels, meaning that one gassiplex card can read up to 96 pistes. For semplicity, since each quarter of the detector is divided in 77 pixels, one card is used for the reading them. 19 pins (96-77) for gassiplex card are therefore not used.

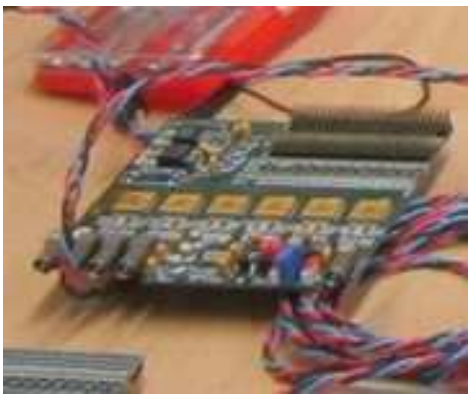

Figure 164. Gassiplex card.

When analyzing data it is necessary to know exactly which pixels is connected to which pin of which card, in order to be able to reconstruct the position of the pixel showing a signal and build the beam image. Such mapping is called decoding. Fig. 165 shows

the correspondence pixel/pin for a quarter of the detector and Fig. 166 reports the decoding.

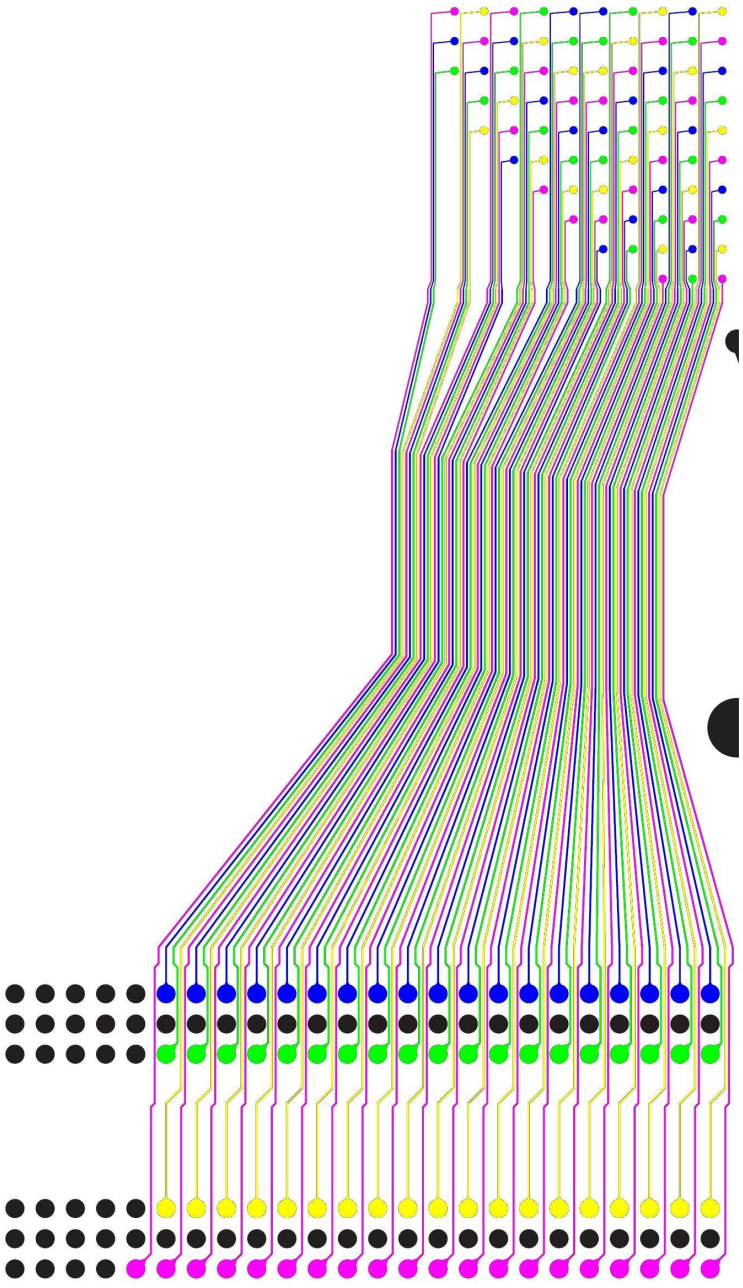

Figure 165. Pistes connecting pixels and pins in one quarter of the PXMG detector.

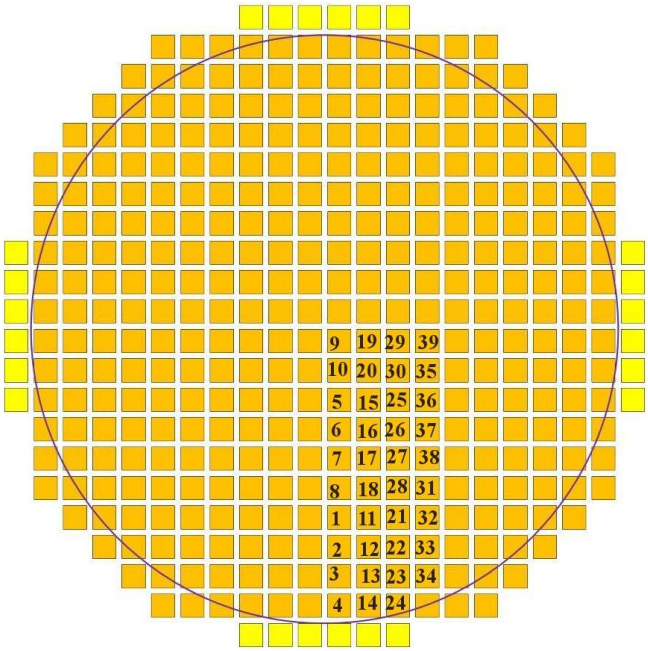

Figure 166. Decoding (it applies specularly in each quarter of the detector).

The electronic chain to process the signals is the same as the one discussed in §4.2, but adapted for 4 gassiplex cards instead than for 2.

6.3 Analysis routines

The analysis procedure follows the same steps as for the XYMG detector, thought it has been adapted for treating pixels instead of strips. Summarizing, the signals from all gassiplexes are recovered for every event in runs with no beam (pedestal) and in runs with beam. After applying the decoding to a single event of a pedestal run, it is known which pixel in the detector showed a signal of a certain amplitude. By analyzing more events of the pedestal run, a distribution of the amplitudes shown by a particular pixel is obtained and by fitting that with a gaussian function, the mean level of the electronic noise in that pixel and its standard deviation are extracted. All the remaining 76 pixels are treated the same way, to detrmine their pedestal level.

For events in beam presence, raw data are analyzed bit after bit. The mesh signal is looked for and, if found, its characteristics (time, amplitude, width and area) are stored for further processing. At the same time also the gassiplex movies are independently analyzed. The time start of every movie is kept in memory for every event and gassiplex number (which identifies the quarter of the detector to which the movie refers), together with the 77 reconstructed (i.e. rebinned) amplitudes of the signals detected in every pixel and their correspondent position in the space, which is determined thanks to the decoding. When all events have been processed, a loop on the retrieved pieces of information is performed in order to look for coincidences among the time signals in the 4 gassiplexes and in the mesh. Those movies in the mesh that do not appear to be in coincidence with 4 movies in the 4 gassiplexes are discarded. In the opposite case, the movie in the mesh and in the 4 gassiplexes are grouped together, being part of the same event. Fig. 167 shows the reconstruction of one event.

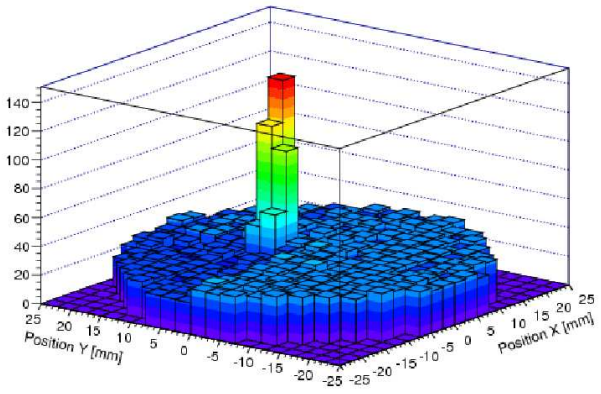

Figure 167. Example of a reconstructed event.

The following step consists in an analysis of the reconstructed events, one by one. If, in an event, the signal induced in a pixel shows an amplitude higher than 5 standard deviation of its electronic noise (after pedestal level and offset subtraction), such signal is considered to have a good probability to have been triggered by a charged particle created

in the reaction between ^{10}B and the converter and its amplitude, time and position in the detector are stored as part of a possible cluster. When all pixels have been investigated for an event, the signals registered as part of a cluster are sorted on decreasing amplitude. At this point the pixel showing the highest signal amplitude is considered as a temporary reference and the relative distance from this position to the position of the pixel showing the second highest amplitude is calculated. If the distance is smaller than a predefined value, the pixel showing the second highest amplitude becomes the reference and the distance from such pixel to the one showing the third highest amplitude is computed. Again, if the distance is smaller than the same predefined value, the reference pixel changes. In the opposite case, the pixel (let's say the number n in the list of the sorted pixel amplitudes) is simply discarded and the distance between the reference one (n-1) and the pixel number n+1 is calculated. At the end of the procedure, one cluster is found and all the discarded pixels are considered as possibly belonging to a second cluster. The cluster analysis is therefore repeated for the pixels not belonging to the first cluster and in the end a second clusters can be found. The center of charge of the 2 clusters is computed, but it was chosen to use only the first cluster to fill a 2D image of the interaction point between the converter and a neutron. Now the beam image contains only one point. All events have to undergo the same analysis to obtain a beam image with satisfactory statistics.

7 Measurements: PXMG MicroMegas

The detector was tested in the micromegas laboratory outside the n_TOF tunnel with a 88% Ar and 10% CF_4 and 2% isobutane gas mixture with a ^{109}Cd source in September 2012. The first tests the presence of current in the mesh and the detector was sent back twice to the producer for chemical cleaning.

The final test started on 19^{th} September 2012. The signal was not extracted from the anodic pixels, but from the mesh, as in all previous off-beam tests. The energy deposited by X-rays from ^{109}Cd (E_1=21.99 keV with I_1= 29.8 % and E_2=22.163 keV with I_2= 56.1 % in case of total absorption) in a gas is much lower with respect to the energy deposited by α and ^{7}Li particles in the same medium, therefore the electron mesh transparency and gain were investigated only to check the good behaviour of the detector and not to choose the voltage configurations allowing the best performance of the detector.

Finally the PXMG could be put in the neutron beam.

7.1 2012

The 2012 measurement campaign lasted around 60 hours.

7.1.1 21^{st} September 2012

Table 26. Details of the measurement performed on 21^{st} September 2012.

Configuration	TOF distance of 183.74 m
Runs	10111, 10112, 10113, 10114, 10115, 10116, 10117, 10118
Protons	4.904973e+16
Converter thickness	2 μm
Mesh Voltage	300 V - 320 [5]
Drift Voltage	450 V

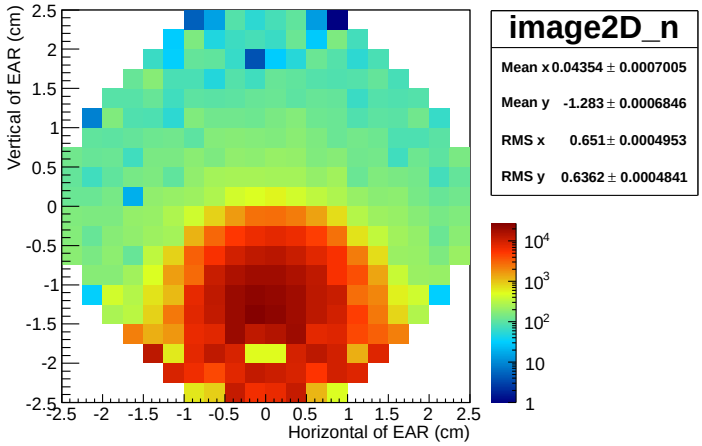

Figure 168. Beam image (μMegas detector seen in the reference system of the EAR.).

The beam image shows that all pixels are working.

[5] A voltage equal to 320 V was set in run 10111, while all other runs the voltage in the mesh was set to 300 V. Nonetheless here results are merged to accumulate more statistics

7.1.2 22^{nd} September 2012

Since Fig.168 clearly shows that the center of the detector was positioned too high, the PXMG micromegas was lowered of few 1 and a new image was acquired.

Table 27. Details of the measurement performed on 22^{nd} September 2012.

Configuration	TOF distance of 183.74 m
Runs	10135, 10136, 10137, 10138
Protons	3.2618e+16
Converter thickness	2 μm
Mesh Voltage	300 V
Drift Voltage	450 V

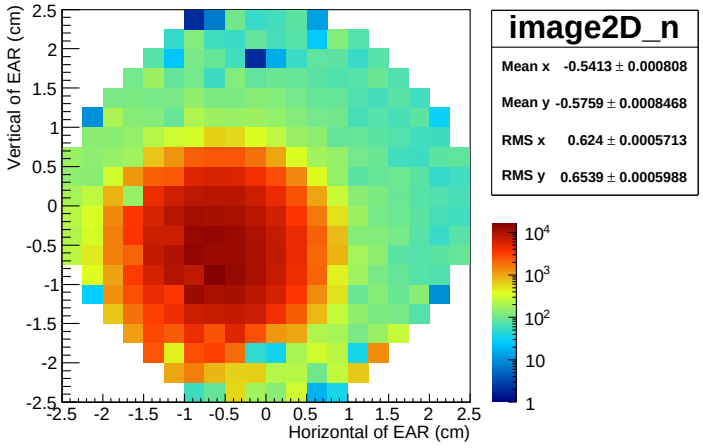

Figure 169. Beam image (μMegas detector seen in the reference system of the EAR.).

7.1.3 23rd September 2012

On the basis of the beam image acquired the night of the 22nd September 2012, the detector was moved 5 mm down and around 7 mm left.

Table 28. Details of the measurement performed on 23rd September 2012.

Configuration	TOF distance of 183.74 m
Runs	10151, 10152, 10153, 10154, 10155
Protons	3.53792e+16
Converter thickness	2 μm
Mesh Voltage	300 V
Drift Voltage	450 V

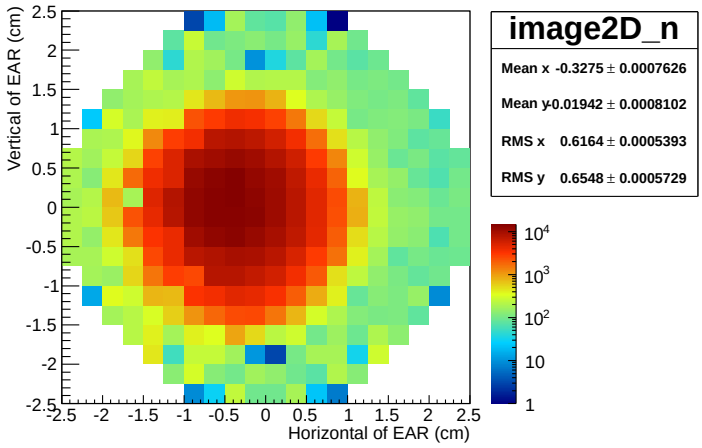

Figure 170. Beam image (μMegas detector seen in the reference system of EAR.).

The center of the detector now sees the center of the neutron beam.

7.1.4 24^{th} September 2012

A further image was acquired to have more statistics.

Table 29. Details of the measurement performed on 24^{th} September 2012.

Configuration	TOF distance of 183.74 m
Runs	10164, 10166, 10167, 10168, 10169
Protons	2.74309e+16
Converter thickness	2 μm
Mesh Voltage	300 V
Drift Voltage	450 V

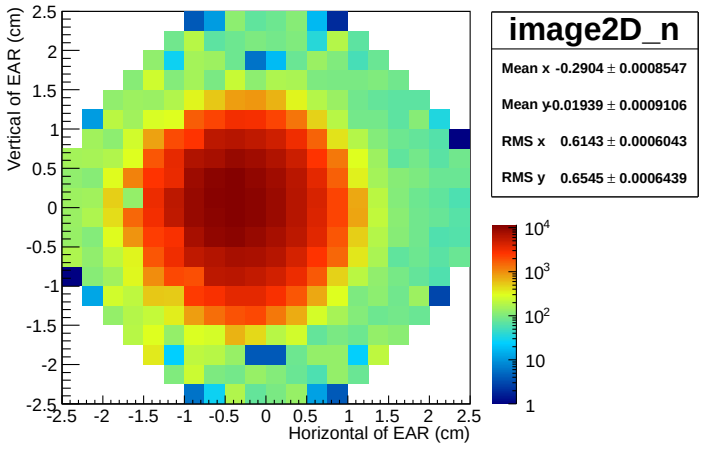

Figure 171. Beam image (μMegas detector seen in the reference system of EAR.).

Since the detector was in the same position the night of the 23^{rd} September 2012 and the night of the 24^{th} September 2012, the data can be summed, in order to have more statistics for the analysis of the beam interception factor.

7.1.5 23^{rd} + 24^{th} September 2012

Fig.172 reports the cumulative beam image.

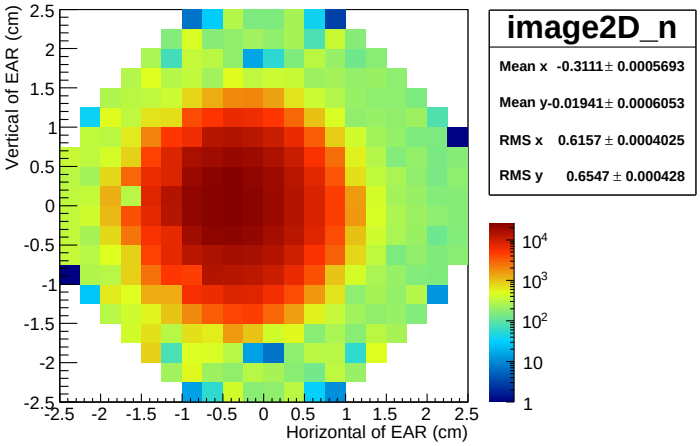

Figure 172. Beam image (μMegas detector seen in the reference system of the EAR.).

Fig.173 shows the beam profile experimentally obtained by considering all neutron energies, compared with the usual Gaussian fit and FLUKA simulations performed in CERN. The study of the beam profile for 0 neutron energy bins is not reported because of the visibly low granularity of the detector.

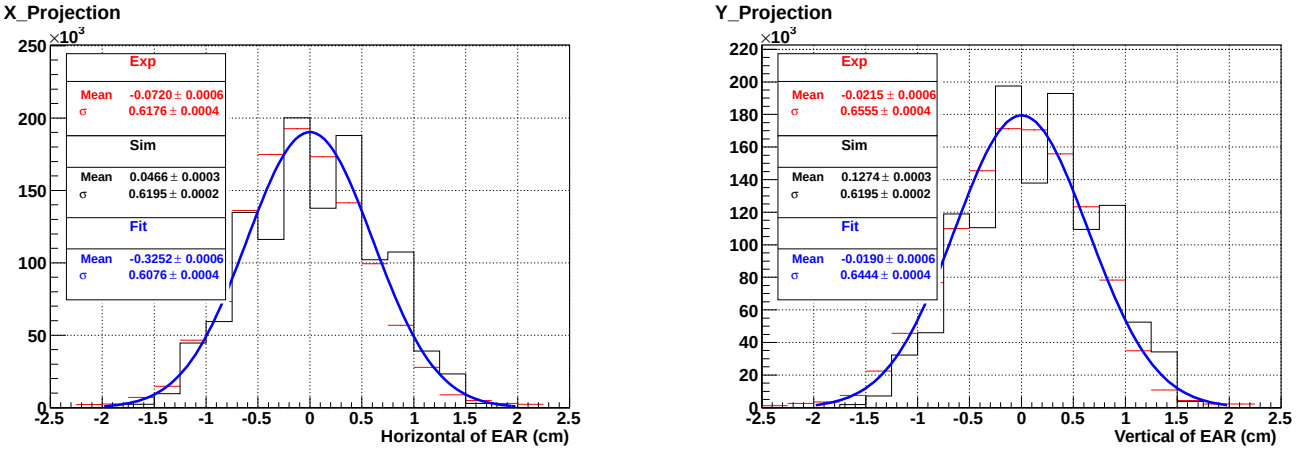

Figure 173. Beam profile for all neutron energies.

As already pointed out, the granularity of the detector is quite low. In order to extract the beam interception factor therefore the following steps were performed both for experimental data and simulations (FLUKA).

1. a 2D grid of 0.5 mm pitch square side was created and filled it up using interpolation routines
2. the peak coordinates of the beam profile in the 1-10 eV region were looked for
3. the 2D histograms was integrated within a circle of the sample diameter around the peak (diameters of 1 cm and 2 cm)
4. the 2D histograms was 0 within a circle of 4 cm around the peak
5. the BIF was derived as the ratio of the integrals calculated in 3) and 4)

In order to match the beam experimental and simulated beam interception factor in the energy region containining the 4.9 eV ^{197}Au resonance, the experimental b.i.f. was scaled by 0.92, 0.94 for 1 cm and 2 cm diameter, respectively. Table 30 reports the values of the bif in different energy bins before normalization, while Fig.174 graphically shows such results. In Fig.174 the ratio of BIF(data)/BIF(MC) was calculated, after renormalization of the experimental data at the 4.9 eV ^{197}Au resonance.

Table 30. Experimental beam interception factor calculated for 2 samples of different diameters.

Energy range	**B.I.F. for sample ⌀ = 1 cm [%]**	**B.I.F. for sample ⌀ = 2 cm [%]**
0.0215443 eV - 0.0464159 eV	23.533 ± 0.019	68.653 ± 0.021
0.0464159 eV - 0.1 eV	24.107 ± 0.017	69.881 ± 0.018
0.1 eV - 0.215443 eV	25.141 ± 0.020	72.165 ± 0.021
0.215443 eV - 0.464159 eV	25.587 ± 0.023	73.398 ± 0.024
0.464159 eV - 1 eV	25.840 ± 0.027	73.739 ± 0.027
1 eV - 2.15443 eV	25.874 ± 0.031	73.914 ± 0.032
2.15443 eV - 4.64159 eV	25.830 ± 0.037	73.717 ± 0.038
4.64159 eV - 10 eV	25.704 ± 0.044	74.000 ± 0.045
10 eV - 21.5443 eV	25.614 ± 0.052	73.601 ± 0.054
21.5443 eV - 46.4159 eV	26.128 ± 0.064	74.179 ± 0.065
46.4159 eV - 100 eV	25.737 ± 0.077	73.851 ± 0.079
100 eV - 215.443 eV	26.318 ± 0.094	74.056 ± 0.096
215.443 eV - 464.159 eV	25.732 ± 0.114	73.316 ± 0.119

464.159 eV - 1 keV	25.407 ± 0.138	72.723 ± 0.145
1 keV - 2.15443 keV	25.119 ± 0.153	72.186 ± 0.163
2.15443 keV - 4.64159 keV	25.978 ± 0.252	72.304 ± 0.268
4.64159 keV - 10 keV	26.485 ± 0.393	72.266 ± 0.417
10 keV - 21.5443 keV	24.365 ± 0.361	70.944 ± 0.396
21.5443 keV - 46.4159 keV	27.388 ± 0.367	72.385 ± 0.392
46.4159 keV - 100 keV	25.797 ± 0.321	74.383 ± 0.333
100 keV - 215.443 keV	24.795 ± 0.272	73.366 ± 0.285
215.443 keV - 464.159 keV	27.294 ± 0.226	74.500 ± 0.225
464.159 keV - 1 MeV	29.156 ± 0.181	77.226 ± 0.170

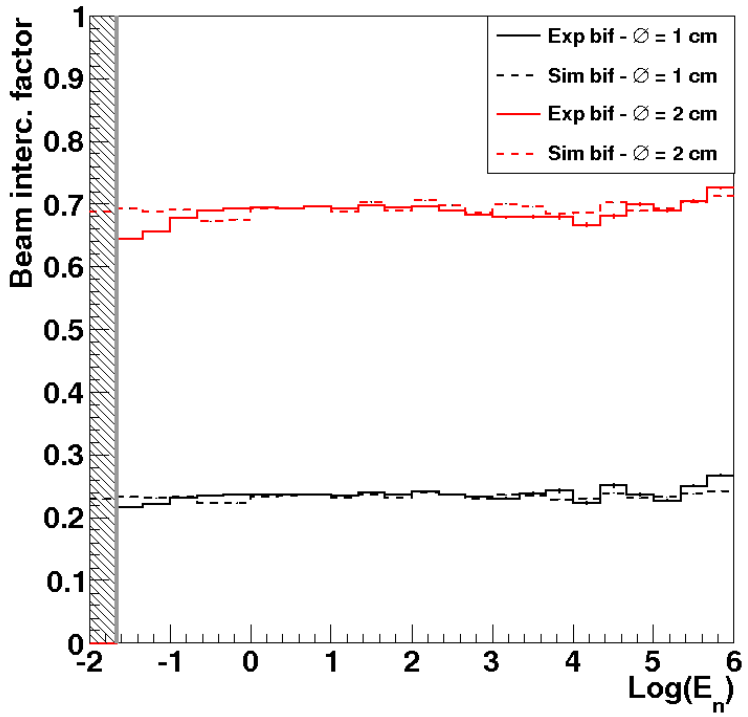

Figure 174. Comparison between the simulated (FLUKA) and experimental beam interception factors for different sample diameters. The experimental results are normalized to the simulated ones in the energy bin containing the 4.9 eV ^{197}Au resonance.

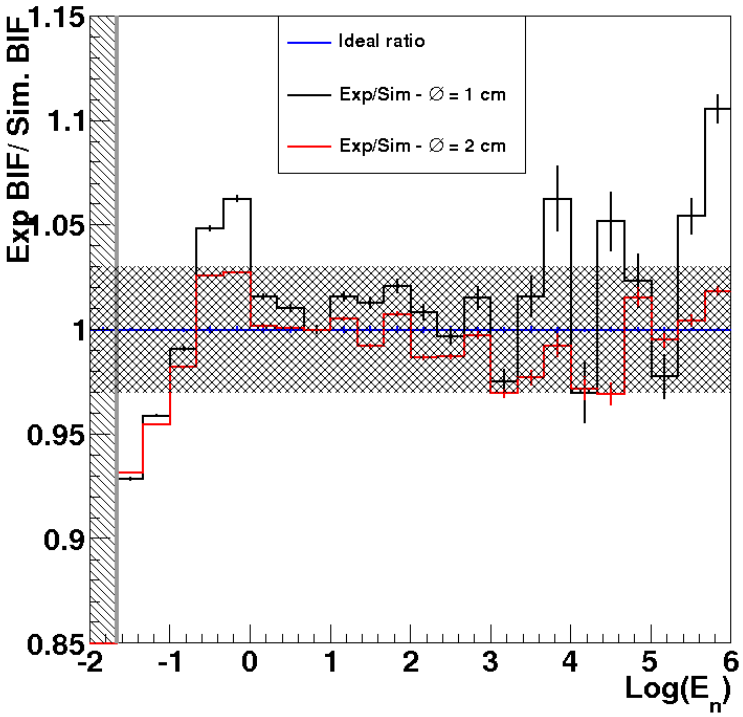

Figure 175. Ratio between the experimental and simulated (FLUKA) BIF, after the experimental results had been normalized to the simulated ones in the energy bin containing the 4.9 eV ^{197}Au resonance.

Fig. 175 shows an agreement within 3% between the simulated and experimental bif in the energy region ranging from 1 eV to 1 keV. At low neutron energies the presence of the PCB alters the bif while at high neutron energies more statistics is needed. The reported results for the bif are moreover affected by the uncertainty introduced when passing from a real 2.5 mm pitch device to a 0.5 mm grid in order to increase the granularity of the detector.

8 Observations

All along the report, the experimental data were compared to FLUKA simulations. As explained in §4.4.2 the detector itself and the PCB alter the beam profile. Therefore in order to be able to extract the beam interception factor from the experimental data, one of the two following methods could be used:

- minimization of the material composing the detector and, where not possible, replacement of low Z materials with higher Z materials.
- determination of the blurring of the beam image caused by the material composing the detector under neutron irradiation.

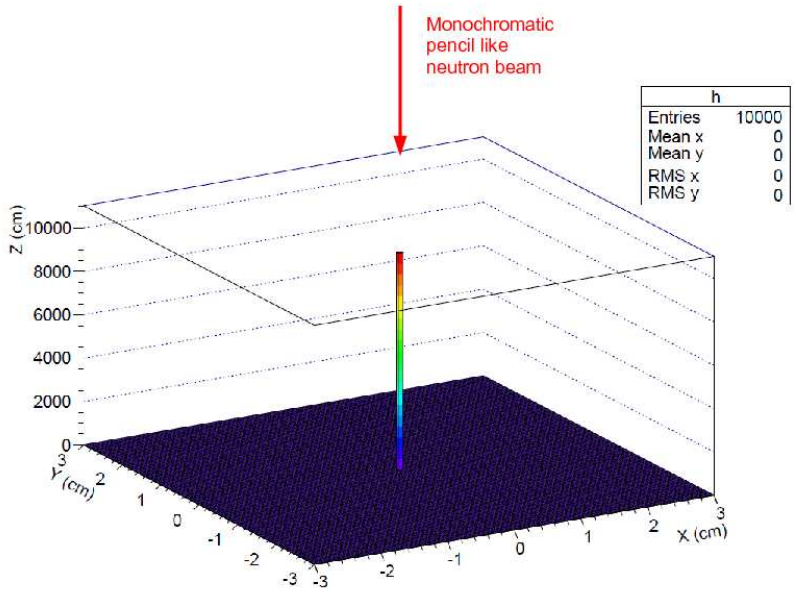

Figure 176. Expected response to a monochromatic pencil like neutron beam.

The first option, thought challenging, is the safest, since it solves the problem at its roots. The second option is feasible, thought more tricky. The idea lying behind is that once the blurring level is known, it can be corrected for. More in details, if a monochromatic pencil like neutron beam travelling along the z direction towards a surface lying in the xy plane, strikes it in the position (x,y)=(0,0), in a 2D histogram representing the beam image a single column at such position is present, as in Fig.176, and its height is proportional to the number of shot neutrons.

In other words, the answer to a monochromatic pencil like neutron beam, in absence of the ^{10}B converter, micromegas detector, and PCB, is a Dirac delta function δ. If the neutron monochromatic pencil like neutron beam instead strikes a converter in the position (x,y)=(0,0), charged particles are created and emitted in directions allowed by the kinematics of the reaction. Things get more complicate because of the presence of the gas, of the PCB, and because of the center of charge analysis. In the end, the response to the initial monoenergetic pencil like neutron beam results to be approximable with a bidimensional Gaussian function centered in (0,0) and with widths σ_x and σ_y determined by the previously listed factors. In symbols, we passed from $\delta(0,0)$ to a $G(0,\sigma_x,0,\sigma_y)$. For simplicity let's reduce to the generic monodimensional case:

$$\delta(x) \rightarrow G(x,\sigma_x) \tag{4}$$

It is known that

$$G(x,\sigma_x) = x \cdot G(1,\frac{\sigma_x}{x}).$$

Therefore, if σ_x is known for a certain neutron energy, in principle it is possible to apply a deconvolution to every point x and reverse the arrow of 4:

$$G(x, \sigma_x) \rightarrow \delta(x) \tag{5}$$

Of course this operation should be performed for every neutron energy and incident angle, thought in a first approach we can discard the last factor assuming that the opening angle of the neutron beam is small.

Since usually the results presented in this report were given in 3 bins per decade and spanned on 8 decades (from 0.01 eV to 1 MeV), as a starting point 24 GEANT4 simulations were performed. In all simulations the geometry is the same (implementation of the detector and PCB) and the incident particles are $50 \cdot 10^6$ monochromatic neutrons in a pencil-like beam. The energy of the incident neutrons differ from simulation to simulation and is simply chosen so that it belongs to one of resulting 24 energy bins. The results of the simulations were treated exactly as the experimental results for the XYMG detector and 24 beam images were obtained. The choice of analyzing the events generated from GEANT4 as the data of a detector with strips in orthogonal directions and not pixels, is only due to the fact that at the time the simulations were started, a validation for the strip configuration had been already performed (see §4.4).

Fig.177 - Fig.178 show the blurring in the beam image introduced by the presence of the detector and its PCB when a monochromatic pencil-like neutron propagating perpendicularly to the converter, strikes it in the center. Unfortunately, the accumulated statistics is really low. More computing time is needed for acceptable results.

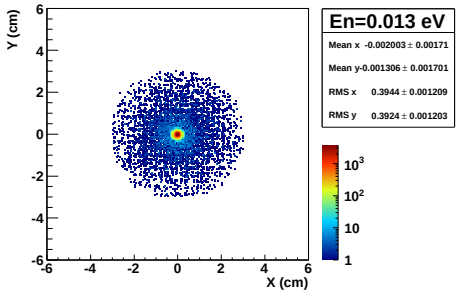

Figure 177. Simulated (GEANT4) response to a 0.013 eV pencil like neutron beam

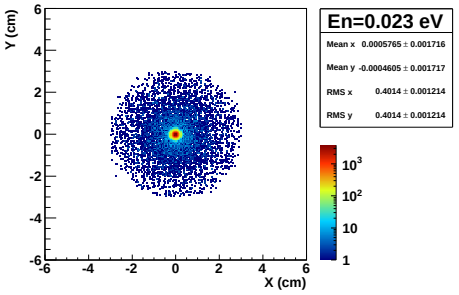

Figure 178. Simulated (GEANT4) response to a 0.023 eV pencil like neutron beam

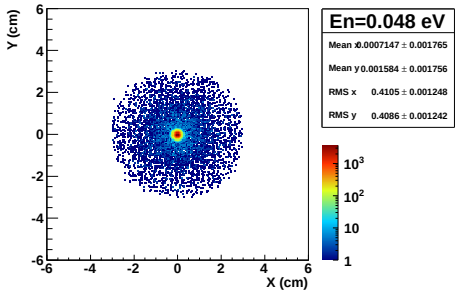

Figure 179. Simulated (GEANT4) response to a 0.048 eV pencil like neutron beam

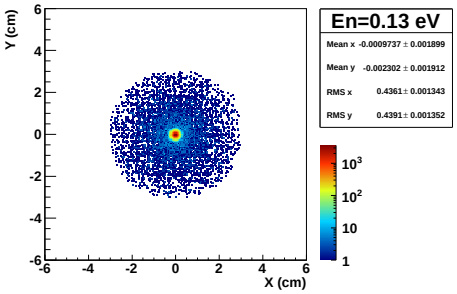

Figure 180. Simulated (GEANT4) response to a 0.13 eV pencil like neutron beam

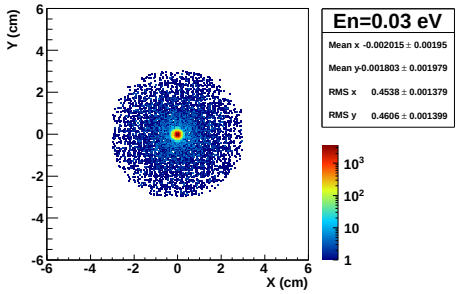

Figure 181. Simulated (GEANT4) response to a 0.23 eV pencil like neutron beam

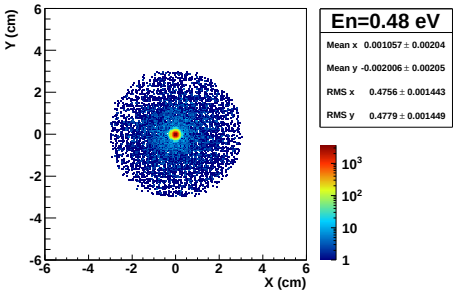

Figure 182. Simulated (GEANT4) response to a 0.48 eV pencil like neutron beam

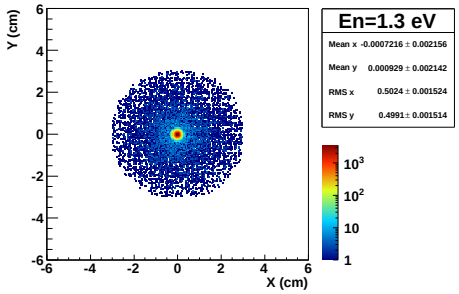

Figure 183. Simulated (GEANT4) response to a 1.3 eV pencil like neutron beam

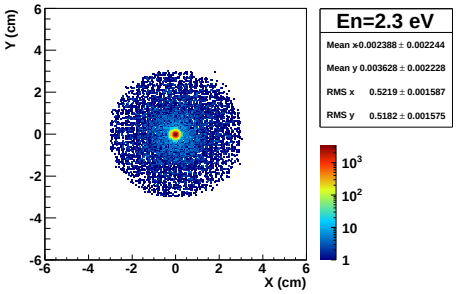

Figure 184. Simulated (GEANT4) response to a 2.3 eV pencil like neutron beam

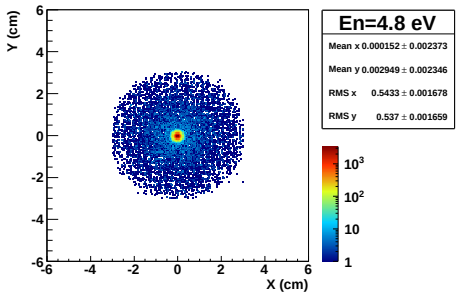

Figure 185. Simulated (GEANT4) response to a 4.8 eV pencil like neutron beam

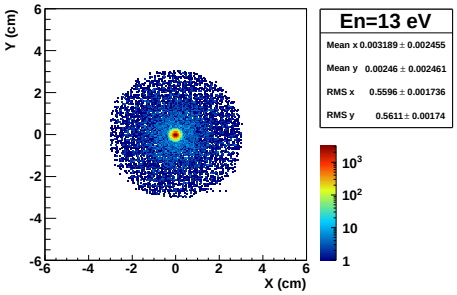

Figure 186. Simulated (GEANT4) response to a 13 eV pencil like neutron beam

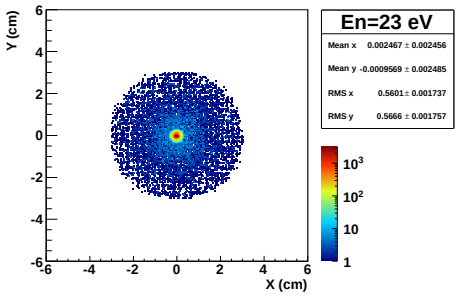

Figure 187. Simulated (GEANT4) response to a 23 eV pencil like neutron beam

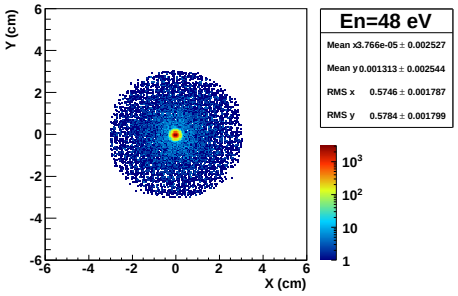

Figure 188. Simulated (GEANT4) response to a 48 eV pencil like neutron beam

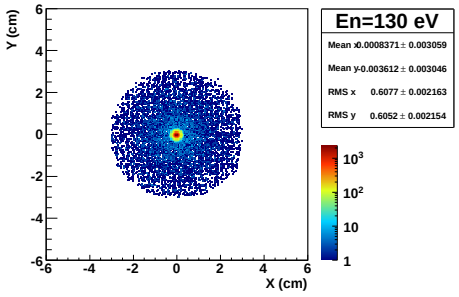

Figure 189. Simulated (GEANT4) response to a 130 eV pencil like neutron beam

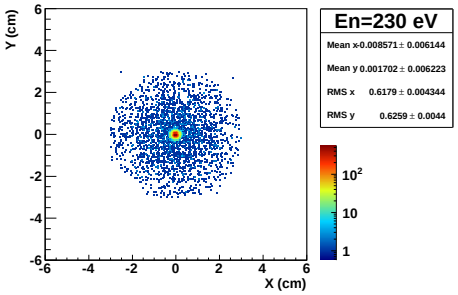

Figure 190. Simulated (GEANT4) response to a 230 eV pencil like neutron beam

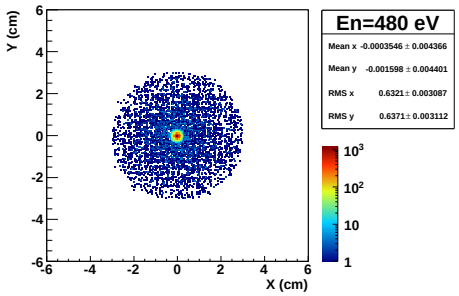

Figure 191. Simulated (GEANT4) response to a 480 eV pencil like neutron beam

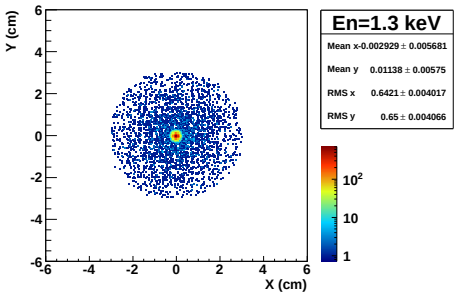

Figure 192. Simulated (GEANT4) response to a 1.3 keV pencil like neutron beam

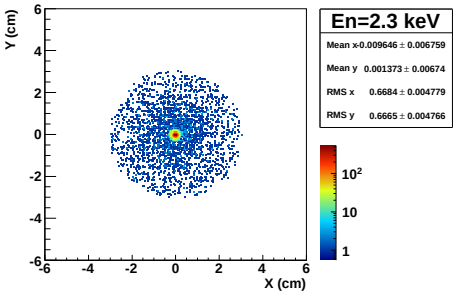

Figure 193. Simulated (GEANT4) response to a 2.3 keV pencil like neutron beam

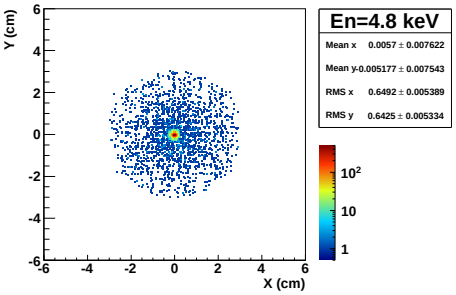

Figure 194. Simulated (GEANT4) response to a 4.8 keV pencil like neutron beam

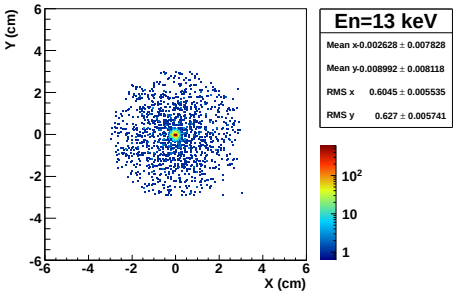

Figure 195. Simulated (GEANT4) response to a 13 keV pencil like neutron beam

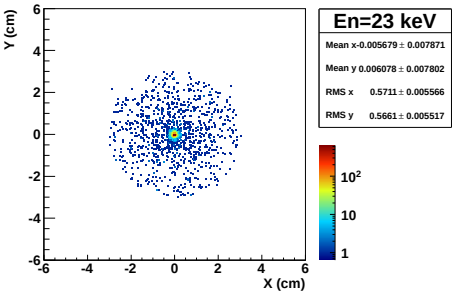

Figure 196. Simulated (GEANT4) response to a 23 keV pencil like neutron beam

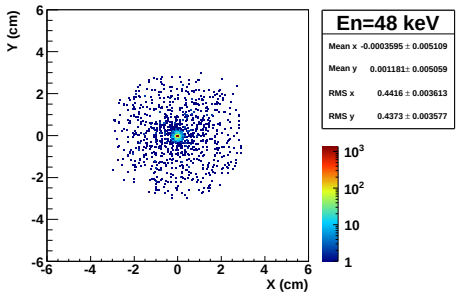

Figure 197. Simulated (GEANT4) response to a 48 keV pencil like neutron beam

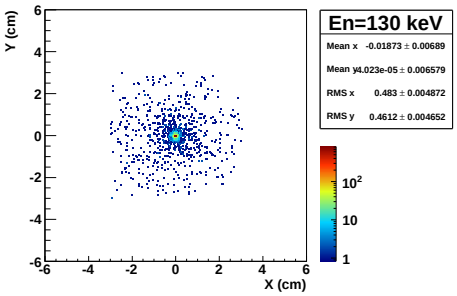

Figure 198. Simulated (GEANT4) response to a 130 keV pencil like neutron beam

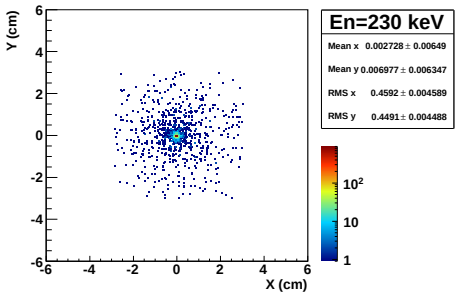

Figure 199. Simulated (GEANT4) response to a 230 keV pencil like neutron beam

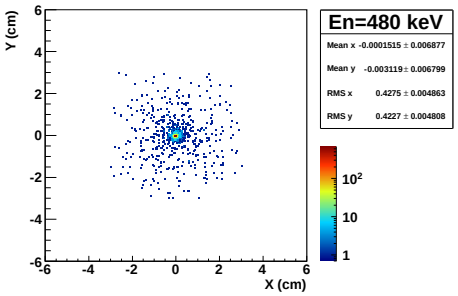

Figure 200. Simulated (GEANT4) response to a 480 keV pencil like neutron beam

9 Conclusions

The “XY-micromegas” detector has been successfully used at the n_TOF facility to validate the beam position with respect to sample targets, to study the beam profile and to extract the beam interception factor. Simulations performed by the n_TOF FLUKA group were compared to experimental results, showing a good comprehension of the collimation system of the facility. The detector anyhow suffered from a fabrication defect. It was in fact conceived to be one of the first prototypes of μBulk with readout in 2D, but failed. The readout was saved and glued on a PCB, and a bulk was built on such readout. As a consequence of heating up materials with different dilation coefficients, a not flat mesh was obtained.

A new bulk detector, with a pixelized anode, was built and used as beam profiler. The new “PXMG” perfectly worked, but the discrepancy between the experimental beam interception factor and the one obtained by FLUKA simulations performed at CERN in some energy regions, reaches and even depasses, 6% and more. After deeper analysis (the report is organized in a logic order, not chronological. In reality all GEANT4 simulations were in fact performed after the analysis of the XYMG data and before and during the one of the PXMG data) it was observed that the presence of the PCB was strongly contributing to a distorsion of the expected beam interception factor.

A new beam profiler has been designed, paying high attention to the material budget. Important efforts have been done in order to minimize the presence of hydrogen in the overall structure.

10 Acknowledgments

This work is the result of the interaction of several people I owe many thanks to.

I am sincerly grateful to Frank Gunsing for his help, which extends far beyond this report, for his everyday support along 3 years with constructive discussions, explanations, advice, patience, trusting, humor and kindness. His help ranged from fundamental physics to experimental physics, passing through programming languages, mathematics and software tools, but never forgetting humanity.

I thank from heart Thomas Papaevangelou, for his availability in sharing his deep experties in detector physics and the related data analysis procedure, for his help in learning GEANT4, his patience, presence, good mood and character. His passion for his job is contagious, as his smile to people.

Many thanks to Eric Berthoumieux and Carlos Guerrero for productive discussions, for setting up micromegas campaign measurements in n_TOF, as well as for coordinating information from different institutes.

I wish to thank all the people who implemented the FLUKA simulations of the beam profile in CERN and in particular Andrea Tsinganis, Vasilis Vlachoudis and Marco Calviani for their feedback and information.

I would like to express my deep appreciation to Ioanis Giomataris, the father of micromegas detectors, for his experties and kindness.

I am indebted to Mariam Kebbiri and Francisco Iguaz for all the time they spent in helping me to get acquainted with micromegas detectors, but also for their kindness both at job and outside and for good working atmosphere.

References

[1] For more documentation see `http://www.cern.ch/ntof`.

[2] For more documentation see `http://irmm.jrc.ec.europa.eu/about_IRMM/laboratories/Pages/the_van_de_graaff_laboratory.aspx`.

[3] F.-J. Hambsch, editor. *"EFNUDAT Fast Neutrons. Proceedings of the Scientific Workshop on Neutron Measurements, Theory and Applications Nuclear Data for Sustainable Nuclear Energy"*, Retieseweg 111, B - 2440 Geel,Belgium, April 2009. Joint Research Center (Institute for Reference Materials and Measurements), European Union.

[4] Andreas Eriksson. "The intensity profile of a neutron beam of 96 MeV at TSL". Master's thesis, Uppsala University, January 2007.

[5] Y. Giomataris, Ph. Rebourgeard, J.P. Robert, and G. Charpak. Micromegas: a high-granularity position-sensitive gaseous detector for high particle-flux environments. *Nucl. Instr. Meth.*, A(376):29–35, 1996.

[6] Y. Giomataris, R. De Oliveira, S. Andriamonje, S. Aune, G. Charpak, P. Colas, A. Giganon, Ph. Rebourgeard, and P. Salin. Micromegas in a bulk. *Nucl. Instr. Meth.*, A(560):405–408, 2005.

[7] S. Andriamonje, D. Attie, E. Berthoumieux, M. Calviani, P. Colas, T. Dafni, G. Fanourakis, E. Ferrer-Ribas, J. Galan, T. Geralis, A. Giganon, I. Giomataris, A. Gris, C. Guerrero Sanchez, F. Gunsing, F.J. Iguaz, I. Irastorza, R. De Oliveira, T. Papaevangelou, J. Ruz, I. Savvidis, A. Teixeraa, and A. Tomasc. Development and performance of microbulk micromegas detectors. *J. Instrum.*, 5:P02001–P02013, 2010.

[8] S. Andriamonje, S. Aune, E. Berthoumieux, R. De Oliveira, A. Giganon, I. Giomataris, F. Gunsing, J. F. Lecolley, J. Pancin, M. Riallot, R. Rosa, , and I. Savvidis. Recent developments of a micromegas detector for neutron physics. *IEEE Transactions On Nuclear Science*, 56(3), 2009.

[9] M. Calviani, S. Andriamonje, and E. Berthoumieux. New 2D micromegas detector for n_TOF beam profile: description and preliminary results. *CERN, n_TOF Internal Note*, 2009.

[10] A 16 integrated channels front end analog amplifiers with multiplex serial readout. Ref:PC 2000/107 (2000), `http://www-subatech.in2p3.fr`.

[11] J. A. Galán-Lacarra. *Probing eV-mass scale Axions with a Micromegas Detector in the CAST Experiment*. PhD thesis, University of Zaragoza, 2011.

[12] M. Bräger. *Redesign and Functional Extension of the Robotic Tape Queueing System within the CASTOR HSM*. PhD thesis, Fachhochschule Wiesbaden, University of Applied Sciences Fachbereich Informatik, 2005.

[13] D. Cano Ott. Library version "rf_libr_v20.c", CIEMAT, 27/3/2001.

[14] Miroslav Morháč. An algorithm for determination of peak regions and baseline elimination in spectroscopic data. *Nucl. Instr. Meth.*, A(600):478–487, 2009.

[15] C. Guerrero and *et al*. Performance of the neutron time-of-flight facility n_tof at cern. *Eur. Phys. J.*, A(49):27, 2013.

[16] S Andriamonje, Y Giomataris, V Vlachoudis, C Guerrero, P Schillebeeckx, R Losito, R Sarmento, M Calviani, A Giganon, F Gunsing, E Berthoumieux, P Siegler, and Y Kadi. A transparent detector for n_tof neutron beam monitoring. *J. Korean Phys. Soc.*, 59(2, Part 3, SI):1597–1600, 2011.

[17] S. Marrone, P.F. Mastinu, U. Abbondanno, R. Baccomi, E.Boscolo Marchi, N. Bustreo, N. Colonna, F. Gramegna, M. Loriggiola, S. Marigo, P.M. Milazzo, C. Moreau, M. Sacchetti, G. Tagliente, R. Terlizzi, G. Vannini, G. Aerts, E. Berthomieux, D. Cano-Ott, and et al. P. Cennini. Micromegas in a bulk. *Nucl. Instr. Meth.*, A(517):389–398, 2004.

[18] S.F. Biagi. Monte carlo simulation of electron drift and diffusion in counting gases under the influence of electric and magnetic fields. *Nucl. Instr. and Meth.*, A(421):234–240, 1999.

[19] G. Battistoni, S. Muraro, P.R. Sala, F. Cerutti, A. Ferrari, S. Roesler, and A. Fasso‘and J. Ranft. The FLUKA code: Description and benchmarking. Proceedings of the Hadronic Shower Simulation Workshop 2006, Fermilab 6–8 September 2006, M. Albrow, R. Raja eds., AIP Conference Proceeding 896, 31-49, (2007).